

# Multiscale Modeling of Amphibian Neurulation

By

Xiaoguang Chen

A Thesis  
presented to the University of Waterloo  
in fulfillment of the  
thesis requirement for the degree of  
Doctor of Philosophy  
in  
Civil Engineering

Waterloo, Ontario, Canada, 2007

© Xiaoguang Chen 2007

I hereby declare that I am the sole author of this thesis. This is a true copy of the thesis, including any required final revisions, as accepted by my examiners.

I understand that my thesis may be made electronically available to the public.

# Abstract

This thesis presents a whole-embryo finite element model of neurulation -- the first of its kind. An advanced, multiscale finite element approach is used to capture the mechanical interactions that occur across cellular, tissue and whole-embryo scales. Cell-based simulations are used to construct a system of constitutive equations for embryonic tissue fabric evolution under different scenarios including bulk deformation, cell annealing, mitosis, and Lamellipodia effect. Experimental data are used to determine the parameters in these equations.

Techniques for obtaining images of live embryos, serial sections of fixed embryo fabric parameters, and material properties of embryonic tissues are used. Also a spatial-temporal correlation system is introduced to organize and correlate the data and to construct the finite element model. Biological experiments have been conducted to verify the validity of this constitutive model.

A full functional finite element analysis package has been written and is used to conduct computational simulations. A simplified contact algorithm is introduced to address the element permeability issue.

Computational simulations of different cases have been conducted to investigate possible causes of neural tube defects. Defect cases including neural plate defect, non-neural epidermis defect, apical constriction defect, and convergent extension defect are compared with the case of normal embryonic development. Corresponding biological experiments are included to support these defect cases. A case with biomechanical feedbacks on non-neural epidermis is also discussed in detail with biological experiments and computational simulations. Its comparison with the normal case indicates that the introduction of biomechanical feedbacks can yield more realistic simulation results.

# Acknowledgements

I would like to express my deep gratitude to my supervisor, Dr. G. Wayne Brodland, for his time and effort in helping me understand the essence behind the complex phenomena. Without his help the thesis could not have completed.

To my family for their support of my academic career. Their moral support, love, understanding, and patience over these years of my post secondary education have been great.

I owe my wife Rong Sun an eternal debt of gratitude for what she has done during the four years of separation. Without her sacrifice, my doctoral study could not have completed.

To my colleagues Jim Veldhuis, Greg Bootsma and Denis Viens for their help with software and visualization issues, without them, this project would not have succeeded. And to Caleb Horst, Paul Groh, Abby Li, Fatima Kakal, Simon Tsui and Justina Yang for those wonderful sports time every week and help on thesis proofreading.

The leisure time at Waterloo would be too boring if I had not known these fellows:  
Wensheng Bu, Ashley Li, Qinghua Huang, Dan Mao, Qiang Wang, Henry Zhang, Yan Zhou, Jinyu Zhu, and Tianjin Cheng.

This research was funded by a Natural Sciences and Engineering Research Council (NSERC) and a Canadian Institutes for Health Research (CIHR) Research Grant to G.W. Brodland.

# Table of Contents

|   |      |
|---|------|
| Abstract.....   | iii  |
| Acknowledgements.....                                   | iv   |
| Table of Contents.....                                  | v    |
| List of Tables .....                                    | viii |
| List of Tables .....                                    | viii |
| List of Figures.....                                    | ix   |
| Nomenclature.....                                       | xii  |
| Chapter 1 Introduction .....                            | 1    |
| 1.1 Malformation: Birth Defect.....                     | 1    |
| 1.2 Fundamental understanding of neurulation .....      | 3    |
| 1.3 Purpose and Motivation .....                        | 3    |
| 1.4 What do we expect to learn? .....                   | 7    |
| Chapter 2 Literature Review .....                       | 10   |
| 2.1 Biological background.....                          | 10   |
| 2.1.1 Sub-cellular components.....                      | 11   |
| 2.1.2 Cell-cell interactions .....                      | 15   |
| 2.1.3 Basic morphogenetic movements .....               | 18   |
| 2.2 Morphogenesis research progress .....               | 20   |
| 2.2.1 Biological perspective.....                       | 20   |
| 2.2.2 Chemical or applied mathematics perspective ..... | 21   |

|   |    |
|---|----|
| 2.2.3 Mechanical perspective .....  | 22 |
| 2.3 Cellular scale model and tissue scale model.....  | 23 |
| 2.3.1 Cellular scale models.....  | 25 |
| 2.3.2 Tissue scale Models.....  | 35 |
| 2.3.3 Challenge for cellular scale models: .....  | 39 |
| 2.3.4 Challenge for tissue scale models: .....  | 40 |
| 2.4 Multiscale Modeling.....  | 41 |
| 2.5 The what, why and how of our model .....  | 42 |
| <br>  |    |
| Chapter 3 Constitutive Model .....  | 44 |
| 3.1 Finite Element Simulation of Cellular Scale Models.....                                       | 45 |
| 3.2 Governing Parameters .....  | 50 |
| 3.3 Bulk Deformation .....  | 52 |
| 3.4 Cell Annealing.....   | 55 |
| 3.5 Mitosis .....   | 55 |
| 3.6 Lamellipodia effect .....   | 56 |
| 3.7 Collective Effect on Tissue Fabric Evolution .....  | 62 |
| 3.8 Model validation.....   | 64 |
| <br>  |    |
| Chapter 4 Geometric Data.....   | 68 |
| 4.1 Determining embryo shape.....   | 68 |
| 4.2 Defining tissue fabric parameters.....  | 70 |
| 4.3 Determining the thickness of embryonic epithelium .....                                       | 72 |
| 4.4 Measuring material properties.....  | 73 |
| <br>  |    |
| Chapter 5 Feature Grid .....  | 76 |
| 5.1 Parametric Coordinate Systems.....  | 77 |
| 5.2 Transformation from parametric to Cartesian coordinates $(u, v) \rightarrow (x, y, z)$ .....  | 79 |
| 5.3 Transformation from Cartesian to parametric coordinates: $(x, y, z) \rightarrow (u, v)$ ..... | 81 |
| 5.4 Database Inquiry System .....   | 84 |

|   |     |
|---|-----|
| Chapter 6 Finite Element Model.....                                     | 87  |
| 6.1 Package structure.....  | 87  |
| 6.1.1 Preprocessing and postprocessing:.....                            | 87  |
| 6.1.2 Computational engine.....   | 90  |
| 6.2 Contact Algorithm.....  | 95  |
| Chapter 7 Computational Simulations.....                                | 99  |
| 7.1 Reference case for normal Axolotl embryo development.....           | 99  |
| 7.2 Impact of tissue mechanical property defects on neurulation.....    | 107 |
| 7.2 Impact of biochemical mechanism defects on Axolotl neurulation..... | 110 |
| 7.3 Biomechanical feedbacks.....  | 115 |
| Chapter 8 Discussions and Future work.....                              | 122 |
| Appendix A Assembly of the Matrix Equations.....                        | 125 |
| References.....   | 130 |

# List of Tables

|   |     |
|---|-----|
| Table 2.1 Comparison of different models .....              | 32  |
| Table 5.1. Database table.....                              | 86  |
| Table 7.1. Comparison of different defective scenarios..... | 114 |
| Table 7.2. Stage 13, 15, 17 stress resultant summary. ....  | 120 |

# List of Figures

|   |    |
|---|----|
| Figure 1.1. Schematic representation of spina bifida.....   | 1  |
| Figure 1.2. Schematic representation of embryonic neurulation.....  | 2  |
| Figure 2.1. Neurulation mechanisms in different levels.....   | 11 |
| Figure 2.3. Intermediate filaments strengthen animal cells.....   | 13 |
| Figure 2.4. Microtubules are polarized and possess dynamic instability.....   | 13 |
| Figure 2.5. Some roles of myosin-I and myosin-II in a eucaryotic cell. ....   | 14 |
| Figure 2.6. Schematic overview of major adhesive interactions that bind cells to each other<br>and to the extracellular matrix..... | 16 |
| Figure 2.7. The eight basic morphogenetic movements in tissue scale.....  | 19 |
| Figure 2.8. Invagination, evagination and folding of epithelium.....  | 24 |
| Figure 2.9. Cell sorting.....   | 25 |
| Figure 2.10. Cell Exchange in a Cell Lattice Model.....   | 26 |
| Figure 2.11. Simulation of cell sorting by cell exchanges.....  | 27 |
| Figure 2.12. Cell-centric model [Brodland, 2004].....   | 28 |
| Figure 2.13. Simulation of cell sorting using a cell-centric model.....   | 28 |
| Figure 2.14. Sub-cellular lattice model.....  | 29 |
| Figure 2.15. Vertex model.....  | 30 |
| Figure 2.16. Schematic cell cross-section and its corresponding finite element model. ....  | 31 |
| Figure 2.17. Simulation of cell sorting using finite element model. ....  | 31 |
| Figure 2.18. Ingber's ECM influence model.....  | 34 |
| Figure 2.19. Partially dissociated 111-cell finite element mesh.....  | 35 |
| Figure 2.20. Tissue scale models driving force hypotheses.....  | 36 |
| Figure 2.21. Apical constriction model of amphibian neurulation.....  | 37 |
| Figure 2.22. Clausi and Brodland finite element model.....  | 38 |
| Figure 2.23. Cortical flow of adhesive structures.....  | 38 |

|  |    |
|--|----|
| Figure 2.24. A schematic representation of growth and morphogenesis of the entire organism and its parts in terms of the hydromechanical model. .... | 39 |
| Figure 3.1. A schematic representation of a piece of epithelium. ....  | 46 |
| Figure 3.2. The cell and finite element models. ....   | 47 |
| Figure 3.3. Coding assumptions about cell rearrangement. ....  | 49 |
| Figure 3.4. Composite cell. ....   | 51 |
| Figure 3.5. Deformation of the cell patch. ....  | 53 |
| Figure 3.6. Mapping of an arbitrary vector $v(\eta)$ into $Hv(\eta)$ ....  | 54 |
| Figure 3.7. Temporal evolution of cellular fabric with Lamellipodia effect. ....   | 56 |
| Figure 3.8. Cell aspect ratio versus dimensionless time. ....  | 57 |
| Figure 3.9. Normalized stress versus time. ....  | 58 |
| Figure 3.10. Simulations of a patch of cells with $q=2$ , $R=0.2$ and $r=0.13$ . ....  | 59 |
| Figure 3.11. $\kappa$ versus dimensionless time $\tau$ with different relative strength $q$ . ....   | 61 |
| Figure 3.12. $\frac{d\kappa_L}{d\tau}$ versus relative strength $q$ with different boundary conditions. ....   | 62 |
| Figure 3.13. Planar view of a monolayer cell aggregate. ....   | 63 |
| Figure 3.14. Finite element analysis procedure diagram. ....   | 66 |
| Figure 3.15. Model validation. ....  | 67 |
| Figure 4.1. The robotic microscope and a reconstruction made using it. ....  | 69 |
| Figure 4.2. Representative images of embryonic epithelia. ....   | 70 |
| Figure 4.3. An image of a cellular tissue and its corresponding magnitude response image. ....   | 71 |
| Figure 4.4. A transverse serial section. ....  | 72 |
| Figure 4.5. Schematic diagram of the tissue tester. ....   | 74 |
| Figure 4.6. Embryo coordinate system and specimen locations [Wiebe, 2005]. ....  | 75 |
| Figure 5.1. Embryonic region identification. ....  | 77 |
| Figure 5.2. Parametric coordinate systems. ....  | 78 |
| Figure 5.3. Mapping from parametric coordinate onto the 3D embryo model. ....  | 78 |
| Figure 5.4. Linear interpolation. ....   | 79 |
| Figure 5.5. Quadratic interpolation. ....  | 80 |

|   |     |
|---|-----|
| Figure 5.6. Gradually approaching algorithm.....  | 82  |
| Figure 5.7. Transformation between different coordinate systems.....  | 82  |
| Figure 5.8. Parametric coordinate systems of different regions on embryo’s surface. ....  | 83  |
| Figure 5.9. Schematic chart for inquiry system. ....  | 85  |
| Figure 6.1. Software package. ....  | 88  |
| Figure 6.2. Graphic user interfaces of ChiChi3D. ....   | 89  |
| Figure 6.3. Graphic user interfaces of Zazu. ....   | 89  |
| Figure 6.4. Pentahedral element. ....   | 92  |
| Figure 6.5. Various boundary conditions.....  | 93  |
| Figure 6.6. Contact problems. ....  | 95  |
| Figure 6.7. Schematic of contact algorithm. ....  | 97  |
| Figure 6.8. Comparison of simulation with and without contact algorithm.. ....  | 98  |
| Figure 7.1. Comparison of simulations of a transverse strip of tissue.. ....  | 100 |
| Figure 7.2. Apical constriction and convergent extension facilitate the medial movement of neural folds.....                                  | 103 |
| Figure 7.3. The CE-like behaviour in the non-neural epidermis.....  | 104 |
| Figure 7.4. Normal development of Axolotl embryo (Table 7.1 case 1).....  | 106 |
| Figure 7.5. The mechanical property defect in neural plate region (Table 7.1 case 2). ....  | 108 |
| Figure 7.6. The mechanical property defects in non-neural epidermis region .....  | 109 |
| Figure 7.7. Disabling Shroom expression leads to severe neural tube defect.....   | 111 |
| Figure 7.8. Biomechanical contribution of convergent extension to neural tube closure.....  | 112 |
| Figure 7.9. Disabling convergent extension leads to severe neural tube defect. ....   | 113 |
| Figure 7.10. Schemes of hyper-restoration responses to the shifts of mechanical stresses from the initial values denoted by black spots. .... | 115 |
| Figure 7.11. A scheme of contraction-extension (CE) feedback. ....  | 116 |
| Figure 7.12. With and without CE feedback on non-neural epidermis. ....   | 121 |
| Figure A.1. The cell and finite element models.....   | 121 |
| Figure A.2. System of Orthogonal Dashpots. ....   | 121 |
| Figure A.3. Location of products of inertia in the matrix.....  | 121 |

# Nomenclature

- A = length of ellipsoid long axis
- B = length of ellipsoid intermediate axis
- C = length of ellipsoid short axis
- C = damping matrix
- e = constraint index
- f = vector of forces
- g = form factor for calculating the total length of edges in an isotropic planar aggregate
- F = transformation tensor
- G = transformation tensor
- H = transformation tensor
- $I_{XX}$  = moment of inertia given by  $I_{XX} = \int_{Vol} X^2 dV$
- $I_{XY}$  = moment of inertia given by  $I_{XY} = \int_{Vol} XY dV$
- $I_{XZ}$  = moment of inertia given by  $I_{XZ} = \int_{Vol} XZ dV$
- $L_{min}$  = minimum specified edge length for cell rearrangement algorithm
- K = elastic stiffness matrix
- n = number of nodes in a cell
- p = pressure in a cell
- q = the relative strength of the contraction along a cell-cell boundary for a lamellipodium
- r = fraction of the current number of cells that produce lamellipodia per unit dimensionless time  $\tau$
- S = the time scaling factor
- t = time

- $\mathbf{u}$  = displacements vector
- $\dot{\mathbf{u}}$  = displacement derivative vector
- $V$  = volume of a cell
- $\nu$  = unit vector
- $\Delta t$  = incremental time step
- $\Delta x$  = x distance from cell centroid to tetrahedron centroid
- $\Delta y$  = y distance from cell centroid to tetrahedron centroid
- $\Delta z$  = z distance from cell centroid to tetrahedron centroid
- $\Delta \mathbf{u}$  = vector of incremental displacement
- $\alpha$  = the orientation of the average long axis of the cells
- $\beta$  = the density of the cells in a specific region of a planar aggregate
- $\gamma$  = interfacial tension along a cell-cell interface
- $\kappa$  = the average shape factor of a group of cells (i.e., for the composite cell)
- $\kappa_i$  = the shape factor of one cell
- $\rho$  = interface density in a planar aggregate
- $\tau$  = dimensionless time
- $\xi$  = a coordinate for the local surface grid
- $\eta$  = a coordinate for the local surface grid
- $\zeta$  = the time constant for cell annealing
- $\Omega$  = the fraction of the current number of cells that divide per unit time
- $\psi$  = the dimensionless rate factor for mitosis
- $\mu$  = the effective viscosity of the cytoplasm
- $\chi$  = the rate factor for lamellipodium effect
- $\sigma_1$  = a principle stress in the long direction of the cell
- $\sigma_2$  = a principle stress in the short direction of the cell
- $\mu_A$  = stiffness of dashpot in the direction of A
- $*$  = used in a variable name as a substitute for any of the digits 1, 2, 3 or 4

# Chapter 1

## Introduction

### 1.1 Malformation: Birth Defect

Embryonic morphogenesis, the process by which a single cell becomes a multicellular embryo with structured tissues and specialized organs, involves complex changes of cell shape and multiple cell rearrangements [Gilbert, 2000; Alberts, *et al* 1998; Brodland, 2004; Hardin and Walston, 2004]. This process is one of the three fundamental elements of developmental biology, along with cell division and differentiation.

Embryonic cells and tissues evidently have their own intrinsic machinery to regulate these complex events so as to produce a consistent global outcome each time. However, when anomalies occur in these motions, serious and debilitating birth defects, such as spina bifida (Figure 1.1), can result.

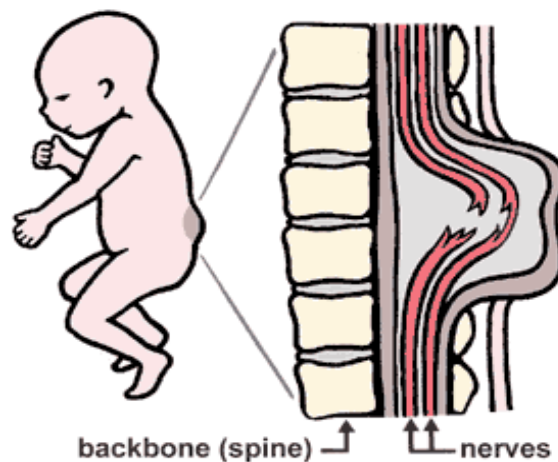


Figure 1.1. Schematic representation of spina bifida.

Spina bifida is the most frequently occurring birth defect and it often produces permanent disabilities. It results from the failure of the neural tube to close properly during a process called neurulation (Figure 1.2). When this condition occurs, the bones of the spine (vertebrae) above the open position of the spinal cord remain unfused and open. This can lead to the protrusion of the spinal cord through the opening. There is currently no cure for any nerve damage caused by spina bifida. To prevent the nerve from further damage and infection due to its exposure to the environment, the spinal cord and the nerve are surgically pushed back into the body and covered with meninges, muscle and skin.

To date, the exact cause of spina bifida remains poorly understood. Scientists have discovered that folic acid can significantly reduce the incidence of neural tube defects (NTDs). Indeed, when pregnant mothers take a folate supplement, the incidence of neural tube defects can be reduced up to 70% [Carter, 2005; Bjorklund and Gordon, 2006]. To seek the cause of NTDs, a full and fundamental understanding of embryonic neurulation from the perspectives of both physics and biology is required.

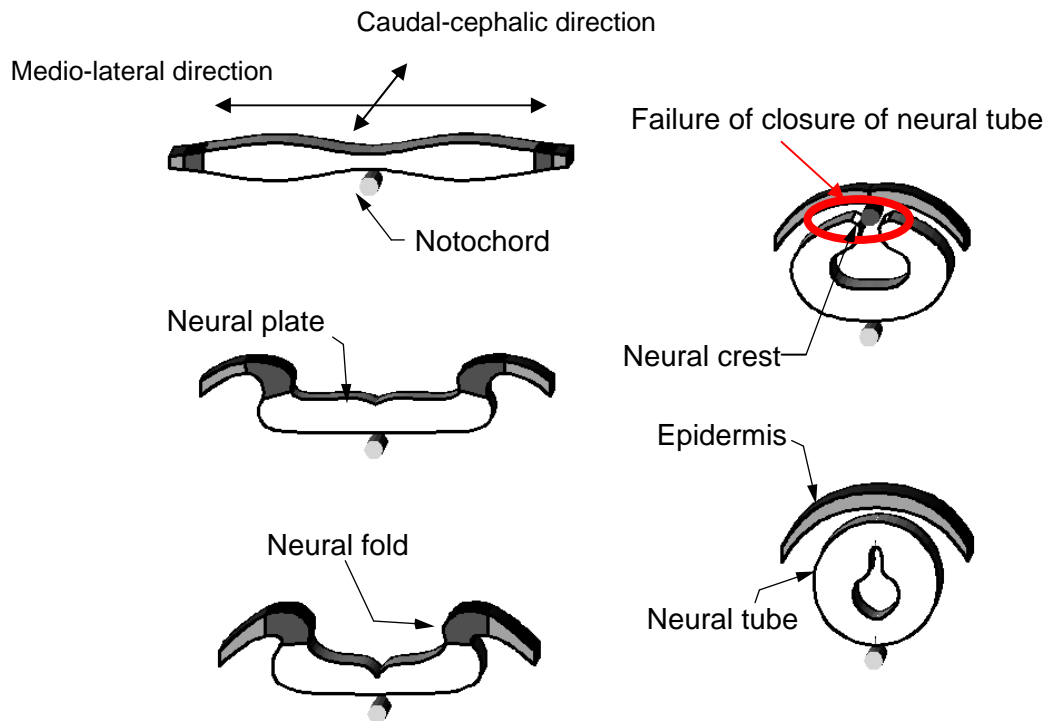


Figure 1.2. Schematic representation of embryonic neurulation

## 1.2 Fundamental understanding of neurulation

During the development of the vertebrate embryo, ectoderm cells form the epidermis and nervous system. A portion of the dorsal ectoderm is specified to become neural ectoderm (neural plate) and this tissue forms the neural tube by a process called neurulation. A schematic representation of embryonic neurulation is shown in Figure 1.2. The notochord initiates the formation of the central nervous system (CNS) by signalling the ectoderm germ layer above it to form the neural plate. The ectoderm above the notochord becomes significantly thicker and flatter than its neighbouring layer of tissue. During this stage, the ectoderm cells of the forming neural plate express unique molecular markers [Gilbert, 2000] and become wedge shaped. This change in cell shape leads to the rolling up of the whole neural plate and brings the neural folds towards each other. In the meantime, the ectoderm cells of the neural plate also experience a process called convergent extension [Keller *et al.*, 2000; Keller, 2005; Keller, 2006] during which the cells intercalate to elongate in the caudal-cephalic direction and narrow in the medio-lateral direction (Figure 1.2). This process also contributes to bringing together the neural folds. In the later stage of the rolling up process, the neural folds finally meet each other, merge, and release molecular markers which separate the forming neural tube from epidermis. The separated neural tube will later differentiate into the spinal cord and the brain, which eventually form the central nervous system.

## 1.3 Purpose and Motivation

Traditionally, embryological research has focused on identifying the molecular and genetic aspects of development [Huang and Ingber, 2005; Lecuit and Pilot, 2003; Pilot and Lecuit, 2005; Lee *et al.*, 2007; Krendel and Bonder, 1999], and relatively little effort has been devoted to understanding the relevant mechanics. From a reductionist point of view, during the past ten years, genome sequencing and high-throughput measurements have enabled scientists to collect comprehensive data sets on the underlying molecules. On the other hand, the abundant data did not advance our understanding of how to put these building blocks

together to generate collective behaviour such as neurulation. Identifying all the genes and proteins in a tissue or organism is like listing all the critical parts of a complex machine. The “user’s guide” which assembles them together to make the machine work, is obviously missing [Kitano, 2002]. Although folate holds much promise to prevent NTDs from happening, and textbooks have provided many figures and descriptions about neurulation, these facts do not reveal the mechanism of neurulation, the causes of NTDs, or the relationship of NTDs to other malformation defects.

The complex tissue motions and cell rearrangements involved in the neurulation process can only be studied effectively using advanced mechanics and numerical methods. Recent work [Swartz *et al.*, 2001; Stephanou and Tracqui, 2002; Chen, 2004; Robinson and Spudich, 2004; Brodland, 2004] has shown that mechanical processes must function in concert with chemical signal regulation and genetics to produce morphogenetic movements. The purpose of this research is to develop a systematic understanding of the mechanics of neurulation that is sufficiently rigorous and detailed so that it will lead to effective new strategies for reducing the incidence of neural tube defects (NTDs) in humans.

In order to explain the ways in which a computational model could be used, we begin by presenting a hypothetical physical analogy [Clausi and Brodland, 1993]. If one wanted to investigate how forces generated by systems of structural proteins might give rise to reshaping of cells and one had a sufficient budget to do so, one might construct a large-scale physical model of each of the significant structural elements in the system. To avoid the effects of gravity on such a system one might submerge it in water and make its components neutrally buoyant. One might use hydraulic cylinders to represent microtubules, computer-controlled linear motors to represent microfilaments, systems of dashpots to represent the cytoplasm [Brodland *et al.*, 2007], magnets to represent cell adhesion systems, microcontrollers and wires interconnecting these components to represent genes and signalling pathways, and other electro-mechanical devices to represent other protein systems.

If one were investigating mechanical interactions between several cells, one might need approximately a hundred such physical components. However, if one were investigating the mechanics of neurulation, tens of thousands of such components might be required.

In a typical simulation, one might position the components in some predefined starting configuration and on releasing the components and turning on their electromechanical control systems, observe how they would push and pull on each other and ultimately reconfigure themselves. If the motions so produced did not match those that occur in real cells having the initial geometry and morphology of the model, one could infer that the model is inaccurate. Either the properties of one or more of the structural components are incorrect or mechanical components are missing in the model. In either case, science is advanced because deficiencies in our understanding are identified.

If the model behaves the same as corresponding real cells, then one could alter specific model components so as to investigate how sensitive the pattern of motion is to changes in specific systems of structural proteins. Such information would be of value in accessing the degree of the changes that genes or signalling pathways would have to induce to produce a specified phenotype.

Although physical models have been used in the past to investigate how systems of forces might drive specific morphogenetic movements, computational models can do the same thing for much less cost and without the issues of friction and inertia, which would eventually plague a physical model.

Computational models have already revolutionized a number of health-related areas, including drug discovery, orthopaedics, hemodynamics and biomaterials. It is therefore not surprising that major efforts have been made to apply them to embryo biomechanics [Taber, 1995; Brodland, 2003 and 2004; Chen and Brodland, 2000; Brodland and Chen, 2000] and these efforts have been meeting ever increasing success due to the convergence of several critical technologies, including improved computational hardware, software algorithms and data collection modalities.

In the context of embryo morphogenesis, a suitably constructed computational model can address the following question: "If one had an embryo of specified geometry and if the

forces generated by its tissues, cells or structural proteins were known in detail, how would the cells and tissues in the embryo move?"

Because embryos have significant structure at several different scales – sub-cell, cell, and tissue – it is appropriate to use a “multi-scale” approach in modeling them. In a multi-scale approach, separate models are constructed at each of several length scales and findings made at one are passed to the other.

In the study of embryology, a current approach is to use a cell-level model to relate the forces generated by sub-cellular structural components to the properties of a sheet of such cells [Brodland *et al*, 2006; Brodland and Veldhuis, 2003; Brodland and Wiebe, 2004]. These cell-level models showed that cellular fabric – as characterized by average cell size, aspect ratio and orientation – is a key determinant of the forces in an epithelium. They also showed that complex interactions occur between cellular fabric, in-plane tensions, in-plane deformations, cell rearrangements, mitosis patterns and lamellipodium action. Known mechanical effects associated with gene expression are incorporated at this level.

These interactions can be described mathematically using a set of constitutive equations [Brodland *et al*, 2006]. These equations use current cellular fabric and the forces generated by specific sets of sub-cellular structural systems to calculate the in-plane loads that would be generated. A second group of equations then calculate the rate at which the tissue would deform if these tensions are not in balance with those applied to the tissue by adjacent tissues. The third group of equations calculates how the cellular fabric changes with time due to tissue deformation, cell annealing and other factors.

These equations make possible a tissue or whole-embryo model in which regions of tissue consisting of many cells are represented by a single finite element. The constitutive equations just described allow these elements to properly represent the highly nonlinear, non-continuum properties of the epithelium.

In the present study, Axolotl (*Ambystoma mexicanum*) embryos are used. Like a number of other amphibian embryos, they share important geometric similarities with human embryos and, for this reason, are often used as an animal model for neurulation.

## 1.4 What do we expect to learn?

If we put the geometric data and the mechanical property data from biological experiments into the computational model, we can test different hypotheses and verify our computational model by comparing the simulation result with the experimental data. By doing so, we expect to address the following questions:

1. Are the mechanical properties of abnormal tissues different than normal tissues?

Recent advancements in mechanobiology shed light on this question. Some of the relationships between the mechanical properties in tissue and the cytoskeletal structure in cells have been identified. In our research, detailed tissue stretching tests need to be conducted to extract the mechanical property data and compare them with normal tissues.

2. Can tissue behaviours or collective cellular behaviours be described by constitutive equations?

This is the key to the success of the computational model. Experimental data will play a critical role in addressing this question. Large amounts of data will be analyzed to derive suitable constitutive equations. The procedure can also be divided into some small questions such as, what parameters need to be defined in constitutive equations and how do they change with the tissue fabric evolution?

3. Can this computational model yield the normal case based on correct initial configurations and boundary conditions?

If our assumption about biochemical pathways changing the mechanical properties of tissue is correct, these unbalanced forces in tissue will reshape the tissue and drive the morphogenesis of the embryo. If the model can produce correct results, then we can increase our trust in this model. Otherwise missing mechanisms need to be incorporated into the model.

4. Can this computational model yield abnormal cases, and how sensitive is the model to these inputs?

This is another crucial question that needs to be addressed. The answer to the question will tell us how much perturbation needs to be introduced in order to produce a neural tube

defect. This will drive us to probe the various possible causes of NTDs including cases that arise from a combination of different causes. The sensitivity analysis of this model will help us to quantitatively evaluate the damage produced by different potential “causes” of NTDs and lay a foundation for devising methods to reduce the incidence of NTDs in humans.

5. What is the role of biomechanical feedbacks in the model?

Positive and negative feedbacks have been widely applied in system biology research. The genetic regulatory network can produce complex results with the help of these two feedbacks. Since in the discussion above we assume the genetic regulatory network determines the mechanical properties of tissue, we expect to see some positive feedbacks and negative feedbacks in our biomechanical model. Experiments and simulations will be carried out to prove the existence of these biomechanical feedbacks as well as the importance of them.

This thesis is organized as follows. A literature review dealing with biology background and computational models of embryonic morphogenesis is presented to provide an overview of the current research achievements. The computational model framework section will provide the details about our model including the objectives, underlying theory, and details of the computer implementation. Then, the results of the computational simulations will be discussed in detail. In the last section, conclusions and future work will be presented.

Because this work is built on the previous research work carried out in our lab, it is appropriate to summarize my contributions:

1. Ran cellular scale simulations to obtain rate constants for the tissue fabric parameters.
2. Modified constitutive equations to incorporate lamellipodium effect and verified the resulting new constitutive equations.
3. Proposed feature grids and wrote all of the codes for its implementation.
4. Wrote approximately 30% of the visualization software (my part consisted of approximately 10,000 lines of C++ code).
5. Wrote 20% of the code for the finite element engine (15,000 lines of C++ code).

6. Collected much of the biological and mechanical property data needed for the whole-embryo simulations.

7. Probed “necessary” input data and parameters to obtain realistic whole-embryo simulations.

8. Incorporated biomechanical feedback into the model.

# Chapter 2

## Literature Review

In this chapter several topics will be discussed. First, the biological background, such as the cell cytoskeleton and mechanobiology will be provided. Then there is a review of morphogenesis research from different perspectives, followed by introductions to current computational approaches for cellular scale and tissue scale models. Multiscale modeling techniques, which connect cellular scale and tissue scale models are then discussed. Finally, the elements used in our model will be presented.

### 2.1 Biological background

Through reductionist approaches, we can represent neurulation at several different scales (Figure 2.1). At the tissue scale, differences in mechanical properties of tissues induce the force imbalances needed to produce tissue motions in the embryo. To reach a force balance state, the tissues interact with each other mechanically and ultimately complete the neurulation process. At the cellular scale, cell-cell interactions determine the fabric of the tissue and in consequence determine the mechanical properties of tissues [Edelman, 1988]. At the sub-cellular scale, the cytoskeleton is responsible for changes in cell shape, alteration of cell-cell adhesions and cell self-rearrangements [Jamora, 2002]. In the following sections, we will discuss in detail the neurulation process from these levels. To facilitate understanding of the relevant biological terms, we begin at the sub-cellular scale.

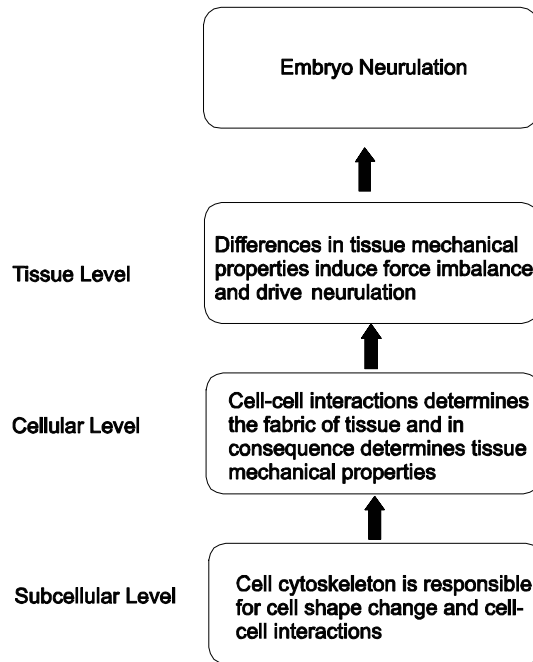


Figure 2.1. Neurulation mechanisms in different levels

### 2.1.1 Sub-cellular components

Like most physical structures, including buildings, cells acquire their shape from their internal “structure”, the cytoskeleton. By rearranging its own components, this dynamic

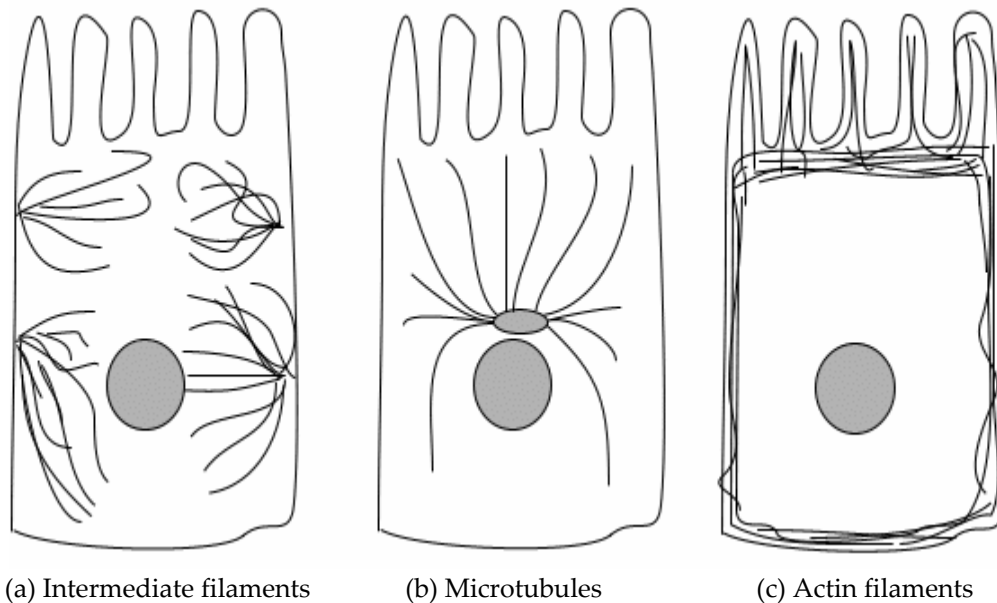


Figure 2.2. Schematic representation of cellular cytoskeleton [Alberts, 1998].

structure can maintain cell shape, drive cell motions, and play important roles in intra-cellular transport and cellular division. The cytoskeleton is built on three types of protein filaments: intermediate filaments, microtubules, and actin filaments (Figure 2.2).

### **1. Intermediate filaments**

Intermediate filaments are like ropes with many long strands of fibrous protein twisted together to provide great tensile strength. “Intermediate filaments are the most durable and toughest of the three types of cytoskeletal filaments” [Alberts, *et al.*, 1998]. A substantial amount of intermediate filament exists in cells. Its main function is to enable cells to withstand mechanical stress from its environment. Intermediate filaments are responsible not only for keeping the cell membranes from breaking but also for maintaining connections with other cells. The intermediate filaments in adjacent epithelial cells connect indirectly through the desmosomal junctions [Runswick, 2001] on the circumferential cell membrane. They form a continuous mesh network throughout the tissue (Figure 2.3). “This mechanical link strengthens the epithelium and is the basic strategy for the epithelium to obtain mechanical strength” [Alberts, *et al.*, 1998].

### **2. Microtubules**

Microtubules are long, hollow tubes with structurally distinct ends. The tubulin dimer, which is the main component of microtubules, can quickly dissemble in one location while reassembling at another location. Therefore microtubules can remodel themselves frequently by employing the free tubulin in the cellular cytoplasm.

The centrosome is the major center out of which microtubules in cells grow. With tubulin subunits,  $\alpha$  and  $\beta$ -tubulin alternating along the microtubule length, microtubules are polarized with a positive end and a negative end as shown in Figure 2.4. Normally microtubules negative-ends are anchored to the centrosome. The centrosome then controls the dynamic instability of microtubules in cells including the number of microtubules, their location and orientation in the cellular cytoplasm for particular purposes. For example, during mitosis microtubules switch between growing and shrinking more frequently than

they usually do. In addition, microtubules also play a critical role in transporting molecules and biochemical materials in cells. The transportation speed on the track of a microtubule is much faster than the diffusion in cytoplasm [Forgács, 2005].

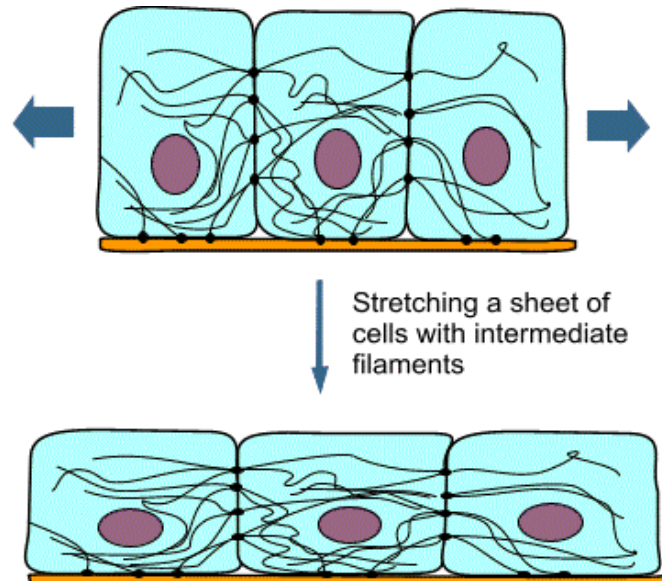


Figure 2.3. Intermediate filaments strengthen animal cells [Alberts, 1998]. If a sheet of epithelial cells is stretched by external forces, then the network of intermediate filaments and desmosomal junctions that extends through the sheet develops tension and limits the extent of stretching.

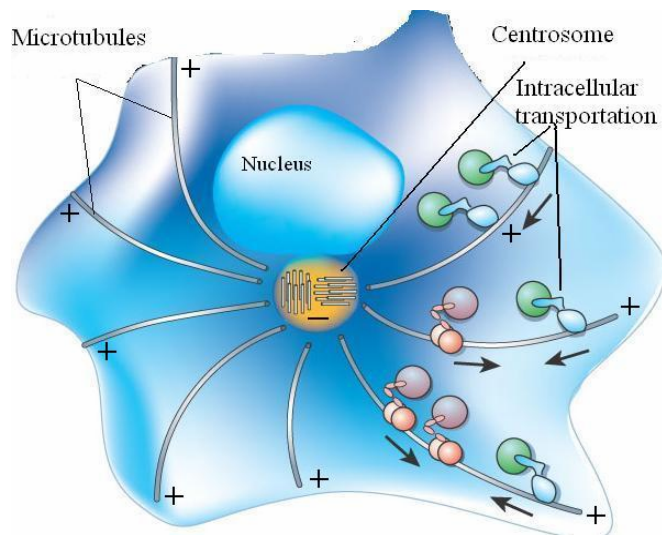


Figure 2.4. Microtubules are polarized and possess dynamic instability [Alberts, 1998].

Microtubules interact with the actin filament network through the jointed protein complex on the surface of the cell membrane [Ingber, 2005; Nelson *et al.*, 2005; Matthews *et al.*, 2006]. In a typical situation, microtubules can bear certain compression force generated by actin filaments. However, when the microtubules cannot sustain this force, they will disrupt, thereby increasing the substrate traction [Lauffenburger and Wells, 2001]. In this way, the actin filament bundles, adhesion junctions and microtubules interplay to maintain a balance of contractibility close to the apical surface [Adams and Nelson, 1998].

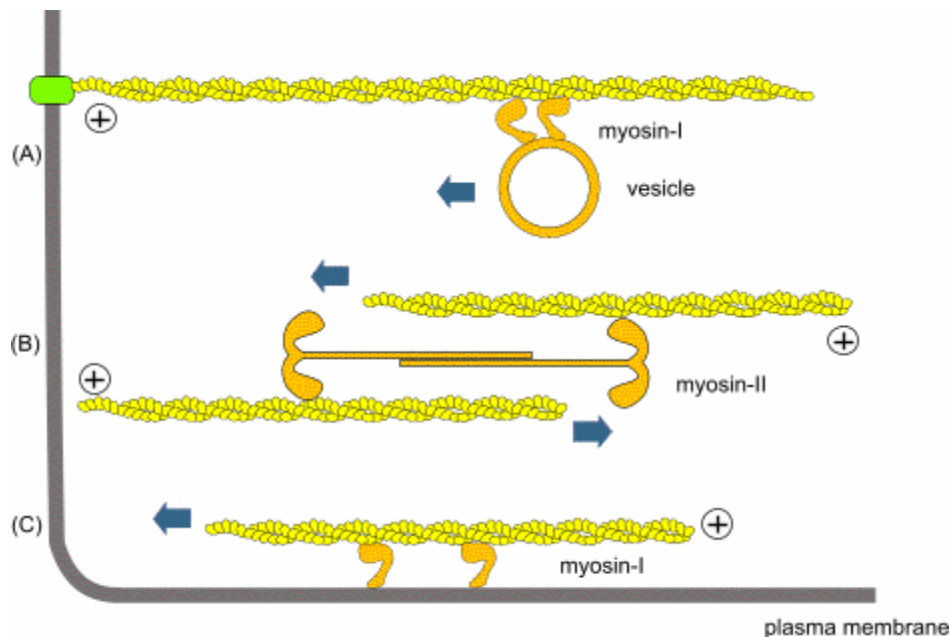


Figure 2.5. Some roles of myosin-I and myosin-II in a eucaryotic cell [Alberts, 1998]. The short tail of myosin-I molecule contains sites that bind to various components of the cell, including membranes. This allows the head domain to move a vesicle relative to an actin filaments (A), or an actin filament and the plasma membrane relative to each other (C). Small filaments composed of myosin-II molecules can slide actin filaments over each other, thus mediating local shortening of an actin filament bundles (B).

### 3. Actin filaments

Actin filaments are thin flexible helical polymers of the protein actin. They are normally organized into bundles and cross-linked exhibiting complex two dimensional or three dimensional networks [Gardel *et al.*, 2006; Shin *et al.*, 2004]. Because they are most highly concentrated in the cortex, which is just beneath the plasma membrane, they have a great

impact on the cellular movements [Alberts, 1998; Wilt and Hake, 2004]. The contractile ability of actin bundles owes to their interactive binding with myosin, a mechanism also adopted in the muscle cells. Myosin-I and myosin-II are the two abundant subfamilies of myosin. The head domain of myosin-I interacts with actin filament and the tail domain determines which surrounding cell component should be attached (Figure 2.5). Myosin-II molecules have two heads and one tail domain. Like myosin-I, their head domain interacts with actin filaments, while the tail domain only interacts with its peer (Figure 2.5). By sliding actin filaments in opposite directions, myosin-II generates contractile force in actin filament bundles, which holds responsibility for deforming, or pulling the membrane into a different shape. In general, actin filaments play a critical part in mediating cell shape [Vasioukhin *et al.*, 2000; Vasioukhin and Fuchs, 2001; Pollard, 2003].

## **2.1.2 Cell-cell interactions**

### **1. Cell-cell adhesion**

By definition, biological tissues such as the nervous, muscle, epithelial and connective tissues are a collection of interconnected cells that perform a similar function within an organism. Cells tend to stick to other cells by employing specific cell adhesion molecules (CAMs) on their surfaces [Gumbiner, 1996]. The extracellular matrix, which is secreted by cells themselves, is also involved in assembling cells to construct biological tissue. A schematic overview of major adhesive interactions that bind cells to their peers and the extracellular matrix is shown in Figure 2.6. The apical (upper) surface of these cells is packed with finger like microvilli that are exposed to the lumen while the basal (bottom) surface rests on a thin sheet of extracellular matrix (ECM), called basal lamina. The junctions between cells and ECM can be categorized into these two types: providing mechanical strength and not providing mechanical strength. The cell-cell adhesion junctions such as adherens junctions and spot desmosomes are mediated by cell-adhesion molecules (CAMs). The cell-matrix adhesions junctions such as hemidesmosomes are determined by adhesion receptors binding to various components of the ECM. These cell adhesion proteins not only hold cells together to construct biological tissue but also play important roles in cell-cell and

cell-environment biochemical signalling [Braga, 2000]. The other types of junctions include tight junctions and gap junctions (Figure 2.6). Tight junctions, lying just under the microvilli, prevent the leakage of molecules through extra-cellular spaces between cells. Because there is no significant amount of cytoskeleton components attached to tight junctions, they do not provide mechanical strength. Unlike tight junctions, gap junctions allow the movement of molecules and ions through connection channels between the cytosols of adjacent cells. Therefore gap junctions are responsible for signalling between the cells.

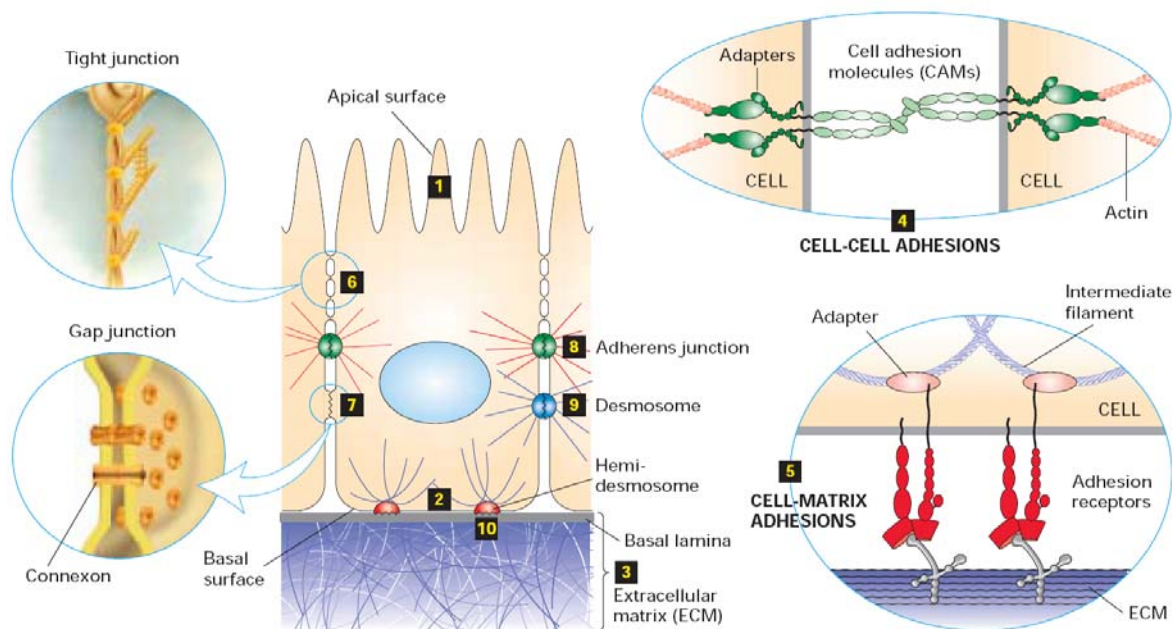


Figure 2.6. Schematic overview of major adhesive interactions that bind cells to each other and to the extracellular matrix [Lodish, 2000]. 1. Apical surface 2. basal surface 3. extracellular matrix(ECM) 4. cell-cell adhesions 5. cell-matrix adhesions 6. tight junction 7. gap junction 8. adherens junction 9. desmosome 10. hemidesmosome

## 2. Mechanotransduction and mechanosensation

“Of Aristotle’s five senses, sight, smell and much of taste are initiated by ligands binding to G-protein-coupled receptors. However, the mechanical sensations of touch and hearing remain unknown without a clear understanding of their molecular basis” [Kung, 2005]. This kind of mystery brings great difficulties to biomechanical models predicting the common behaviours of different type of cells and tissues. Due to these factors, the research on cellular

scale mechanics has leaned towards biological experiments instead of modeling in recent years. The new term “mechanobiology” has been gaining more attention due to the huge improvements in experiment methods and instruments. To date, much less is known about cellular mechanotransduction -- the conversion of external mechanical forces on living cells into a biochemical response that changes the gene program and mechanical properties.

As mentioned above, some of the cell-cell adhesion junctions provide mechanical strength and some do not. Things would be simple if cells were static and their mechanical properties could be determined by those specific adhesion junctions. The reality is cells are alive, and they remodel their structure and shape from time to time. Even small perturbation on the cell membrane may lead to remodelling of cell-matrix and cell-cell contact. There are two main viewpoints reported on the mechanotransduction in recent studies.

1. Mechanosensitive ion channels and lipids

Many cell membranes are equipped with mechanosensitive (MS) ion channels that respond to turgor in proportion to the surrounding concentration of water, which means the MS ion channels act independently of lipid bilayers. However, recent studies have indicated that lipids are also involved in the gating of MS channels. When the interface between the lipids bilayer and MS channels is under stress or other externally applied force, the MS channel protein will change its conformation making a switch between open and closed. And also by changing the lipids' shape, the membrane can exert force on the MS ion channel and open its gate [Chin, 1997].

2. Cytoskeletal tension, integrins, Rho and MS ion channels

This hypothesis puts together cytoskeleton, cell-cell adhesion junctions and MS ion channels. Its main idea is that the whole cell is the mechanotransducer because it integrates these local signals with other environmental inputs before eliciting a specific behavioural response. The cell-cell and cell-matrix adhesion junctions can transfer force to the whole cell in a short time span. A corresponding experiment was conducted to verify this thought. Ingber embedded microbeads (4.5  $\mu\text{m}$  diameter) on the surface membrane of cultured capillary endothelial cells using permanent magnetic pulling cytometry. The microbeads are

coated with a synthetic RGD peptide that binds to integrin receptors. These RGD-beads ligate and activate integrin receptors, and form focal adhesions. A 3-second force pulse was applied on these microbeads and results show that the whole cell tends to respond viscoelastically to mechanical stimuli immediately. Obviously the MS ion channel theory will not be able to predict this phenomenon because the diffusion of solute or molecular transportation has a time lag longer than 3 seconds. Ingber [Ingber, 2003 I; Ingber, 2003 II] uses tensegrity structure to describe the prestress cytoskeletal network in cells [Stamenovic and Ingber, 2002; Rosenblatt *et al.*, 2006]. Tensegrity structure is a special prestressed structure. Its stiffness is zero when no prestress is applied in the structure. The prestress can transfer externally applied force to its whole structure isometrically at a very quick speed when the prestress in the structure is high. Local integrin-cytoskeleton linkages within bead-associated focal adhesions exhibit an immediate viscoelastic response due to the special properties of tensegrity structure.

From a mechanical perspective, the difference between the two opinions about the mechanism of mechanotransduction is not huge. Both of them can be explained by prestressed structures and conformation change of MS ion channels. The former one can be viewed as a prestressed water balloon and the later one can be viewed as a prestress tensegrity structure. The prestress effect makes the changes of local force spread to global structure and change the conformation of MS ion channels.

### **2.1.3 Basic morphogenetic movements**

Biological tissue is a collection of interconnected cells that perform a similar function within an organism. Because of the mechanical property changes in cells, there are a total of eight basic morphogenetic movements occurring in the developing organism. Figure 2.7 is the schematic representation of the eight basic morphogenetic movements. Although morphogenetic movements are categorized in this way, we may not be able to observe the neat, tidy example of each kind. In a real case these movements occur at the same time and are coupled together which makes the morphogenesis even more complex.

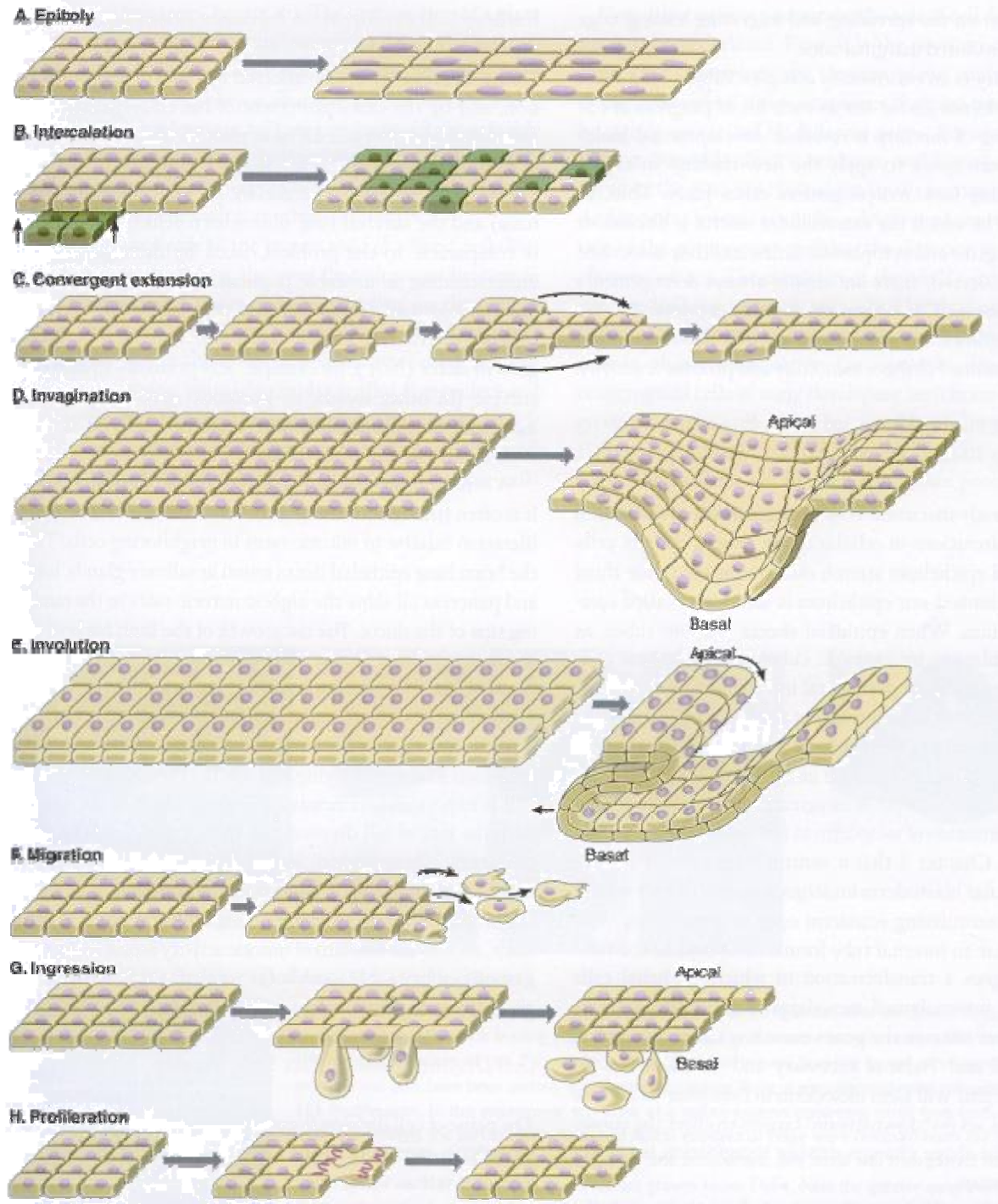


Figure 2.7. The eight basic morphogenetic movements in tissue scale [Wilt and Hake, 2004].

## 2.2 Morphogenesis research progress

Although our research and this report are focused on embryonic neurulation, this does not restrict our discussion from general morphogenesis research. Embryonic morphogenesis is one of the most intriguing events during embryonic development, and has attracted much attention, especially over the last few decades. Scientists from biology, mechanics, chemistry, applied math and other research fields are trying to interpret morphogenesis “in their own words”. In the following section we will track the development and progress of these research fields and draw a conclusion that an interdisciplinary approach is critical for morphogenesis research.

### 2.2.1 Biological perspective

Before molecular biology or biochemistry took the dominating position in the science of biology, biologists usually described biological phenomena in terms of mechanics. What they had done was observe the motions of cells and shape changes of the whole-embryo, and push back the question to the previous stage. It was the immediate cause of those biological phenomena that they were seeking. Although some attempts have failed, the mechanical viewpoint, the essence of design, still has value in biological research. However, appreciation of mechanics and form fell away as the 20th century progressed. The quintessential experiment, “the one gene one enzyme hypothesis” of Beadle and Tatum [Beadle and Tatum, 1941], first connected the genotype to phenotype. Henceforward the mainstream of biology switched to gene and biochemical research [Kirschner *et al.*, 2000]. Molecular biology became a very productive research field. Scientists focused on finding biochemical pathways and gene expression to “explain” organogenesis and pattern formation exclusively. However the understanding of how nature builds tissues with specialized form and function is still missing. The reductionist approaches seem not to have the final answer. The complexity theorist, Stuart Kauffman tried to study the “emerging global civilization” in biology by conducting the first computational simulations of a genetic regulatory network [Kauffman, 1969], which is similar to the famous cellular automata model.

At the same time, the demands for complexity theory in other research fields such as computer science, economics and sociology was growing rapidly. These changes drove the research in biology in a new direction, which can be viewed as a primitive form of system biology. Application needs and research advancements promoted the research trends into exploring the global outcome of biology systems. System biology seems to have a promising future in the upcoming 10 years because “system biology offers an opportunity to study how the phenotype is generated from the genotype” [Kirschner, 2005]. Although system biology presents us with high expectations in biology research, it does not provide us with satisfying solutions in morphogenesis related research or a more precise understanding of the physical world. We continue to wonder what is missing in the very first place. In seeking the answer, “there has been a recent resurgence of interest in mechanical forces as morphogenetic regulators” [Ingber, 2005]. With the advancement of biophysics instruments, many experiments have been conducted to prove that the mechanical forces, which had been largely ignored since the rise of molecular biology, play a critical part in embryonic development [Huang and Ingber, 2005; Ingber 2005; Scott and Stainier, 2003].

### **2.2.2 Chemical or applied mathematics perspective**

A. M. Turing (1921-1954) was one of the foremost thinkers in the morphogenesis research field of the 20<sup>th</sup> century. His famous paper “The Chemical Basis of Morphogenesis” tried to “demonstrate that systems of mutually reacting and diffusing chemicals could be used to illustrate the mysterious origin of biological form with a previously formless structure – for example within a developing embryo” [Sekimura, 2003]. The word “morphogenesis” in that scenario is more precisely “pattern formation”. Turing believed that morphogens are capable of diffusing in a tissue without much hindrance. The beautiful diffusion-reaction equations are used to describe the diffusing movements and become the foundation of mathematical biology. The instability of the whole system is already embedded into the equations and dramatically different results can be expected with the introduction of different stochastic factors. The essence of mathematical biology depends on striving for “deep” explanations. However, experimental biology is still largely descriptive. The two

different cultures make it difficult for experimental biologists to recognize the work of mathematical biologists. With the huge advancements in biophysics and biotechniques, the situation is becoming more and more promising. Biologists seem to be ready to accept mathematical biology models in different research areas from molecular biology and cellular biology to tissue research. A number of models [Sekimura, 2003] with revised mesh or governing equations have emerged and help people to understand biology problems in a more quantitative and accurate way.

### **2.2.3 Mechanical perspective**

In the physical or mechanical viewpoint of morphogenesis, D'Arcy Thompson has been the pioneer in interpreting biology in mechanics. His book *On Growth and Form* brought the opinion that “the form of an object is a diagram of forces” [Thompson, 1992], and this is probably the foundation of relating biology with mechanics. With developments in solid mechanics and numerical analysis methods, computational mechanical simulations play important roles in many research fields. The founder of modern biomechanics, Fung, Y.C. introduced mechanics in biological research and gained great success in applications [Fung, 1981]. The biomechanics in embryonic morphogenesis also attracted many researchers [Brodland, 2004; Brodland, 2005; Belousov, 1998; Belousov, 1998; Belousov, 2006; Glazier, 1993; Graner, 1992; Munro and Odell, 2002; Odell *et al.*, 1981; Taber, 1995; Taber, 2007; Zone, 1996]. Different mechanical models have been proposed. They have succeeded in a certain way. These models all proved that mechanical models have the capacity to produce highly complex geometries given appropriate positive feedbacks and negative feedbacks [Taber, 2007; Shraiman, 2005]. However embryonic morphogenesis is also closely associated with gene expression and biochemical pathways. Positive and negative feedbacks are apparently largely controlled through these networks. The accurate input of positive feedbacks and negative feedbacks becomes very critical. Simulations are delayed due to the lack of sufficient knowledge as to how genetic regulatory networks function and how to map biochemical pathways into mechanical pathways. The general finite element method has gained great success in studying non-biological system, but it lacks accurate descriptions of

mechanical properties of biological systems. This makes it difficult to conduct simulations [Taber, 1995].

Many computational models concerning embryonic morphogenesis have been proposed by scientists from different research fields over past decades. What follows is a review of current computational models in cellular scale and tissue scale that deal with embryonic morphogenesis.

### **2.3 Cellular scale model and tissue scale model**

During embryonic development, cells may experience passive shape change, active shape change, growth, division, and rearrangement. These motions all contribute to embryonic morphogenesis. In a successful model, all these motion types should be incorporated into the model in the form of parameters or modules. Although these cell motions or processes are generally linked, most investigators tend to treat them separately. To simplify the description of embryonic morphogenesis, the deformation of embryonic epithelia during morphogenesis is usually categorized into two groups, local shape change and global shape change [Taber, 1995].

Local shape change describes the epithelia out-of-plane deformation, which includes invagination, evagination, and folding. Invagination is the process of forming pockets that sink into a structure (Figure 2.8a). Evagination is the process of forming buds that arise out of a structure (Figure 2.8b). Folding is the action in which structures bend, touch, and join (Figure 2.8c). Global shape change represents the epithelia in-plane deformation, which includes surface area changes and constant area cell rearrangements (Figure 2.9).

To study these shape changes during embryonic morphogenesis, two kinds of computational models are employed: cellular scale models and tissue scale models. Cellular scale models involve studying embryonic morphogenesis from the perspective of cell motions and interactions. In the cellular scale model, details about cells must be described and provided to run simulations, and cell motions must be tracked during the whole process.

In tissue scale models, embryos are divided into finite elements with different descriptions of mechanical properties. Tissue (element) properties become the focal point instead of cell motions. Since local shape change usually involves large deformation in a three dimensional (3D) space, tissue scale models are widely used to study local shape change.

Our research work focuses on the relationships between cellular scale models and tissue scale models. So both models will be reviewed here. The literature on computational models for embryonic morphogenesis is vast. In this report, cell rearrangements (global shape change) and embryo neurulation (local shape change) will receive more attention.

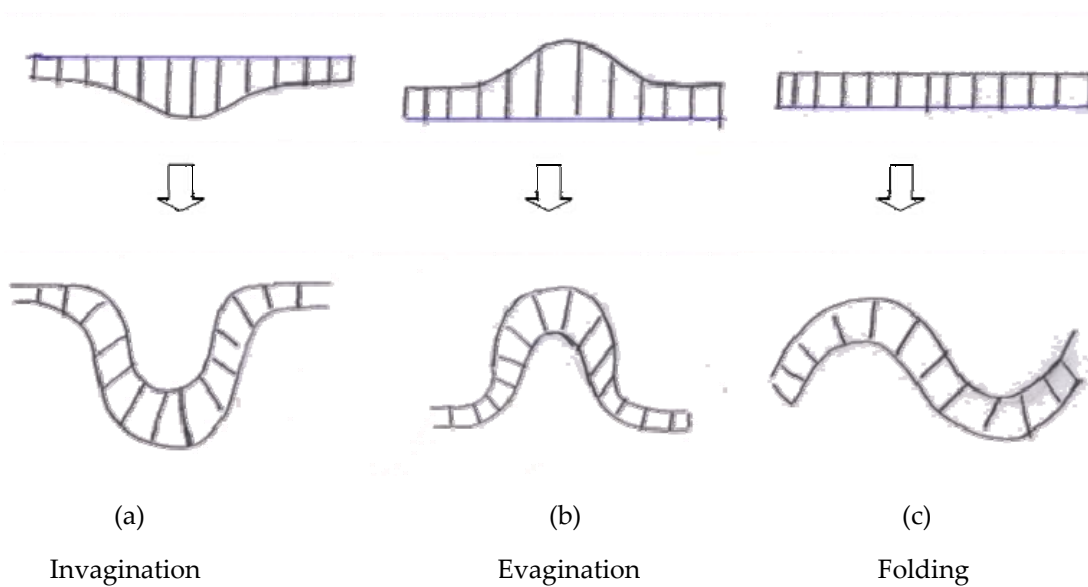


Figure 2.8. Invagination, evagination and folding of epithelium [Fristrom 1988].

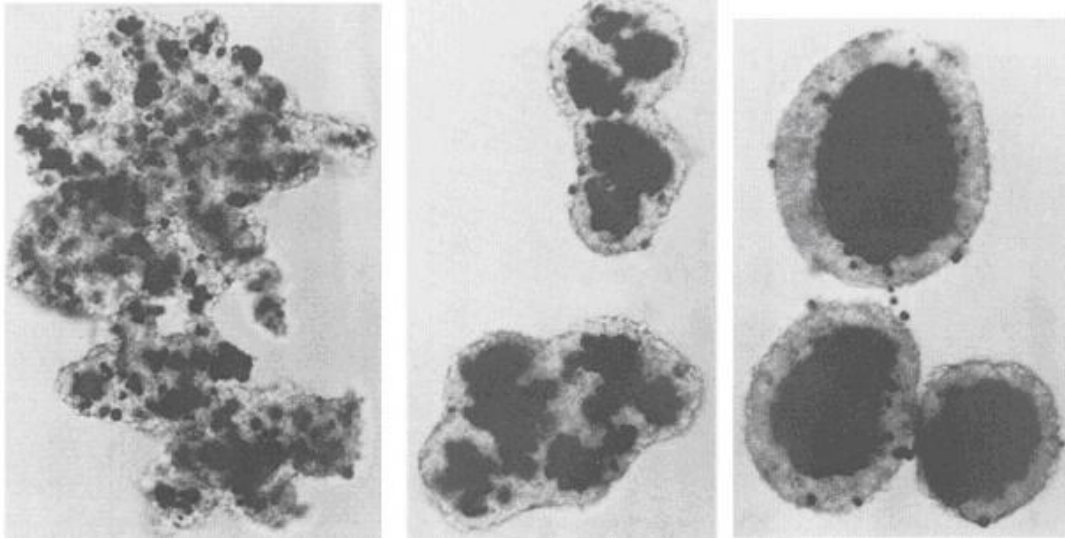


Figure 2.9. Cell sorting [Brodland 2004].

### 2.3.1 Cellular scale model

Hypotheses concerning the driving force of cell rearrangements include the differential adhesion hypothesis (DAH), differential surface contraction hypothesis (DSCH), specific CAM-based hypotheses, and Differential Interfacial Tension Hypothesis (DITH) [Brodland, 2002; Brodland, 2004]. Which is the driving force, adhesion or interfacial tension (surface tension)? Although this is still under debate, recent experiments have suggested that the interfacial tension might be the critical factor instead of adhesion, contrary to what was reported in former theoretical models and experiments. When these hypotheses are implemented into the computational models, all the governing rules are usually described with the length or the weighted lengths of cell-cell interface.

In essence, the primary difference between the different computational models is the descriptions of cell shape or structure, while the objectives are almost the same, namely finding a local state of minimum energy or a configuration of force equilibrium. These models will be introduced one by one.

## 1. Cell-lattice models

Cell-lattice models [Brodland, 2004] are similar to the famous model “cellular automata”. By using regular squares or hexagonal lattices to describe cell shape [Gordon and Goel *et al*, 1975; Goel and Campbell *et al*, 1970; Goel and Rogers, 1978; Rogers and Goel, 1978], this model saves a lot of computational running time.

The basic idea of this model is to find the lowest free energy state of the system by exchanging the position of neighbouring cells (Figure 2.10). The possibility of exchanging the position of two cells is determined by evaluating the energy change of the whole system. Different implementations may have different evaluation criteria. Some models use probability decision mechanisms while most of the others use a threshold value policy. If a probabilistic decision mechanism is used, this approach can be viewed as a Monte Carlo simulation.

The strength of this model is that it is straightforward to program and has short run times. Although this model is surprisingly effective in modeling real cell aggregates (Figure 2.11), the behaviour of cell position exchanging in this model is not observed in real embryos, which prevents this model from reflecting the real process of cell rearrangement.

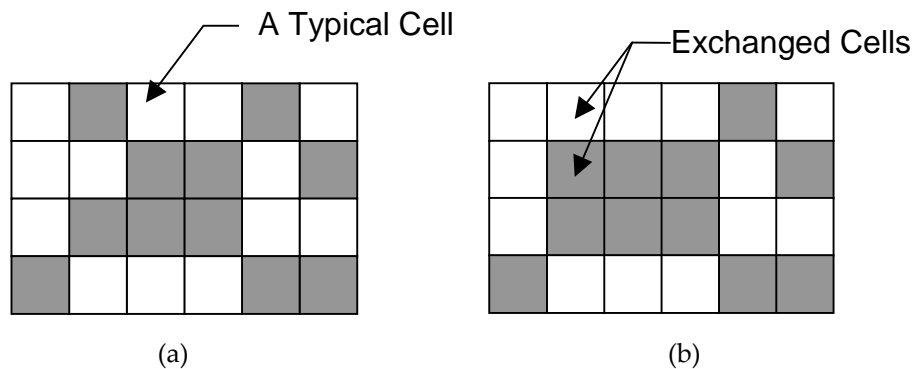


Figure 2.10. Cell Exchange in a Cell Lattice Model [Brodland 2004]. Each cell occupies one square in the mesh. Different color represents different cell type.

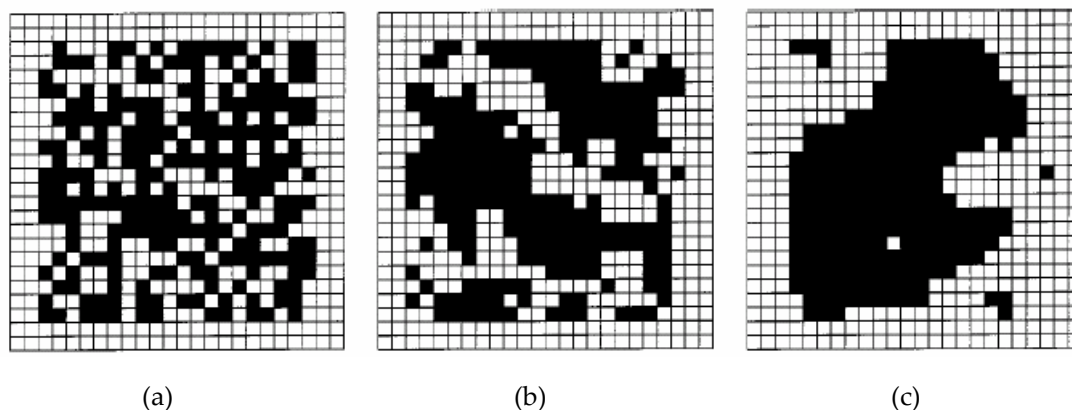


Figure 2.11. Simulation of cell sorting by cell exchanges [Gordon *et al.*, 1975]. (a) The initial configuration; (b) An intermediate state; (c) The final state of the system.

## 2. Centric models

Centric models by Honda [Honda 1978, Honda 1983, Honda 1986] use Dirichlet or Voronoi tessellations to describe cells in aggregates. In a Dirichlet or Voronoi tessellation, forming points define the whole system. Each forming point controls one area, and the forming point is closest to all the points in its area compared with other forming points (Figure 2.12). By randomly placing forming points in the plane, an initial configuration is generated.

The basic idea of this model is that a forming point will make a certain displacement, which is determined by complex calculations in each iteration step, to minimize the free energy of whole system based on cell-cell boundary lengths. In each step, forming point motion will cause a re-meshing of the whole plane, which means updating the geometry of the cell aggregate.

This model is effective for describing single cell shapes and simulating cell sorting (Figure 2.13). The intrinsic drawback of this model is that the cell shape is determined by Voronoi tessellation rules, which prevent modeling of aggregates with anisotropic cells.

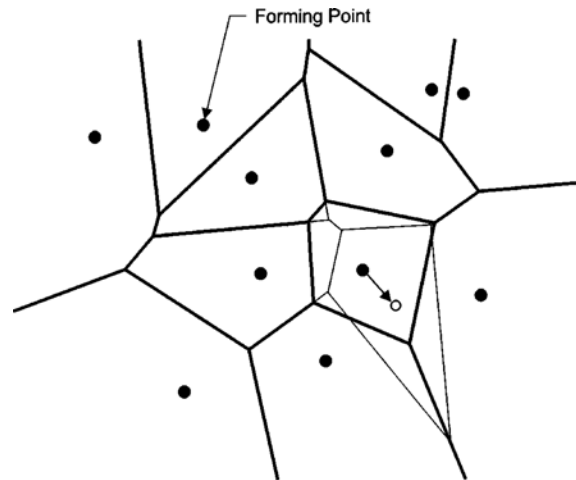


Figure 2.12. Cell-centric model [Brodland, 2004]. A voronoi tessellation determines the configuration of cell aggregates. The dark lines represent the current cell aggregate configuration, and the light lines represent the next cell aggregate configuration.

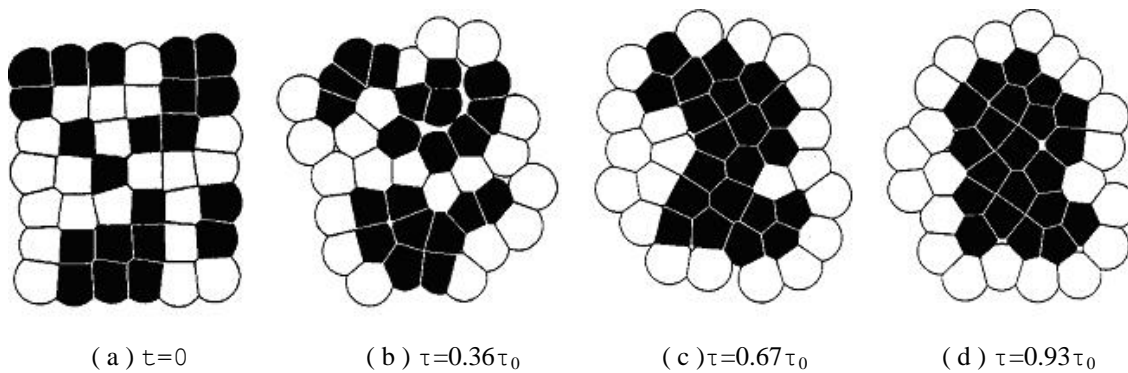


Figure 2.13. Simulation of cell sorting using a cell-centric model [Graner and Sawada 1993]. a) the initial configuration; b) and c) an intermediate state; d) the final state of the system.

### 3. Sub-cellular lattice models

Sub-cellular lattice models [Glazier and Graner 1992, Glazier and Graner 1993; Rieu, 1998] are a substantial enhancement from cellular lattice models. The difference is the number of squares that are used to describe one cell. In cellular lattice models, each cell only occupies one square while in sub-cellular lattice models each cell can occupy multiple squares (Figure 2.14). Some constraints for maintaining these squares into one aggregate are introduced in sub-cellular lattice model.

One advantage of sub-cellular lattice models over cellular lattice models is the description of cell shape. With more squares, the description of cell shape in sub-cellular lattice model is better than cellular lattice model. However, the shape description always has jagged boundaries. In addition, this approach does not adequately model the mechanical effects of the cell cytoplasm.

#### 4. Boundary vertex models

Boundary vertex models [Honda 1983, Honda 1986] employ vertices and polygons to describe cell shape (Figure 2.15). The basic idea of this model is that each vertex moves so as, to shorten the total length of the cell-cell boundaries. In some models, an algorithm of weighted boundary length is used [Honda 1983, Honda 1986].

The approach used in this model can be summarized as follows: One cell-cell boundary is chosen at random in each iteration step (Figure 2.15), node P and Q can move in the direction of AB and CD respectively. By adjusting the movement of P and Q, the length  $AP'+BP'+P'Q'+Q'C+Q'D$  can be minimized.

The approach belongs to the boundary-shortening method. The drawback of these boundary-shortening methods is that they do not incorporate the mechanical effects of cell cytoplasm. Thus, an objective time factor is lacking in these models.

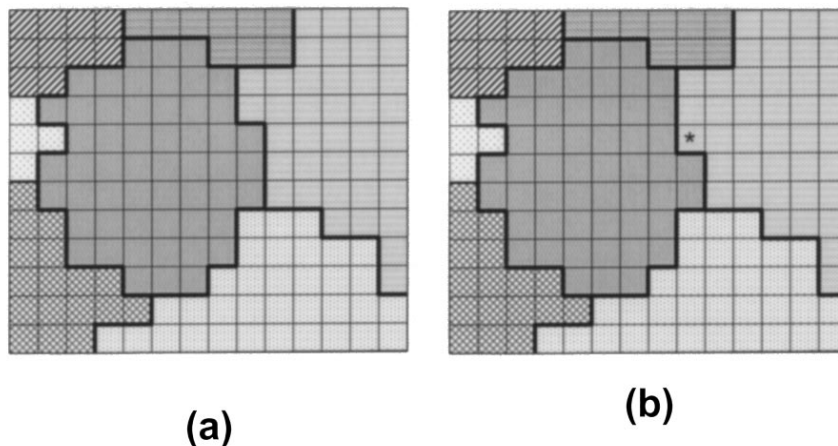


Figure 2.14. Sub-cellular lattice model [Brodland 2004]. Each cell occupies an area surrounded by dark lines. Cell shape changes are implemented by changing the cell type of each site. In (b) the cell type in the site marked with an asterisk is changed.

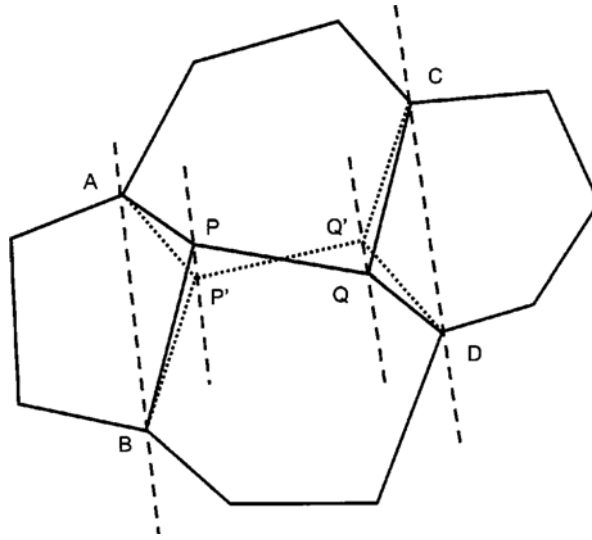


Figure 2.15. Vertex model [Honda 1986]. Cell shape changes are implemented by moving a pair of vertices P and Q.

## 5. Finite element models

In a finite element model [Chen and Brodland 2000], polygonal elements realistically model the geometries of each cell. Material properties can be assigned to each element and they can be used to model the viscosity of cell cytoplasm. The driving force for cell arrangement in this model is the interfacial tension on each cell-cell boundary. The objective of this model is to find the time course of motion. Details about this model will be discussed in Chapter 3, so only some key points in this model will be introduced here.

1. Each cell is divided into discrete finite elements. (Figure 2.16) Each triangular element has a rod element on each edge. The rod element will generate constant contracting force in its longitudinal direction during the whole process.
2. The global effective stiffness (damping) matrix is based only on cell cytoplasm viscosity. Rod element and triangular element have no contribution to the global stiffness matrix.
3. The viscosity  $\mu$  is introduced in the model to replicate the forces produced by cytoplasm deformation.
4. A Lagrange multiplier is imposed to keep a volume of each cell constant.

This finite element model can simulate a wide range of cell action phenomena (Figure 2.17). Based on a strict mathematical derivation, this model provides a general way to

perform computational simulation of cell rearrangements. With the advance in computing technology, finite element models provide a means to simulate morphogenetic events in biological systems.

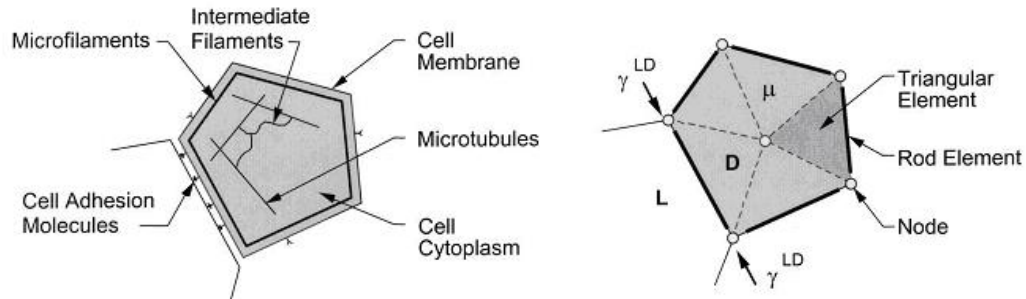


Figure 2.16. Schematic cell cross-section and its corresponding finite element model [Brodland 2004].

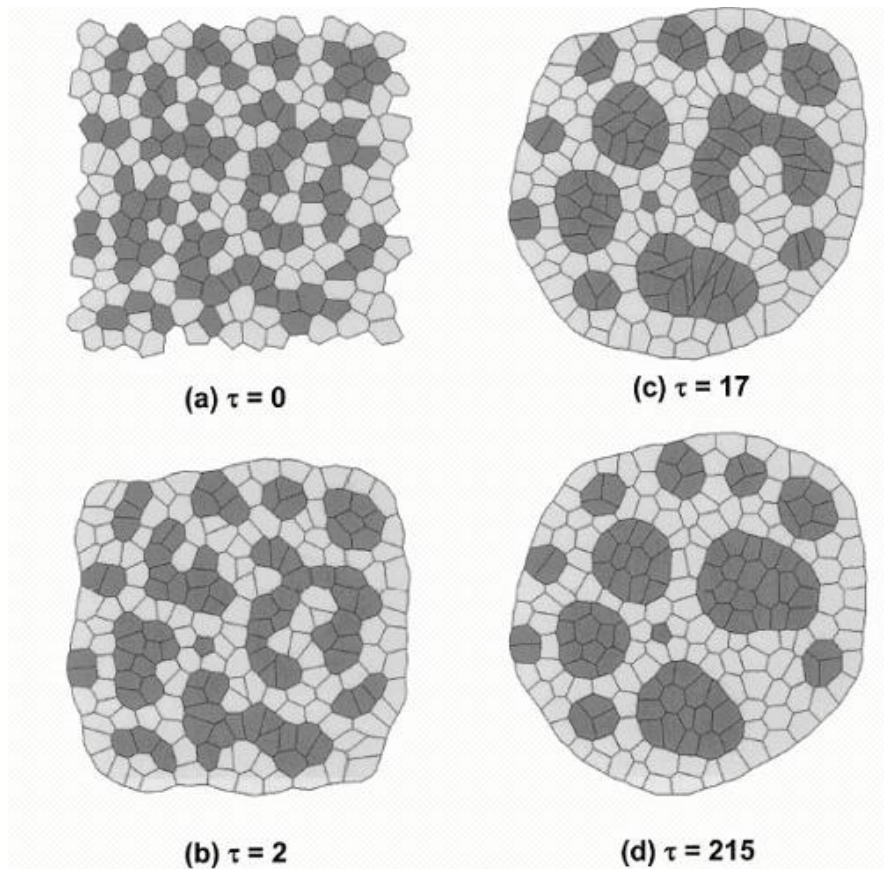


Figure 2.17. Simulation of cell sorting using finite element model [Brodland 2004]. a) the initial configuration; b) and c) an intermediate state; d) the final state of the system.

The comparison of these models is listed shown in Table 2.1.

**Table 2.1 Comparison of different models:**

| <b>Approach</b>                      | Cellular lattice models | Sub-cellular lattice models | Centric models                               | Boundary Vertex models          | Finite Element models                |
|--------------------------------------|-------------------------|-----------------------------|--|---------------------------------|--------------------------------------|
| <b>Description of cell shape</b>     | Square                  | Stepped polygons            | Arbitrary polygon, but restricted by Voronoi | Arbitrary polygon               | Arbitrary polygon                    |
| <b>Objective</b>                     | Minimize the energy     | Minimize the energy         | Minimize the energy                          | Minimize the cell-cell boundary | Mechanical equilibrium configuration |
| <b>Governing rules for iteration</b> | Cell position exchange  | Cell type change            | Forming point movement                       | Vertex movement                 | Vertex movement                      |
| <b>Description of cell cytoplasm</b> | NO                      | NO                          | NO   | NO                              | YES                                  |
| <b>Real Time relevance</b>           | NO                      | NO                          | NO   | NO                              | YES                                  |
| <b>Time cost</b>                     | Low                     | Modest                      | Modest                                       | Modest                          | High                                 |

## 6. CompuCell Project

As mentioned in the introduction, the genetic regulation network and morphogen gradient play a critical role in mediating the cell morphogenesis. Quite a few models exist to incorporate the genetic regulatory networks and morphogen fields. CompuCell project is one of them [Izaguirre, 2004]. It is a computational framework for simulation of the “coupling between genetic regulatory networks and diffusion of morphogens, cell adhesion, haptotaxis (movement of cells along a gradient of a molecule deposited on a substrate), and chemotaxis (movement of cells along a gradient of a chemical diffusing in the extracellular

environment)" [Izaguirre, 2004]. It consists of three main modules: "Cellular Potts model (CPM) that describe cell and ECM behaviours, a Reaction-Diffusion (RD) module that describes diffusible morphogens and a combined ordinary differential equations (ODE) /state model of genetic regulatory networks and differentiation" [Izaguirre, 2004]. Cellular Potts Model is a generalized cellular automata. It is evolved by updating the cell lattice one pixel at a time based on a set of probabilistic rules. It is based on the differential adhesion hypothesis by minimizing the energy of cell-cell surface interaction. One difference that separates it from most current cell-lattice models is that constraints are imposed by introducing a Hamiltonian or effective energy function. Divergence from the designated behaviour will result in an "energy penalty". The other difference is that CompuCell provides the option to use continuum models to model cell dynamics. The genetic regulatory networks in CompuCell are a set of rules for cells that govern their growth, division, secretion of morphogens, and strength of adhesion. Most of these rules are concerned with the morphogen density in cells. This mechanism correlates genetic regulatory networks with the Reaction-Diffusion module and brings more complex behaviours into the model.

CompuCell is an open-source object-oriented project, and its comprehensive modules are attracting more attention in recent years with the development of systems biology. The introduction of genetic regulatory networks into computational models is a great leap compared with most current models. Thus the marriage of math and biology gives birth to a new research discipline: system biology. It makes biological study more quantitative and solid. However, as discussed in the introduction, the driving force behind the model is the Turing's Reaction-Diffusion equations. The chemical perspectives in these kinds of equations can bring complex pattern forming in the system but based on recent research embryonic pattern forming is largely produced by mechanical force interactions and deformations. Basically, the positive and negative feedbacks which are brought by reaction-diffusion equations can be replaced by the rules defined in genetic regulatory networks. In addition, the Cellular Potts Model has limited capabilities for describing the moving boundaries in a cell aggregate.

A large number of computational models for morphogenesis are similar to the CompuCell project. The Turing's reaction-diffusion equations are the governing equations in those models. They only differ in mesh algorithm choice, computational engine and their target applications. There are a number of other models, that focus on more specific topics such as Odell's model [Munro and Odell, 2002a; Munro and Odell, 2002b] which deals with the emergence of global polarity of convergent extension and Ingber's model [Huang and Ingber 2005] which focuses on the mechanical influence of the extracellular matrix [Discher *et al.*, 2005; du Roure *et al.*, 2005] on cell proliferation and tumour formation (Figure 2.18). Most of these models are implemented in the two dimensional (2D) domain. Three dimensional (3D) models for cell arrangement are still rare, and currently are limited to models from Honda [Honda *et al.* 2003] and Viens [Viens and Brodland, 2007] (Figure 2.19).

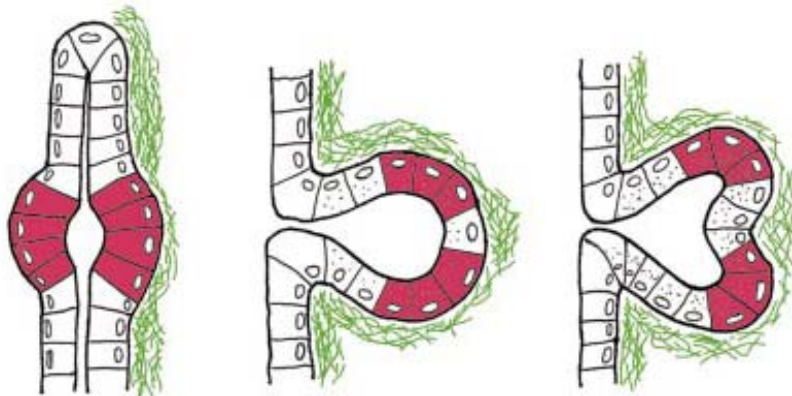


Figure 2.18. Ingber's ECM influence model [Huang and Ingber 2005].



Figure 2.19. Partially dissociated 111-cell finite element mesh [Viens and Brodland, 2007].

### 2.3.2 Tissue scale Models

Tissue scale models, including finite element models, divide the embryo into elements that contain tens to hundreds of cells, and they allow the mechanical consequences of various driving-force hypotheses on tissue and whole-embryo motions to be tested. Some of the most promising of these hypotheses are presented here.

The apical constriction hypothesis assumes that apical microfilament contraction (Figure 2.20a) provides crucial driving forces. The apical constriction hypothesis has been implemented by many researchers [Odell *et al.*, 1981 (Figure 2.21); Oster and Alberch, 1982; Clausi and Brodland, 1993], and has produced tissue motions that are quite realistic. Although these models are based on the same driving force, small differences in constitutive models can produce significant changes in the results. The model of Clausi and Brodland has provided perhaps the most realistic results (Figure 2.22).

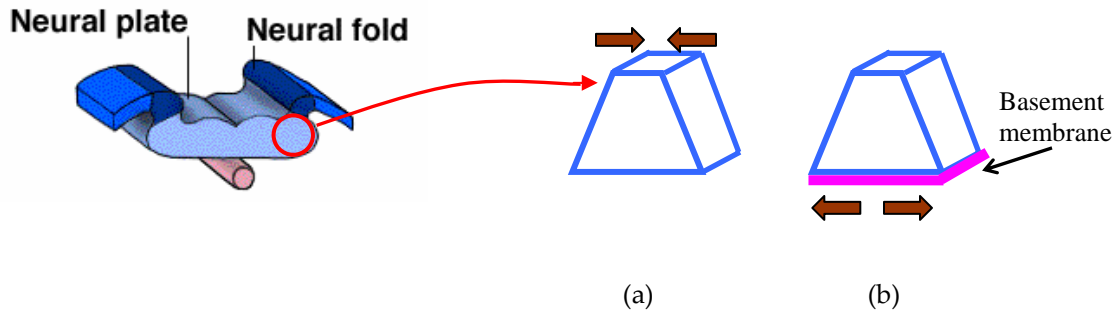


Figure 2.20. Tissue scale models driving force hypotheses. (a) Apical constriction hypothesis. (b) The constrained expansion or contraction hypothesis.

The constrained expansion or contraction hypothesis [Odell *et al.*, 1981] assumes that the cell shape changes are caused by the expansion or contraction of the basement membrane or extracellular matrix, which is just underneath the cell aggregate (Figure 2.20 b). Invagination and evagination can be easily simulated with this hypothesis, but biological evidence to support it is lacking.

The cytoplasm flow hypothesis [Jacobson *et al.*, 1986; Taber, 1995] assumes that the motile behaviour of epithelial cells is similar to that of mesenchymal cells. Cytoplasm flows from the basal surface through the lateral sides of the cell to the apical surface, and then flows back to the basal surface through the median (Figure 2.23). Adhesion molecules join the current and accumulate at the apical surface, which causes the two cells to stick together. According to Jacobson, the model can simulate invagination and folding of the neural tube by setting a different flow rate in each cell. Different flow rates cause shear stresses to exist between two cells which cause out-of-plane deformation.

Shell models proposed by Hardin and Cheng [Hardin and Cheng, 1986], treat the embryonic epithelia as a continuum shell. By applying different forces on different locations and modeling cell rearrangement as fluid-like flow materials, this model has been used to simulate embryonic gastrulation.

The hypothesis of morphogens interacting with geometry [Cummings, 1989] assumes the morphogen density changes cause the geometry of the epithelium to change, and the changing geometry in turn reacts to change the morphogen pattern. This model treats the

epithelial as a continuum and incorporates positive feedback and negative feedback into the model to generate complex geometric results.

The hydromechanical hypothesis is proposed by Borkhvardt [Borkhvardt, 2002]. The process of invagination and evagination is considered to a result of the intracavitary pressure changes in an autonomous regime. The place with the weakest force of resistance will bulges out or sags, which results in invagination and evagination (Figure 2.24).

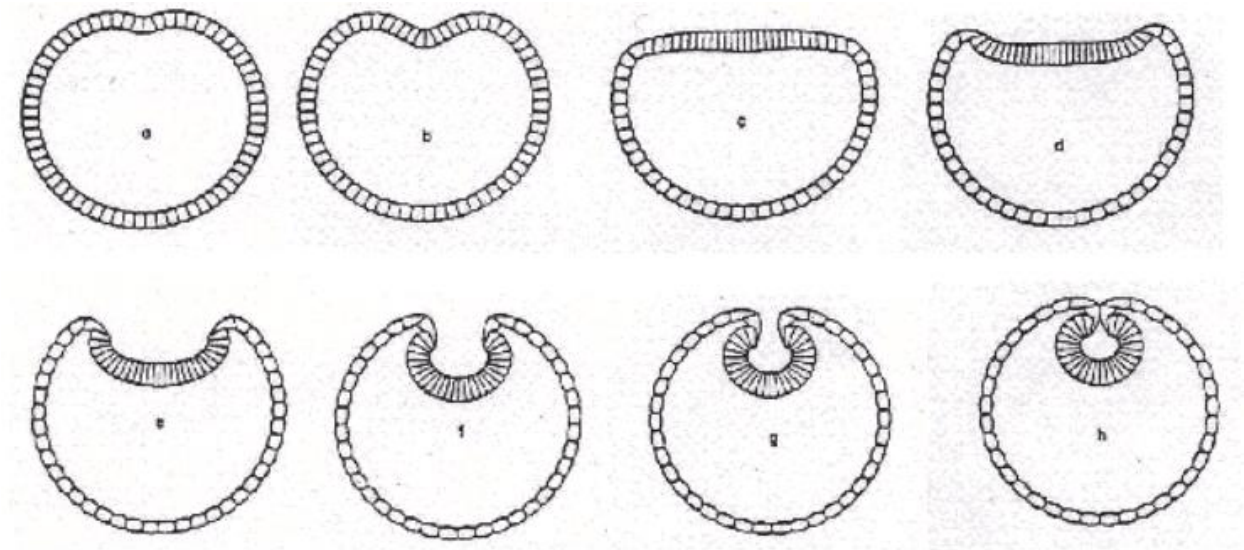


Figure 2.21. Apical constriction model of amphibian neurulation [Odell *et al.*, 1981].

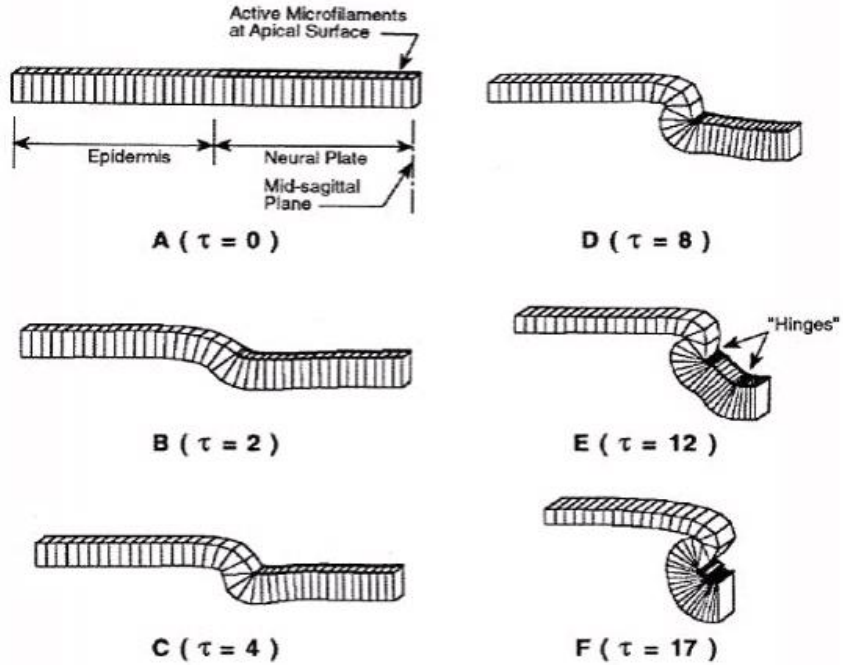


Figure 2.22. Clausi and Brodland finite element model [Clausi and Brodland 1993].

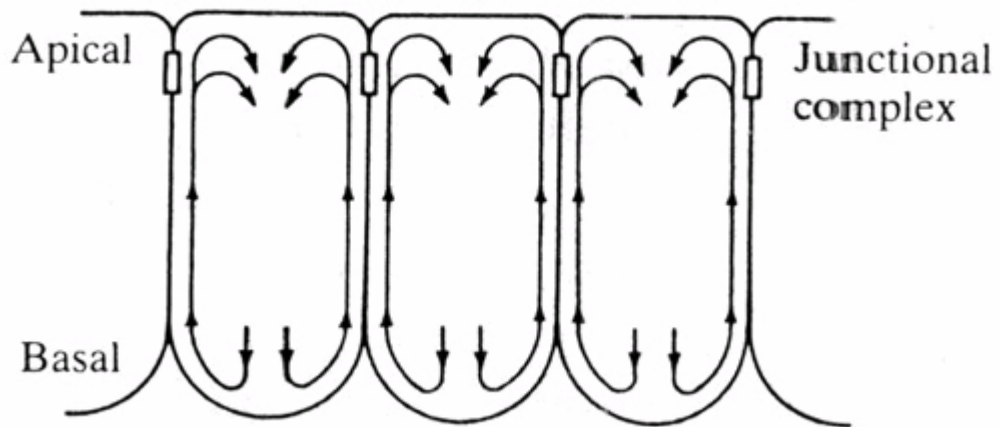


Figure 2.23. Cortical flow of adhesive structures [Jacobson *et al.*, 1986].

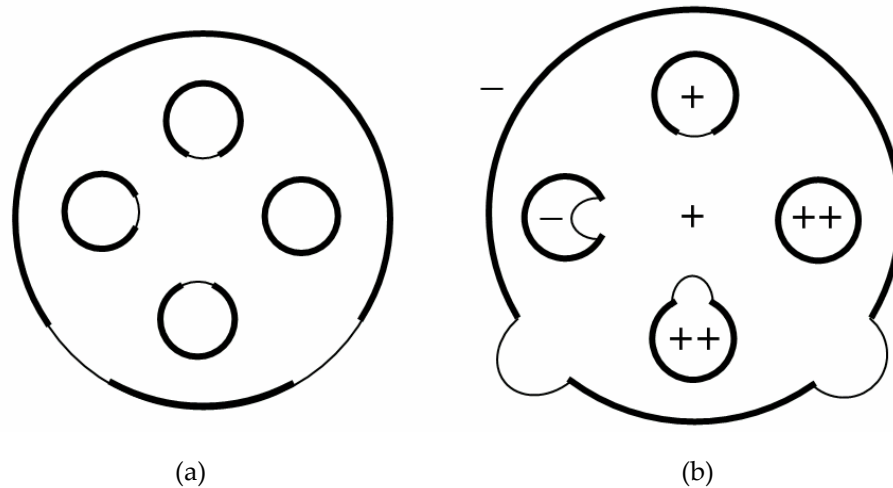


Figure 2.24. A schematic representation of growth and morphogenesis of the entire organism and its parts in terms of the hydromechanical model [Borkhvardt, 2002]. (a) Initial, state at equal local pressures; (b) State arisen after the appearance of difference in pressures. The organism is depicted as a system of closed cavities (designated as circles). The difference in pressure in individual cavities and outer medium is designated as symbols “++” > “+” > “-”. The thickness of lines designating cavity walls corresponds to their resistance.

### 2.3.3 Challenge for cellular scale models:

In spite of the many advances that have been made, a number of significant challenges for both type models still remain. Currently, cellular scale models are usually employed to study global shape changes such as cell rearrangement. However, it would be intellectually satisfying to model each cell with one element to simulate both local and global shape change effects during embryonic morphogenesis. To fulfill this objective some challenges need to be overcome.

1. Most cellular scale models are based on a 2D domain. When they are extended to a 3D domain, more details about cell-cell interactions need to be understood. Because 3D models involve much more complex boundary conditions than 2D models. For example, the junctions between cells may involve five, six or more cells in three dimensions. Both geometric description of these conditions and mechanical effects such as adhesion molecules are necessary.
2. The computational cost increases dramatically if a 3D model is applied. Early stages of embryos may consist of tens or hundreds of thousands of cells. It is impractical to

implement a finite element algorithm to simulate each cell with one element without a great advance in computational power.

3. With positive and negative feedbacks, a small random error in the initial configuration affects the final result greatly. A perfect emergence of embryonic morphogenesis is difficult to simulate before a comprehensive understanding of embryonic morphogenesis is achieved. For example, a correct neurulation may not “emerge” without proper cell thickness. And if the cellular-scale model does not provide sufficient parameters to characterize the cell motions, the “emergence” is also difficult to occur.

#### **2.3.4 Challenge for tissue scale models:**

1. Most current tissue scale models do not allow for cell rearrangements, and this has a huge impact on the entire embryonic development. Cell rearrangement may be a source of positive and negative feedbacks as mentioned in the introduction. It is the key to a successful mechanical model.
2. Tissue scale models focus on changes in tissue properties caused by cellular scale motions. Sufficient and proper parameters must be extracted to describe such changes. A positive and negative feedback mechanism is embedded in the tissue properties change.
3. To input or verify changes in tissue properties with computational simulations, experimental measurements of mechanical properties of embryonic tissue are required. Embryonic tissue properties have been found to vary greatly during the whole process. For instance, the ectoderm tissue in early gastrulation and late gastrulation yield totally different results in measurements [Glagoleva, 2003; Benko and Brodland, 2007].

## 2.4 Multiscale Modeling

Almost every problem in science and engineering is multiscale in nature. Embryos are made of multiple tissues, tissues are composed of cells, cells are made up of molecules, and molecules consist of atoms and electrons. The recent progress in nanomechanics, such as molecular dynamics and quantum mechanics, enables researchers to study the biological problems at the DNA scale. However, models such as finite element models, molecular dynamics, and quantum mechanics alone are sometimes not sufficient to describe the physical phenomena; the coupling between different scale models becomes the alternative solution to this kind of problem. For instance, suppose one has a material patch with crack propagation occurring in a small area; crack propagating involves the breaking of chemical bonds. This requires a quantum mechanics approach. The atoms close to the crack can be modeled by a molecular dynamics approach, and a finite element approach is accurate enough for simulating the rest of the material patch. The result is that it takes three separate theoretical frameworks to model the mechanics of crack propagation in solid structures that are in the order of one micron in size. The key point of this kind of coupling of models with different scales is that these three models have to work or compute at the same time and send feedback to each other, which researchers refer to a parallel coupling. The critical part of parallel coupling is how to define the interplay between different models. One has to make the boundary connection seamless without having energy loss during the computation.

Another type of multiscale coupling is called serial coupling [Winsberg, 2006]. As implied in its name, the coupling of three separate theoretical frameworks is implemented through “parameter passing.” For instance, the results from quantum mechanics can be compressed into the potential function and passed to molecular dynamics. The computational results from the molecular dynamics approach can be incorporated into parameters such as elastic modules or stiffness and passed to the finite element approach. This type of coupling requires the constitute equations be expressed with limited parameters, and the extracting of these parameters is not time consuming. The advantage of this method

is the reduction of computational cost. By using the molecular dynamics approach, one may spend one month on a computational simulation of a piece of skin tissue. With finite element model, however, the time cost can be reduced to one day.

Since the problem we focus on is the embryonic morphogenesis which does not involve much size effect and current computational capacity is limited, the serial multiscale coupling method becomes a better choice.

## **2.5 The what, why and how of our model**

From the reviews and discussions above it is not difficult for us to draw a conclusion that there is a strong demand for combining biochemical pathways with mechanical models. The question for biologists is not only how does gene control makes embryonic morphogenesis happen, but also when and where does embryonic morphogenesis happen [Huang and Ingber, 2005]. In contrast, the question for researchers in the mechanical field is how can biochemical pathways incorporate into a finite element framework.

Another crucial question arises: at which scale should we model an embryo, at the cellular scale or tissue scale? From a biological perspective, embryos consist of tissues; tissue consists of cells. Correspondingly from a mechanical perspective, the whole-embryo mechanics can be decomposed into tissue mechanics and tissue mechanics can be decomposed into cell mechanics. Many models based on both levels have been proposed to study embryonic morphogenesis. However, none of them has successfully simulated the whole process. For a cellular model to make this happen, we are expecting a huge CPU time cost. Sometimes even a small perturbation will ruin this process. In view of these facts, the tissue scale model becomes a good candidate for the simulation, as long as we give correct biomechanical feedbacks in the tissue scale and the tissue model captures the mechanical motions of cells. This drives us to try the possibility combining tissue mechanics and cell mechanics together. Setting up a bridge between the cellular scale model and the tissue

model to capture the interrelationship between cell motions and tissue fabric evolution might be the correct answer.

This report presents the inception of a whole-embryo finite element model of neurulation. To capture the mechanical interactions that occur across cellular, tissue and whole-embryo scales, an advanced, multiscale finite element approach is used. Cell-based simulations are used to construct a system of constitutive equations for embryonic tissues, and experimental data are used to determine the parameters in these equations. Images of live embryos and serial sections of fixed embryos provide the geometric data needed to complete the whole-embryo model. Biological experiments will also be conducted to verify the validity of this model. Finally, investigations will be performed using on our model to determine the mechanical cause of spina bifida.

# Chapter 3

## Constitutive Model

To address the challenges associated with cellular scale and tissue scale models, our lab has developed an open framework for the computational simulation of embryonic morphogenesis. By bridging the gap between cellular scale and tissue scale models, this framework intends to probe the relationships between mechanical events (or their genetic precursors) and embryonic malformations. The structure of this framework is summarized as follows:

1. **Constitutive model:** A cell-based constitutive model for embryonic epithelia is devised to capture the interrelationship between cell motions and tissue fabric evolution.
2. **Computational model implementation:**
  - 1) Collect data on embryo shape, tissue fabric, epithelial thickness and tissue mechanical properties.
  - 2) Use a custom spatial-temporal data correlation system (feature grid) to correlate the experimental spatial-temporal data with the finite element model.
  - 3) Use our computational engine to predict the outcomes of various starting configurations and active force generation systems.
  - 4) Use advanced pre- and post-processing software to set up and view the finite element model.
3. **Computational simulations:** Simulations will be evaluated against experimental data.

As mentioned in the previous chapter, during embryonic morphogenesis, various structured monolayers of cells called epithelia undergo both local and global shape changes, which includes rolling of plates into tubes, stretching, bending of tubes, shearing in the tissue scale, reshaping, rearranging, and mitosis in the cellular scale. The complex motion of cells makes combining these motions into one computational model in the cellular scale difficult. On the other hand, a unified constitutive model is visibly lacking for tissue scale models.

To set up a robust constitutive model, a thorough understanding of the relationship between stress and strain during embryonic morphogenesis is required. Analytical studies and computer simulations have shown [Chen and Brodland, 2000; Brodland *et al.*, 2000; Brodland *et al.*, 2007] that the stress and strain relationship are greatly affected by the cellular scale motions such as reshaping, rearranging, and mitosis. This kind of observation also receives support from experiment results [Brodland and Wiebe, 2004]. To incorporate these cellular scale motions into a tissue scale model, parameters representing these cellular scale motions should be extracted from cellular scale computational simulations and experiments.

Obtaining experimental data of mechanical properties of embryo epithelia have been difficult because of their fragility and the tiny size of the specimens. However, some properties which cannot be measured in experiments can be obtained in computational models. Therefore cellular scale computational simulations become an important approach to study tissue fabric evolution. Although a number of computation models have been proposed to study the problem, their common drawback is that they do not adequately model the cell viscosity, which is critical for cell motions. By introducing cell viscosity into their model, Chen and Brodland have successfully simulated a number of important cell motions.

### **3.1 Finite Element Simulation of Cellular Scale Models**

Basic components behind the cellular scale model are shown in Figure 3.1 [Chen and Brodland, 2002] and are listed below.

**Microfilaments** – bands of contractile material along the perimeter of the apical end of each cell and composed predominantly of actin.

**Microtubules** – long, thin tube-like structures, which are composed of sub-units of the protein tubulin. They act as a scaffold to determine cell shape.

**Intermediate filaments** – provide a three dimensional tension network to support the cell scaffold.

**Extra-cellular matrix (ECM)** – is a complex structural entity surrounding and supporting cells.

**Basement membrane** – is a structure that supports an overlying epithelium and keeps the epithelial cells organized as a layer.

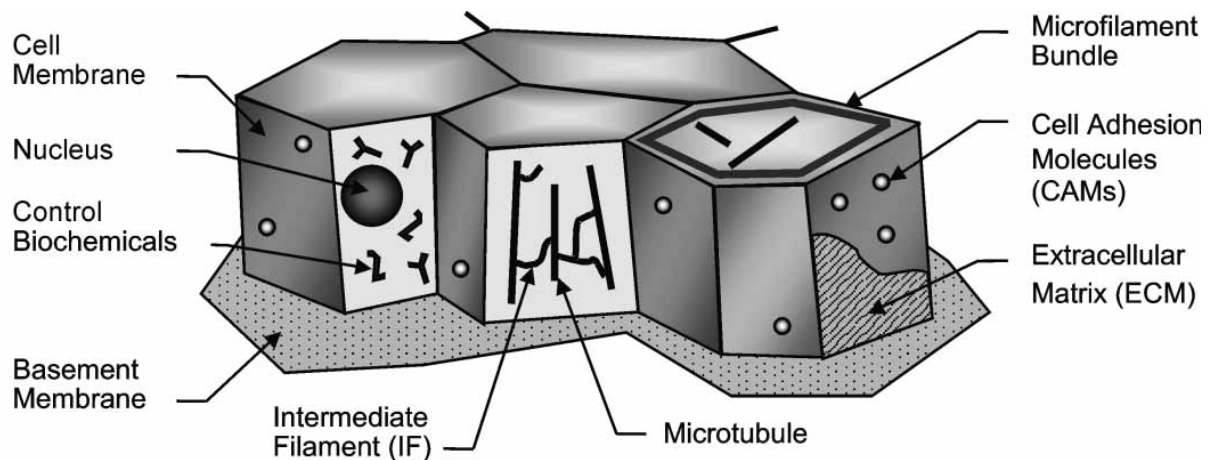
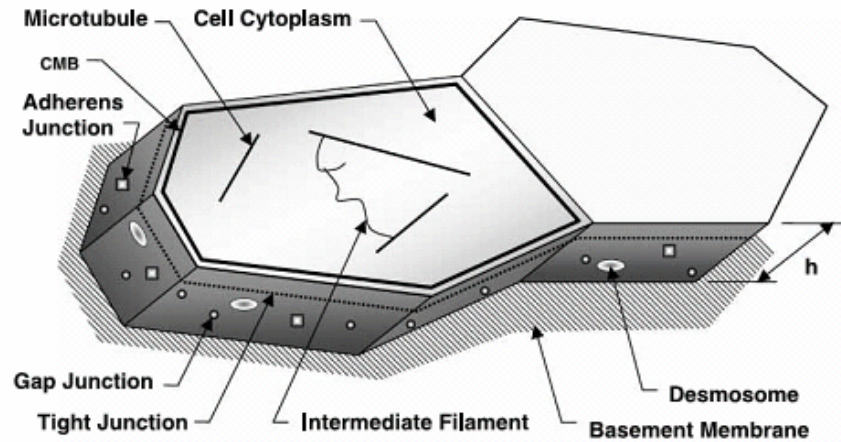


Figure 3.1. A schematic representation of a piece of epithelium [Chen and Brodland, 2000]. Components of mechanical importance are shown.

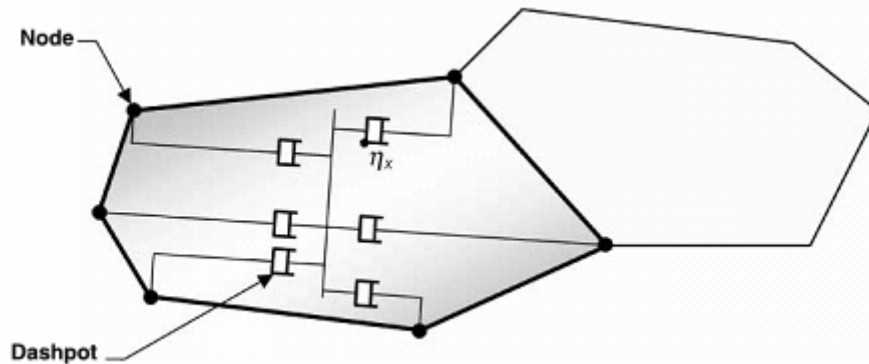
In Brodland’s model, some key assumptions can be summarized as follow:

1. The net driving force in cell-cell interactions is approximated by an interfacial tension along cell boundaries. The tension is generated by circumferential microfilament bundles (CMBs), other microfilaments and cell membrane tension. Forces generated by cell adhesion molecules (CAMs) reduce this contraction.

2. The cell cytoplasm, including its embedded networks of intermediate filaments, is considered to be incompressible and is modeled by an effective viscosity  $\mu$ .



(a)



(b)

Figure 3.2. The cell and finite element models [Brodland *et al.*, 2007]. (a) A schematic representation of two cells that are assumed to form part of a generic embryonic epithelium. (b) A model based on systems of orthogonal dashpots. In the interest of image clarity, only the dashpots aligned with the long axis of the cell are shown. The second set of dashpots would run orthogonal to those shown. Truss elements, like those shown in (a), are assumed to act along each cell-cell interface.

Based on the above assumptions, there are a total of two free material parameters in this model: a constant tension  $\gamma$  along each cell-cell interface and the cell viscosity  $\mu$ . To model these cells in the finite element method, nodes of each cell are connected with each other by

an orthogonal dashpot system which is along with the principal axes of the cell (Figure 3.2b). Each dashpot in Figure 3.2b is assigned the same damping coefficient  $\eta_x$ . As a consequence, the movement of one node will produce the same reaction force on the other nodes (assuming they are fixed when the movement occurs). This brings simplicity to the stiffness matrix assembling. And through virtual work principle,  $\eta_x$  can be related to the cell viscosity  $\mu$  based on some geometric assumptions [Brodland *et al.*, 2007]. Truss-like elements are employed to model the interfacial tension along the each side of the cell. To keep the total cell volume constant, a volume boundary constraint is imposed on each cell. The system is described by the equation:

$$\mathbf{C}\dot{\mathbf{u}} + \mathbf{K}\mathbf{u} = \mathbf{f}, \quad (3.1)$$

where  $\mathbf{C}$  is the damping matrix of the system,  $\mathbf{K}$  is the stiffness matrix of the system,  $\mathbf{f}$  is the consultant force vector applied on the system,  $\mathbf{u}$  is the nodal displacements, and  $\dot{\mathbf{u}}$  is its derivative over time.

Because the tension  $\gamma$  is constant, the truss-like elements have no contribution to the global stiffness of the whole system. Therefore the global stiffness  $\mathbf{K}$  is zero. By using a forward difference scheme, this nonlinear equation can be rewritten as follow:

$$\begin{aligned} \mathbf{C}\dot{\mathbf{u}} &\approx \mathbf{C} \frac{\Delta \mathbf{u}}{\Delta t} = \frac{1}{\Delta t} \mathbf{C} \Delta \mathbf{u} = \mathbf{f}, \\ \frac{1}{\Delta t} \mathbf{C}(\mathbf{u}_{q+1} - \mathbf{u}_q) &= \mathbf{f}_q, \end{aligned} \quad (3.2)$$

The volume constraints are incorporated as Lagrange multipliers.

The mechanism by which cells are able to rearrange is shown in Figure 3.3. As the boundary between cells A and C becomes shorter and shorter it disappears with a quadruple junction forming. After that, a new boundary is generated between B and D. Because time steps are discrete in the finite element simulation the topology is assumed to change directly from Figure 3.3a to Figure 3.3c, when the edge length is less than a specified value (the critical length). The new-formed edge between B and D is longer than this

specified short value to avoid the simulation going back and forth between Figure 3.3a and Figure 3.3c.

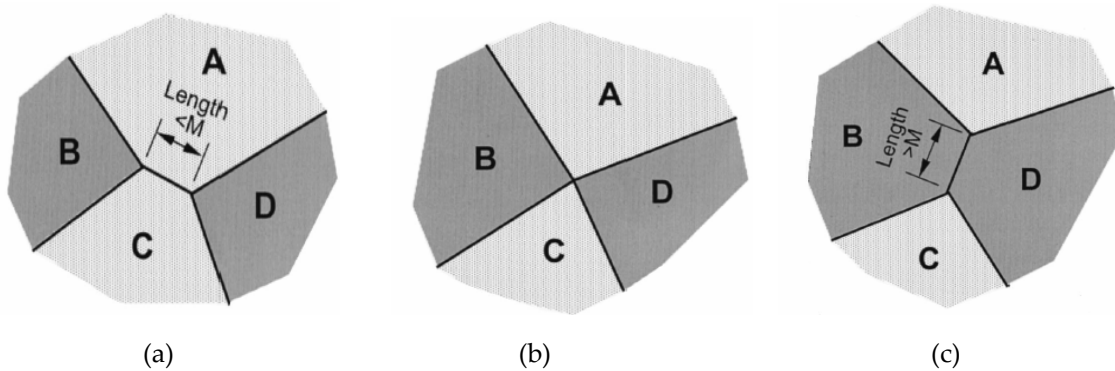


Figure 3.3. Coding assumptions about cell rearrangement [Chen and Brodland, 2000]. (a) A and C are moving away from each other. The boundary length becomes shorter and shorter until it is less than a certain length  $M$ . (b) The real situation happening in a real embryo, but in coding rules, this situation will not happen. If the boundary length is less than  $M$  the program will skip situation (b) and jump to (c). (c) A and C are separated and the new boundary between B and D is formed. Its length is greater than  $1.1M$  to avoid dead looping.

By conducting a great number of simulations including stretching, compression, simple shear, and the combination of these effects, the authors found that the instant stress value depends primarily on the tension along the boundaries of the cells and the orientation of these boundaries. In the mean time, corresponding experiments [Brodland and Wiebe, 2004] were conducted to support these hypotheses. In addition, the simulation concerned with the cell annealing and tissue strain relaxation yielded some valuable observations, revealing that epithelial aggregates share some fundamental characteristics of plastic deformation with other materials. When the epithelial tissue undergoes stretching, cell edges rotate to align with the stretch direction. If the stretch force is less than a certain value, the deformation will be caused only by cell elongation. When the stretch force is greater than this value, the cells will choose rearrangements instead of elongation. This property resembles the yielding of a plastic material. Based on the computational simulations, the yield point is related to the ratio of the interfacial tension  $\gamma$  to the product of the cell viscosity  $\mu$  and the strain rate  $\dot{\epsilon}$ .

Clearly, based on the computational simulations and experiment observations listed above, we can conclude that the evolution of the tissue fabric will affect the stress condition dramatically. Corresponding parameters, which can lend themselves to physical interpretation, need to be extracted from the cellular scale simulations to describe the fabric evolution. Tensors have been a good choice for describing tissue fabric in a number of applications [Rothenburg, 1981; Asipauskas *et al.*, 2003; Lätzel *et al.*, 2000; Hohler and Cohen, 2005; Janiaud and Graner, 2005]. For historical reasons, three parameters, cell shape, orientation and cell edge density, are employed to describe embryonic tissue fabric evolution for the constitutive equations instead [Brodland, 2004].

### 3.2 Governing Parameters

Consider a patch of cells, as shown schematically in Figure 3.4. The definition of the density  $\beta$  of the cells in a specific region of a planar aggregate is:

$$\beta = \frac{n}{A}, \quad (3.3)$$

where  $n$  is the number of cells in the region and  $A$  is its area.

For each cell  $i$  in the planar aggregate, a shape factor  $\kappa$  is defined as:

$$\kappa_i = \sqrt{\frac{I_{\max}^i}{I_{\min}^i}}, \quad (3.4)$$

where  $I_{\min}^i$  is the minimum principal moments of inertia and  $I_{\max}^i$  is the maximum principal moments of inertia. The average cell shape factor,  $\bar{\kappa}$  is defined as

$$\bar{\kappa} = \frac{1}{n} \sum_{i=1}^n \kappa_i, \quad (3.5)$$

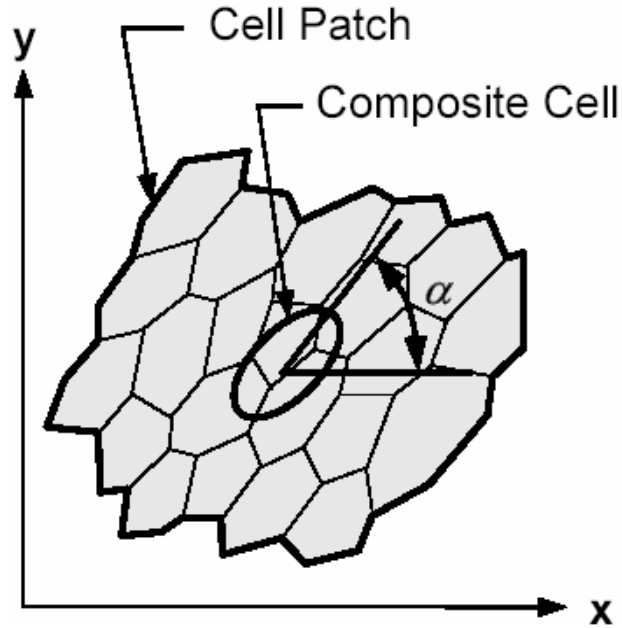


Figure 3.4. Composite cell [Brodland, 2004].

The cells that contact the boundary of the aggregate are neglected because they have truncated geometries. To describe the integral shape of the aggregate, a composite cell (Figure 3.4) can be used to describe the whole patch with its moments of inertia

$$\begin{aligned}
 I_{xx}^* &= \frac{1}{n} \sum_{i=1}^n I_{xx}^i, \\
 I_{yy}^* &= \frac{1}{n} \sum_{i=1}^n I_{yy}^i, \\
 I_{xy}^* &= \frac{1}{n} \sum_{i=1}^n I_{xy}^i,
 \end{aligned} \tag{3.6}$$

defined as the average of the centroidal moments and product of the individual cells in the aggregate. The shape factor of the composite cell is defined as:

$$\kappa = \sqrt{\frac{I_{\max}^*}{I_{\min}^*}} \tag{3.7}$$

where  $I_{\min}^*$  is the minimum principal moments of inertia and  $I_{\max}^*$  is the maximum principal moments of inertia based on the  $I_{xx}^*$ ,  $I_{yy}^*$  and  $I_{xy}^*$ .

As shown in Figure 3.4, the major axis of the composite cell  $\alpha$  is defined as:

$$\alpha = \arctan\left(\frac{2I_{xy}^*}{I_{xx}^* - I_{yy}^*}\right) \quad (3.8)$$

In case  $I_{xx}^* = I_{yy}^*$ , the angle can be defined uniquely using the equation

$$\alpha = \begin{cases} \frac{\pi}{4}, & I_{xy}^* > 0 \\ 0, & I_{xy}^* = 0 \\ -\frac{\pi}{4}, & I_{xy}^* < 0 \end{cases} \quad (3.9)$$

Although these parameters are used to describe a planar aggregate, an extension to three-dimensional aggregates is not difficult.

A dimensionless time  $\tau$  is used here to replace the real time variable.

$$\tau = St, \quad (3.10)$$

$$S = \frac{\gamma\rho}{2\mu\delta} \quad (3.11)$$

$$\rho = \frac{g\sqrt{\beta}}{\pi} \int_0^\pi \sqrt{\kappa \sin^2 \theta + \frac{1}{\kappa} \cos^2 \theta} d\theta \quad (3.12)$$

where  $\delta$  is the thickness of the planar aggregate,  $\rho$  is the interface density which is defined as the sum of the length of all internal cell boundaries plus half of the perimeter of the patch over the area of the patch,  $g$  is a form factor having a typical range between 1.9 and 2.2 for isotropic aggregates [Brodland and Wiebe, 2004].

So far three parameters,  $\kappa, \alpha$  and  $\beta$  are defined as a robust set of parameters to describe the fabric of an epithelium. The next step is to relate these parameters to different cellular scale effects in tissue fabric evolution.

### 3.3 Bulk Deformation

A deformation tensor  $F$  [Malvern, 1969] is employed to map a pair of non co-linear vectors  $A$  and  $B$  to corresponding vectors  $a$  and  $b$  in the new configuration assuming that the deformation is uniform over the whole sheet (Figure 3.5).

$$F = \begin{bmatrix} F_{11} & F_{12} \\ F_{21} & F_{22} \end{bmatrix} = \begin{bmatrix} a_1 & b_1 \\ a_2 & b_2 \end{bmatrix} \begin{bmatrix} A_1 & B_1 \\ A_2 & B_2 \end{bmatrix}^{-1} \quad (3.13)$$

To map the initial configuration with  $\kappa=1$ ,  $\alpha=0$  and  $\beta=1$  in Figure 3.5a to configuration  $\kappa$ ,  $\alpha$  and  $\beta$  in Figure 3.5b. A tensor  $\mathbf{G}$  can be used to perform the transformation.

$$G = \begin{bmatrix} \cos(\alpha) & -\sin(\alpha) \\ \sin(\alpha) & \cos(\alpha) \end{bmatrix} \begin{bmatrix} \sqrt{\frac{\kappa}{\beta}} & 0 \\ 0 & \sqrt{\frac{1}{\kappa\beta}} \end{bmatrix}, \quad (3.14)$$

The transformation can be considered as a stretching in the coordinate directions to produce the required  $\kappa$  and  $\beta$  followed by a counter clockwise rotation  $\alpha$ .

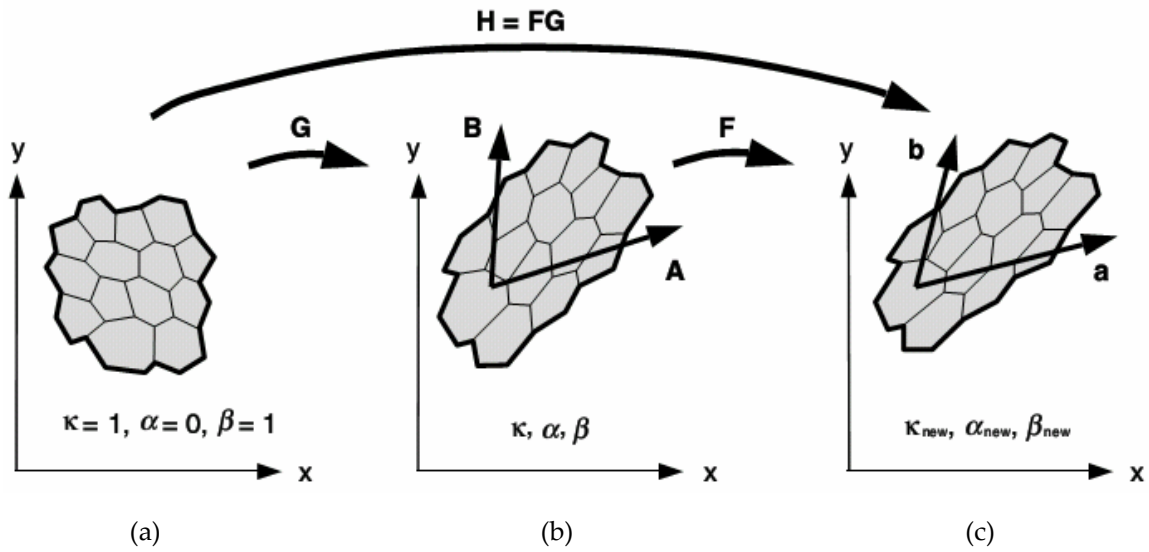


Figure 3.5. Deformation of the cell patch [Brodland, 2004]. (a) A hypothetical isotropic configuration with a unit cell density  $\beta$ . (b) New configuration deformed from (a) by  $\mathbf{G}$ . (c) New configuration deformed from (a) by  $\mathbf{H}$  or deformed from (b) by  $\mathbf{F}$ .

To transform from configuration a to c (Figure 3.5c), the tensor  $\mathbf{H}$  is calculated by the product:

$$\mathbf{H} = \mathbf{FG} \quad (3.15)$$

Considering how an arbitrary unit vector would deform under  $\mathbf{H}$  (Figure 3.6),

$$v(\eta) = \begin{Bmatrix} \cos \eta \\ \sin \eta \end{Bmatrix}$$

The unit circle will transform to an ellipse, and the angle between the major axis of the ellipse and the x-axis is given by:

$$\eta_{\max} = \frac{1}{2} \arctan\left(2(H_{11} * H_{12} + H_{21} * H_{22}), H_{11}^2 - H_{12}^2 + H_{21}^2 - H_{22}^2\right) \quad (3.16)$$

new  $\alpha_D$  can be given by:

$$\alpha_D = \arctan\left(H_{21} \cos \eta_{\max} + H_{22} \sin \eta_{\max}, H_{11} \cos \eta_{\max} + H_{12} \sin \eta_{\max}\right) \quad (3.17)$$

The subscript D means the effect is caused by in-plane deformation

$$\kappa_D = \sqrt{\frac{\|Hv(\eta_{\max})\|}{\|Hv(\eta_{\max} + \pi/2)\|}} \quad (3.18)$$

$$\beta_D = \frac{\beta}{\|H\|} \quad (3.19)$$

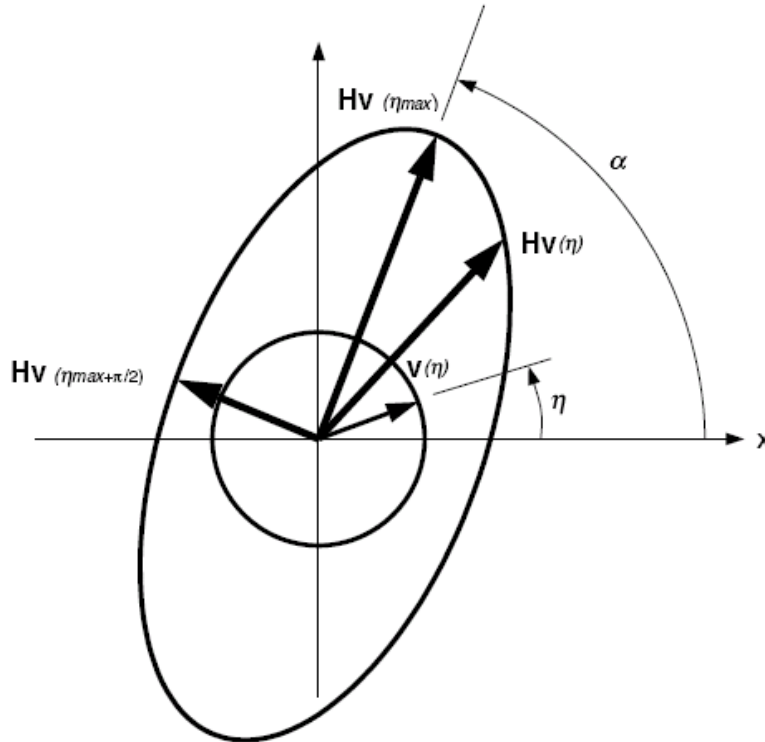


Figure 3.6. Mapping of an arbitrary vector  $v(\eta)$  into  $Hv(\eta)$  [Brodland, 2004].

### 3.4 Cell Annealing

Cell annealing is the spontaneous rounding of elongated cells. Based on the 3D computational simulation and theoretical analysis [Brodland and Veldhuis, 2003], the annealing causes  $\kappa(t)$  to decay in an approximately exponential fashion, which can be represented as

$$\kappa(t) = 1 + (\kappa_0 - 1)e^{-\zeta S t} \quad (3.20)$$

where  $\kappa_0$  is the starting value of  $\kappa$ , and  $\zeta$  is the time constant of the decay with the value 0.17. On account of implementation in the finite element method, this relationship is formulated in incremental form:

$$\Delta\kappa_R = \zeta S (1 - \kappa) \Delta t \quad (3.21)$$

The subscript R represents that the effect is caused by cell annealing.

### 3.5 Mitosis

Mitosis also has an impact on the tissue fabric evolution [Brodland, 2004; Hemerly *et al.*, 2000; Nechiporuk, 2006]. Usually mitosis orientation is governed by its long axis. The  $\kappa$  of two daughter cells will be closer to 1 (isotropic) than that of their mother cell. The relationship can be represented as

$$\begin{aligned} \Delta\kappa_M &= \psi \Omega \frac{(\kappa_{dividing} - 1)}{\kappa_{dividing}} \Delta t, & \kappa < 2 \\ \Delta\kappa_M &= \psi \Omega \frac{(\kappa_{dividing} - \frac{\kappa_{dividing}}{2})}{2} \Delta t, & \kappa \geq 2 \end{aligned} \quad (3.22)$$

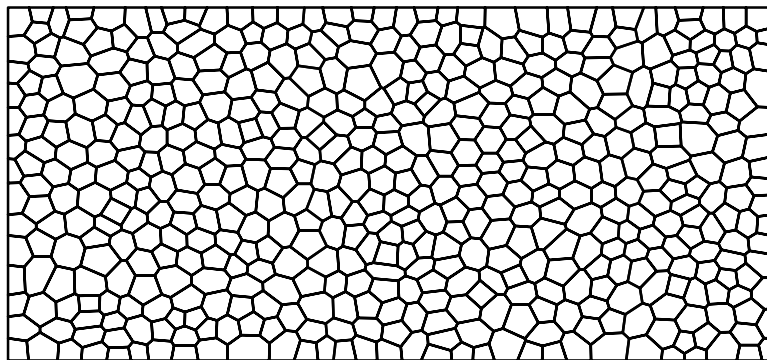
where  $\kappa_{dividing}$  is the shape parameter of the mother cell,  $\Omega$  is the fraction of the current number of cells that divide per unit time.  $\psi$  is the dimensionless rate factor, which is taken here to be -2.65. The subscript M is used to denote a mitosis effect. The finite difference formula for mitosis effect on cell density is written as

$$\Delta\beta_M = \beta \Omega \Delta t \quad (3.23)$$

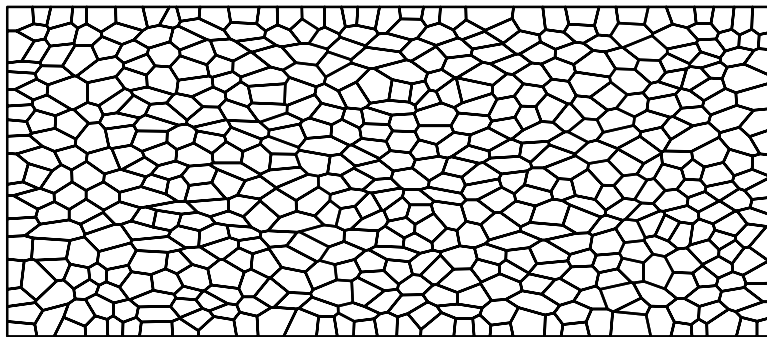
### 3.6 Lamellipodia effect

When suitable biochemical conditions are present [Wallingford and Harland, 2002; Ehrlich, 2002], embryonic cells generate oriented protrusions, called lamellipodia. As these protrusions arise from a cell, they push their way between an immediately adjacent pair of cells until they contact the next neighboring cell [Gloushankova *et al.*, 1997; Gloushankova *et al.*, 1998]. When they then contract, they draw the source and next neighboring cells together [Bailly and Condeelis, 2002]. This action can produce reshaping of tissues and their constituent cells.

Figure 3.7a shows a typical starting configuration. The cells have an initial average aspect ratio of  $\kappa=1.2$ , and their long axis is parallel to the horizontal axis of the Figure. As the interfacial tensions, lamellipodia and cell viscosities interact over time, the cells reshape, even though the edges of the tissue are restrained (Figure 3.7b).



(a)  $\tau = 0$



(b)  $\tau = 20$

Figure 3.7. Temporal evolution of cellular fabric with Lamellipodia effect.

The work reported here is focused on investigating the stress-strain characteristics of a rectangular patch of model tissue in terms of the rate  $r$  at which lamellipodia form, the relative strength  $q$  of their contractions and the boundary conditions. To simplify the real scenario, we assume the fraction of the current number of cells that produce a lamellipodium per unit dimensionless time is constant and denoted by  $r$ . When a lamellipodium forms, the linear element along the edge where it arises is replaced by a lamellipodium element that generates a total tension of  $q \cdot \gamma$ .

Simulations show that if  $r$ , the rate of lamellipodium generation, is sufficiently small, the cells basically anneal [Brodland *et al.*, 2006] as shown by the average cell aspect ratio decay (Figure 3.8). However, as the rate of lamellipodium generation is increased, the cells elongate more because the tendency towards cell elongation produced by lamellipodia pulling on their ends is greater than the tendency towards rounding produced by annealing effect.

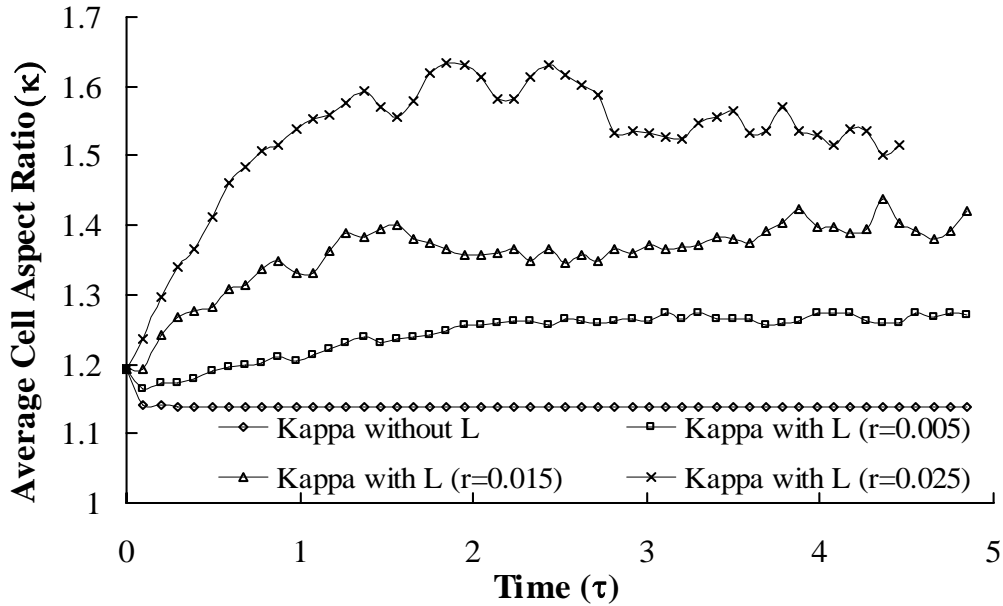


Figure 3.8. Cell aspect ratio versus dimensionless time.

The dimensionless tensile stress

$$S = \frac{2\sigma}{\gamma\rho} \quad (3.24)$$

produced in the tissue is shown in Figure 3.9. Parametric studies show that this stress changes with time primarily because lamellipodia cause the cells to elongate in the direction of lamellipodium action and that this change in cell shape significantly affects the interfacial tension-generated stresses [Brodland *et al.*, 2006]. The stresses generated directly by the lamellipodia effect, the difference between the two curves, are rather modest. The simulations show that while lamellipodia do directly affect the stresses acting in an epithelium, their primary mode of action is to reshape the cells, thereby changing the interfacial tension-generated stresses. Because the constitutive equations derived previously are able to predict changes in cellular fabric, modifications to predict the mechanical effects of lamellipodium action should be possible.

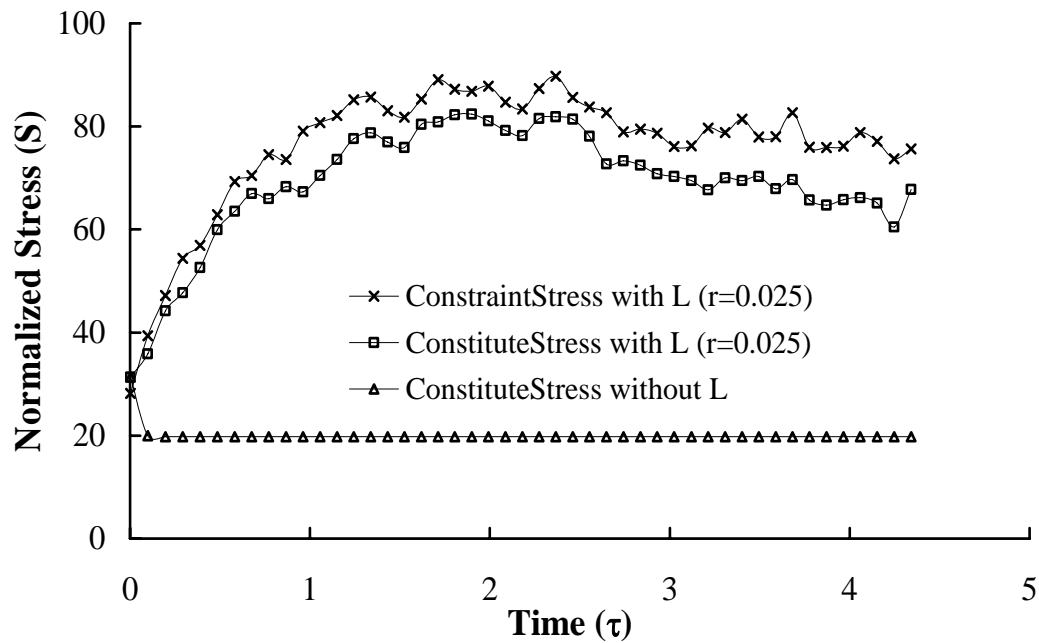
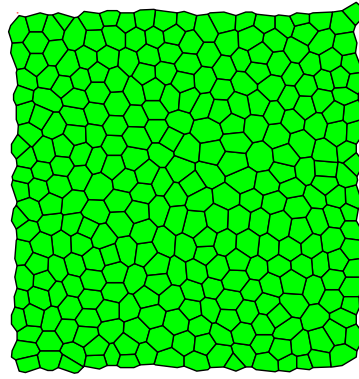
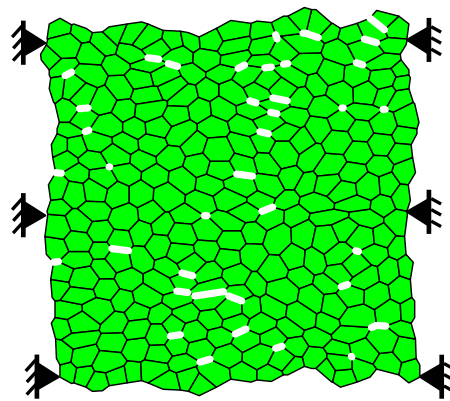


Figure 3.9. Normalized stress versus time.

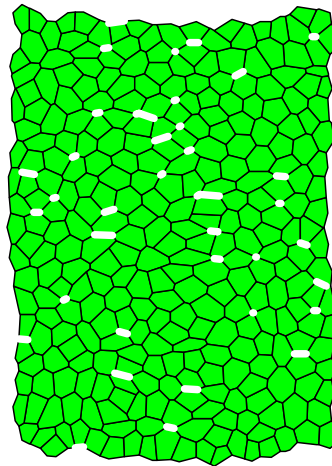
To derive the expression of lamellipodia effect on tissue fabric evolution, periodic boundary conditions are employed in this report instead of the rectangular boundary conditions used in recent studies [Brodland and Veldhuis, 2006]. Two cases including restrained lateral edges (Figure 3.10b) and unrestrained lateral edges (Figure 3.10c) are compared here.



(a) Initial configuration



(b) Restrained lateral edges



(c) Unrestrained lateral edges

Figure 3.10. Simulations of a patch of cells with  $q=2$ ,  $S=0.2$  and  $r=0.13$ . (a) The initial configuration consists of 301 cells. (b) When the edges of the patch are fixed, the cells elongate and ultimately reach an aspect ratio of  $\kappa=1.24$ . (c) When the edges of the patch are unrestrained, lamellipodia (shown with wide white lines) cause the patch to narrow to 80% of its original width.

**Restrained lateral edges:**

In this case, the geometry of the whole patch can not deform, and the lamellipodia effect acts along with the annealing effect and reach a balance point of a certain value of  $\kappa$ . At this critical point,  $\kappa$  remains constant, therefore we have the following equation:

$$\frac{d\kappa_L}{d\tau} + \frac{d\kappa_A}{d\tau} = 0, \quad (3.25)$$

Since we've already had the expression for  $\frac{d\kappa_A}{d\tau}$ , the tissue fabric change caused by annealing, we can easily get the expression for  $\frac{d\kappa_L}{d\tau}$ , the tissue fabric change caused by

lamellipodia effect. There is an alternative way to compute the value for  $\frac{d\kappa_L}{d\tau}$  from time

series. Plot the change rate of  $\kappa$ ,  $\frac{d\kappa}{d\tau}$ , with respect to dimensionless time  $\tau$  and extract

the maximum value around time zero. This value  $\left. \frac{d\kappa}{d\tau} \right|_{\tau=0}$  is  $\frac{d\kappa_L}{d\tau}$  because  $\kappa$  is 1 and

$\frac{d\kappa_A}{d\tau}$  is zero at that time. Figure 3.11 is the track of  $\kappa$  over time  $\tau$ . Each curve represents a

case with different relative strength  $q$ .

**Unrestrained lateral edges:**

In this case, the patch of cell can move freely and the simulation results demonstrate that  $\kappa$  of the patch of cells has a small fluctuation around 1 assuming that the initial configuration is isotropic. Therefore the annealing effect is negligible here. The lamellipodia effect will be balanced by the bulk deformation shown in Figure 3.10 to keep  $\kappa$  approximate to 1. The equation can be expressed as

$$\frac{d\kappa_L}{d\tau} + \frac{d\kappa_D}{d\tau} = 0, \quad (3.26)$$

By calculating the  $\frac{d\kappa_D}{d\tau}$  based on the geometric shape change, we are able to plot the track of

$\frac{d\kappa_L}{d\tau}$  with respect to  $\tau$ . To express  $\frac{d\kappa_L}{d\tau}$  with  $r, q$ , we have following simulation results.

Recent studies show that the  $\frac{d\kappa_L}{d\tau}$  holds a linear relationship with  $r$  [Brodland and Veldhuis, 2006] and Figure 3.12 indicates that the relationship between  $\frac{d\kappa_L}{d\tau}$  and  $q$  is also linear except the degree of kinematic restraint in the medio-lateral direction will linearly modify the curve's slope. The two curves in Figure 3.12 represent the two limiting cases, unrestrained lateral edges and restrained lateral edges. By doing linear interpolation we are able to obtain the  $\frac{d\kappa_L}{d\tau}$  based on the degree of kinematic restraint.

$$\frac{d\kappa_L}{d\tau} = \chi \cdot r \cdot (q - 1.5) \cdot e, \quad (3.27)$$

where  $\chi$  is the coefficient calculated from the simulation curve fitting,  $e$  is the restraint index which describe the degree of kinematic restraint in the ML direction. Its incremental form is written as

$$\Delta\kappa = \chi \cdot r \cdot (q - 1.5) \cdot e \cdot \Delta t. \quad (3.28)$$

By using constraint index  $e$  we are able to interpolate between the cases, unrestrained lateral edges and restrained lateral edges.

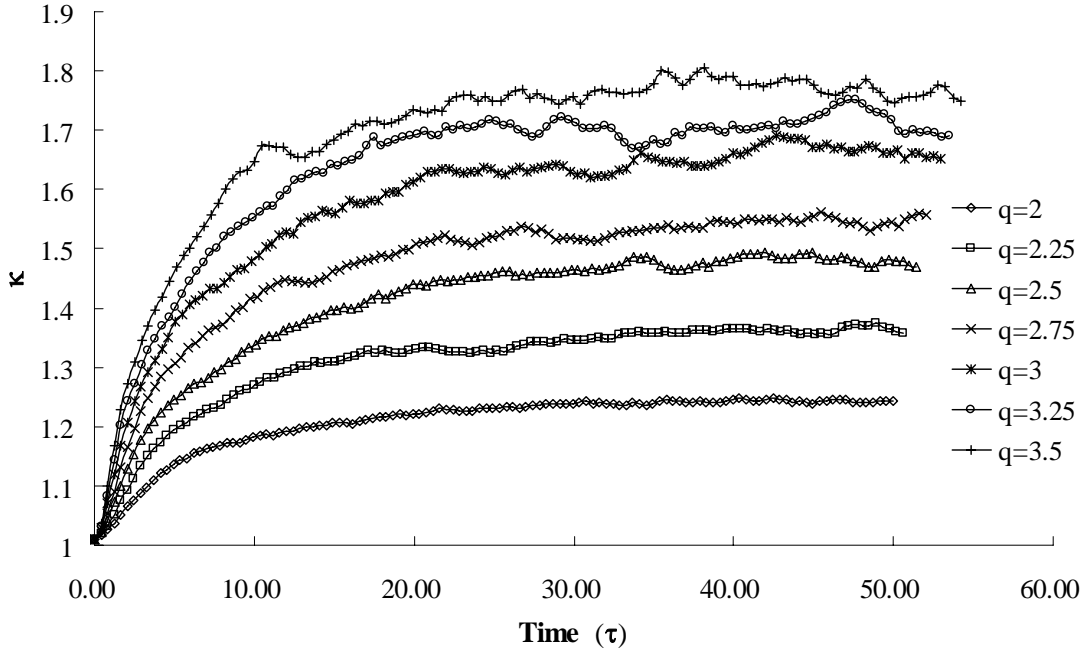


Figure 3.11.  $\kappa$  versus dimensionless time  $\tau$  with different relative strength  $q$ .

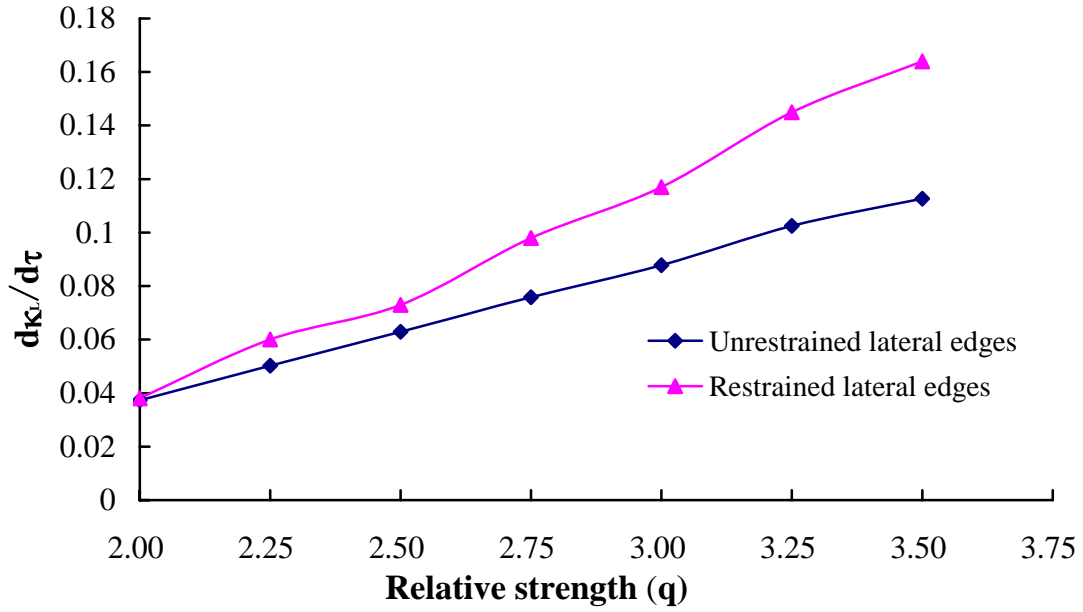


Figure 3.12.  $\frac{d\kappa_L}{d\tau}$  versus relative strength  $q$  with different boundary conditions.

### 3.7 Collective Effect on Tissue Fabric Evolution

Combining the deformation, annealing, mitosis and lamellipodia effect together, the three parameters in the new configuration can be represented as follows:

$$\begin{aligned}
 \kappa_{new} &= \kappa_D + \Delta\kappa_R + \Delta\kappa_M + \Delta\kappa_L \\
 \alpha_{new} &= \alpha_D \\
 \beta_{new} &= \beta_D + \Delta\beta_M
 \end{aligned}
 \tag{3.29}$$

To relate these parameters to the stresses in planar aggregate, the author [Brodland, 2004] defined the stress in epithelial cell aggregates as the net force per unit length of cutting plane (Figure 3.13) [Brodland, 2004]. The previous studies [Brodland and Wiebe, 2004; Brodland and Veldhuis, 2003; Brodland and Veldhuis, 2002; Chen and Brodland, 2000] show that the interface density is,

$$\rho = \frac{g\sqrt{\beta}}{\pi} \int_0^{\pi} \sqrt{\kappa \sin^2 \theta + \frac{1}{\kappa} \cos^2 \theta} d\theta \quad (3.30)$$

where  $g$  is a form factor that ranges from 1.9 to 2.2 for isotropic aggregates.

The stress in the directions of the long and short axes of the composite cell can be expressed as follows [Brodland and Wiebe, 2004] (Figure 3.13):

$$\sigma_1 = \frac{\rho\gamma\kappa}{2\pi} \int_0^{2\pi} \frac{\cos^2 \theta}{\sqrt{\kappa \cos^2 \theta + \frac{\sin^2 \theta}{\kappa}}} d\theta \quad (3.31)$$

$$\sigma_2 = \frac{\rho\gamma}{2\pi\kappa} \int_0^{2\pi} \frac{\cos^2 \theta}{\sqrt{\kappa \sin^2 \theta + \frac{\cos^2 \theta}{\kappa}}} d\theta \quad (3.32)$$

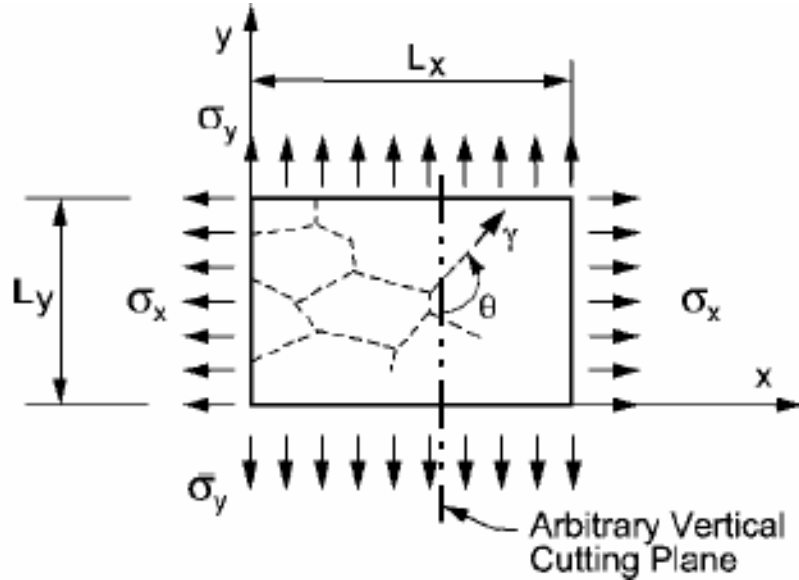


Figure 3.13. Planar view of a monolayer cell aggregate [Brodland, 2004]. The stress  $\sigma_x$  and  $\sigma_y$  (principal stress of the sheet of the aggregate) produced by interfacial tensions  $\gamma$  can be determined by considering the force crossing suitable cross-sections of the aggregate.

Formulas for transforming the two-principle stress into global coordinate system are:

$$\sigma_x^\gamma = \frac{\sigma_1 + \sigma_2}{2} + \frac{\sigma_1 - \sigma_2}{2} \cos 2\alpha, \quad (3.33)$$

$$\sigma_y^\gamma = \frac{\sigma_1 + \sigma_2}{2} - \frac{\sigma_1 - \sigma_2}{2} \cos 2\alpha, \quad (3.34)$$

$$\tau_{xy}^\gamma = \frac{\sigma_1 - \sigma_2}{2} \sin 2\alpha \quad (3.35)$$

Then the vector of driving forces is given by

$$\mathbf{f} = \mathbf{f}_{\text{int}} + \mathbf{f}_{\text{ext}} \quad (3.36)$$

where  $\mathbf{f}_{\text{ext}}$  is the vector of external driving force.  $\mathbf{f}_{\text{int}}$  is the vector of internal driving force which is caused by the stresses  $\sigma_x^\gamma, \sigma_y^\gamma, \tau_{xy}^\gamma$ . The equation in incremental form can be rewritten as

$$\mathbf{C}\dot{\mathbf{u}} \approx \mathbf{C} \frac{\Delta \mathbf{u}}{\Delta t} = \frac{1}{\Delta t} \mathbf{C} \Delta \mathbf{u} = \mathbf{f} = \mathbf{f}_{\text{ext}} + \mathbf{f}_{\text{int}} = \mathbf{f}_{\text{ext}} + \sum_{i=1}^r \mathbf{f}_{\text{int}}^i \quad (3.37)$$

By using a forward difference scheme, the nonlinear equation can be solved.

The computation diagram is expressed in Figure 3.14.

### 3.8 Model validation

The constitutive model presented here has combined bulk deformations, annealing, mitosis, and the lamellipodia effect together to study tissue fabric evolution. The question is whether the combination of these effects in the constitutive equation is consistent with experimental data and cellular scale model simulation. Because of the limit in experimental measurements, there are few experimental data available for model validation. Thus in this part, a set of cellular scale model computational simulations are conducted to verify the correction. Due to the fact that mitosis and the lamellipodia effect will not happen at the same time in the neural plate area, the simulation done here is focused on the combinational effect of two groups: 1) bulk deformations, annealing and mitosis. 2) Bulk deformation, annealing and the lamellipodia effect. The discussions in the above section have presented the simulation results of the combination of cell annealing and the lamellipodia effect as well as the combination of bulk deformation and the lamellipodia effect. The constitutive equation is derived from and therefore consistent with those simulations. Figure 3.15a shows the agreement between cellular scale finite element simulations and constitutive equations. Figure 3.15b shows that when deformation acts alone (labeled D in Figure 3.15b), cellular

scale simulations and the constitutive equation are in excellent agreement; when deformations and annealing are combined together (D+R), the cellular scale simulation has a larger  $\kappa$  than the constitutive equation. This is because the critical length has large impact on the simulation results. If the critical length is too small, the cell rearrangement is difficult to occur. When the critical length is chosen to be a large value, the cell rearrangements occur too often, and they will balance in a non-realistic state. To make the simulation result consistent with the theory result, a proper critical length is needed. However, it is difficult and impossible to find a value suitable for every situation. Based on computational results, we find that the optimal critical value should be 15% of the average length of the cell aggregate. When the three effects act together (D+R+M), cellular scale simulations and the constitutive equation match again because the mitosis effect increases the possibility of cell rearrangements in each time iteration, and makes the simulation result consistent with theory.

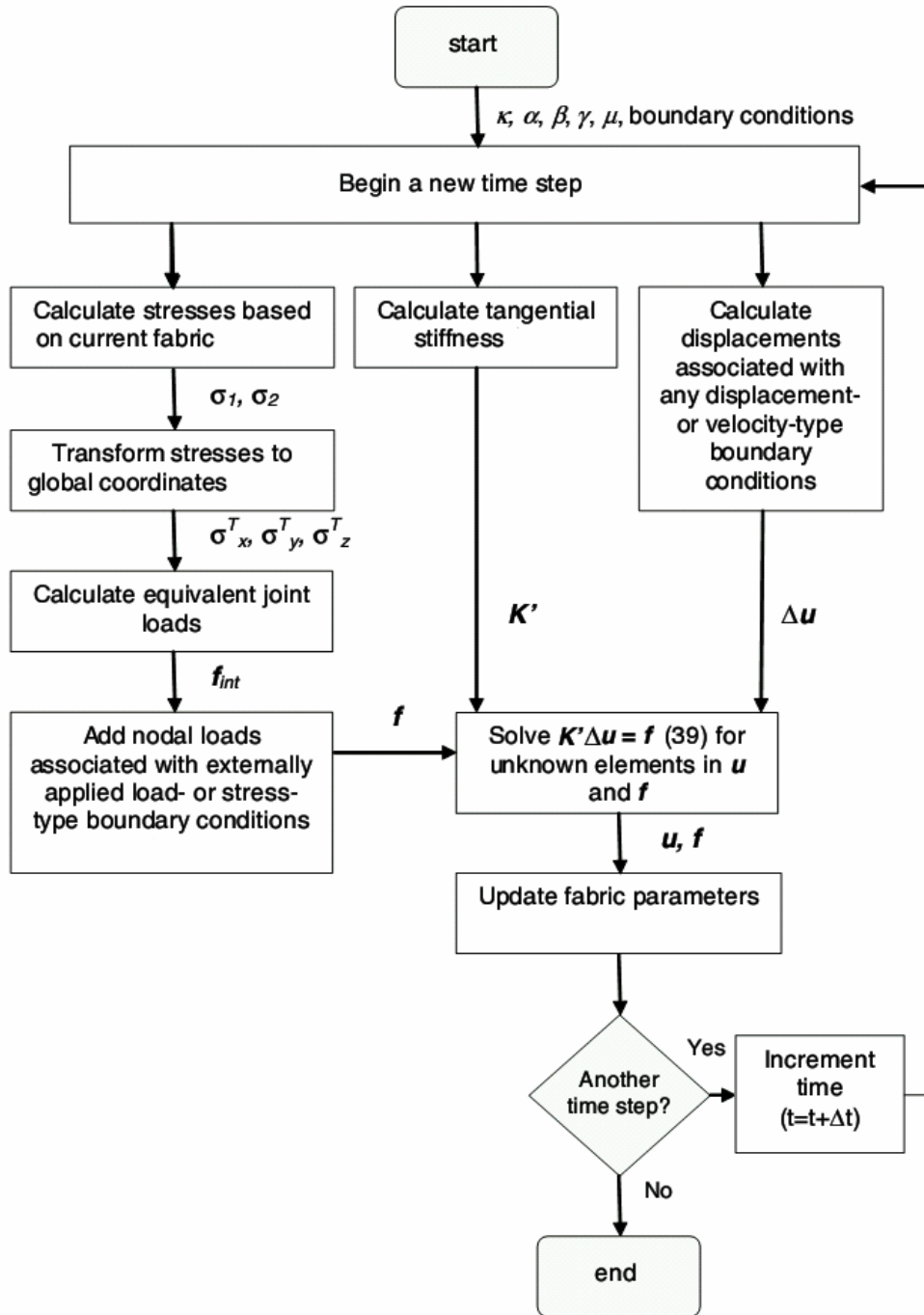
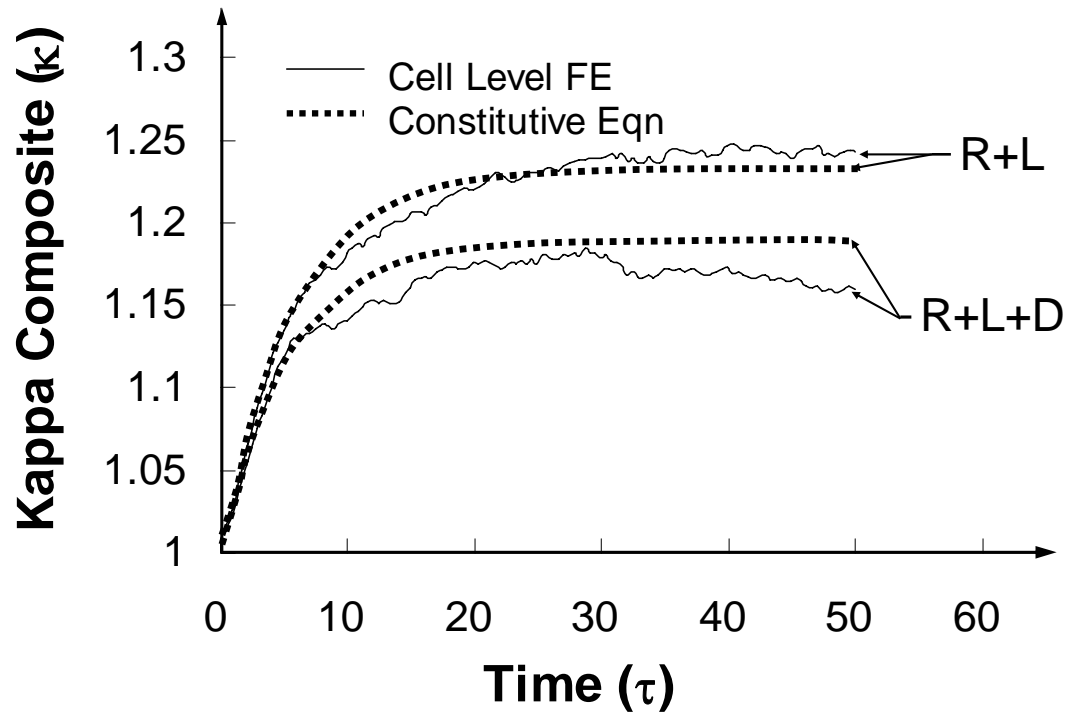
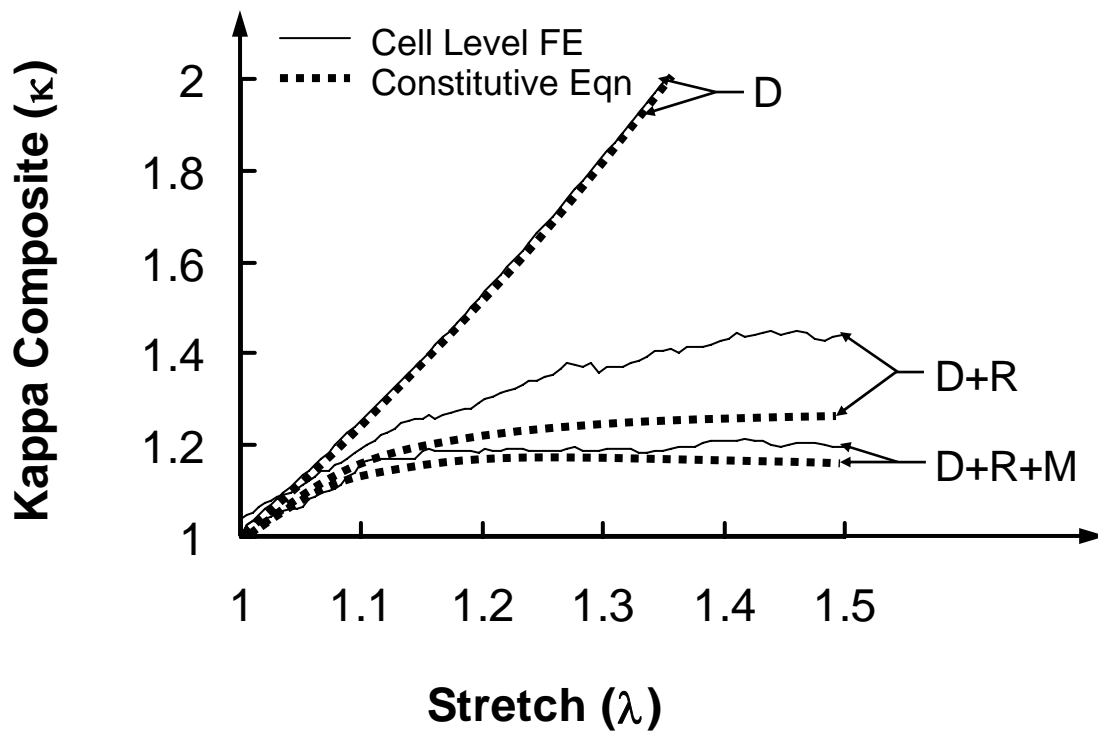


Figure 3.14. Finite element analysis procedure diagram [Brodland, 2004].



(a) Changes to cell shape caused by annealing and lamellipodia effect (R+L) and annealing, lamellipodia effect, and deformation (R+L+D).



(b) Changes to cell shape caused by deformation (D), deformation and annealing (D+R) and deformation, mitosis, and annealing (D+R+M) [Brodland, 2004].

Figure 3.15. Model validation

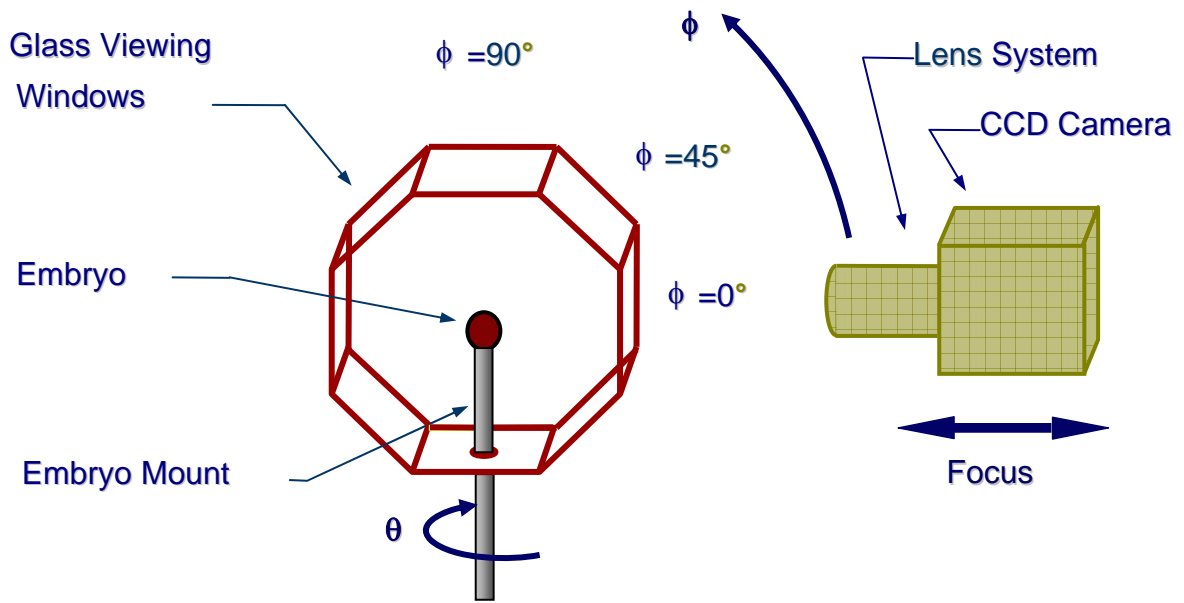
# Chapter 4

## Geometric Data

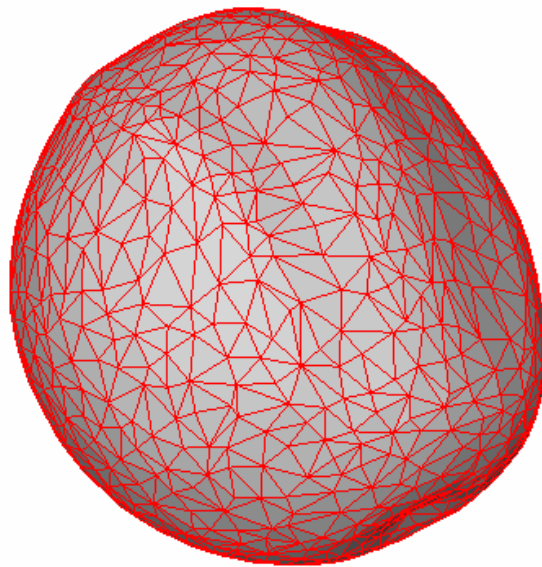
The geometry of an embryo is complex and varies with time. A complete geometric description, therefore, requires both thickness and shape data for each tissue layer and the fabric and material properties of each tissue, and development of these characteristics through time. The four primary steps involved in the collection of this “spatial-temporal data” are 1. determining embryo shape, 2. defining tissue fabric parameters, 3. determining embryo layer thickness, and 4. measuring material properties.

### 4.1 Determining embryo shape

To identify the specific three-dimensional (3D) shape of a live embryo is technically challenging, and our lab has developed an optical method for extracting 3D geometric information of live embryo using robotic microscope images taken at several viewing angles (Figure 4.1a). By establishing point correspondences among these views and employing suitable reconstruction algorithms [Brodland and Veldhuis 1998, Bootsma, 2005], we can calculate the spatial positions of a collection of surface points. These points can then be meshed and used to obtain a surface representation of the embryo (Figure 4.1b). In-plane tissue motions and strain rates are determined using image processing methods that track the motion of groups of cells [Brodland and Veldhuis 1998; Bootsma, 2005].



(a) Schematic diagram



(b) A 3D reconstruction

Figure 4.1. The robotic microscope and a reconstruction made using it.

## 4.2 Defining tissue fabric parameters

Tissue fabric varies greatly with the position on the embryo's epithelium and the time-lapse. Figure 4.2 demonstrates the images captured by Frogatron from different locations on the embryo. Tissue fabric parameters are extracted from the embryo's images using specially designed image processing software. The customized software [Puddister, 2003; Iles *et al.*, 2007] uses horizontal and vertical Sobel operators to highlight the boundaries of the cells and then uses Fourier analysis to transfer the image into the frequency domain (Figure 4.3). After removing the noises of the images in the frequency domain, we are able to determine the tissue fabric parameters  $\kappa, \alpha$ , and  $\beta$ . An interpolation scheme is then used to map fabric parameters onto the surface mesh.

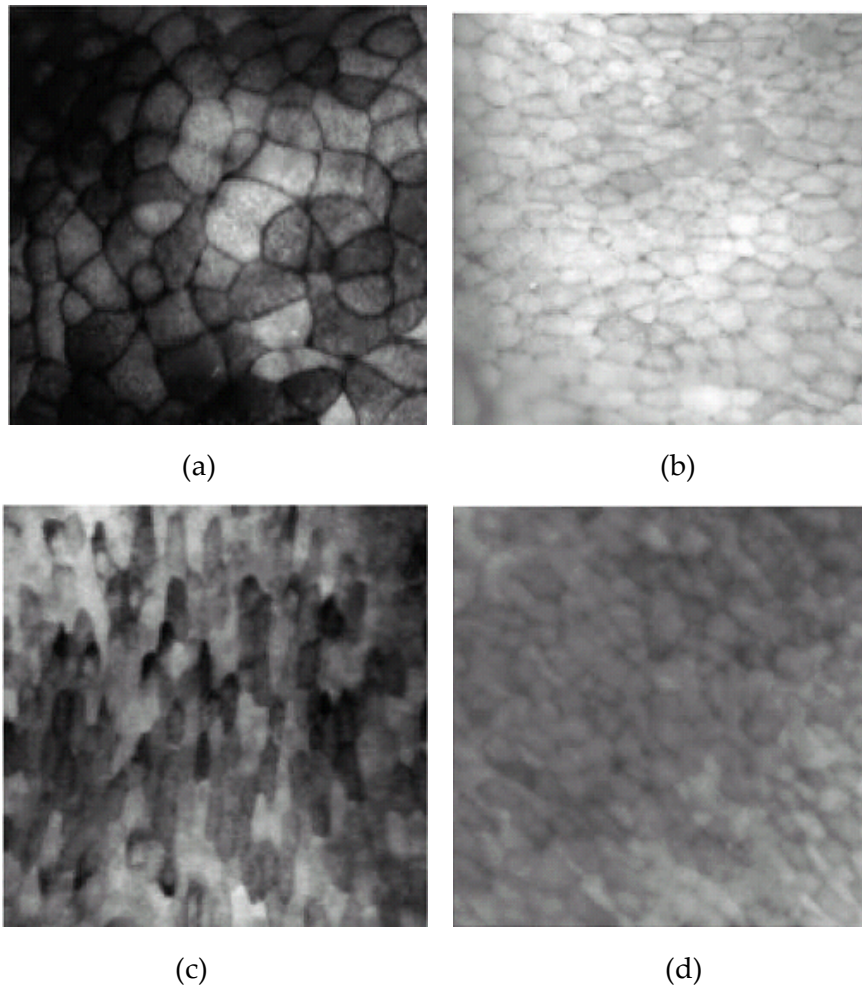
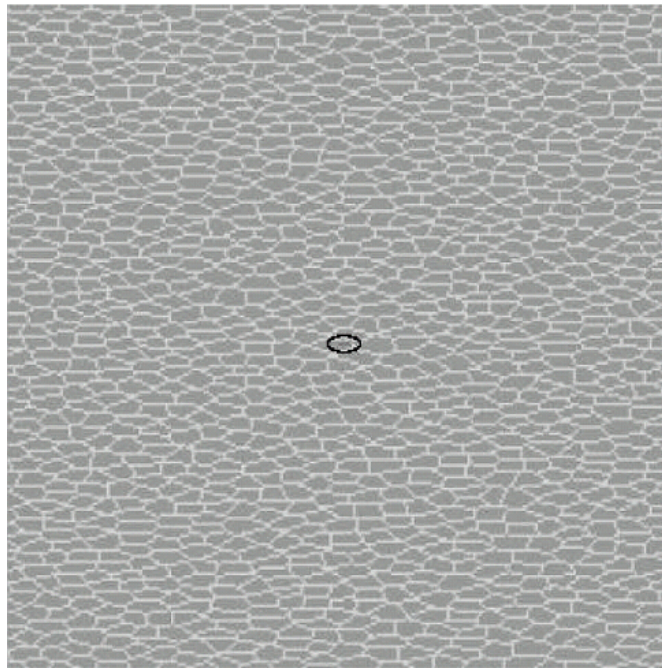
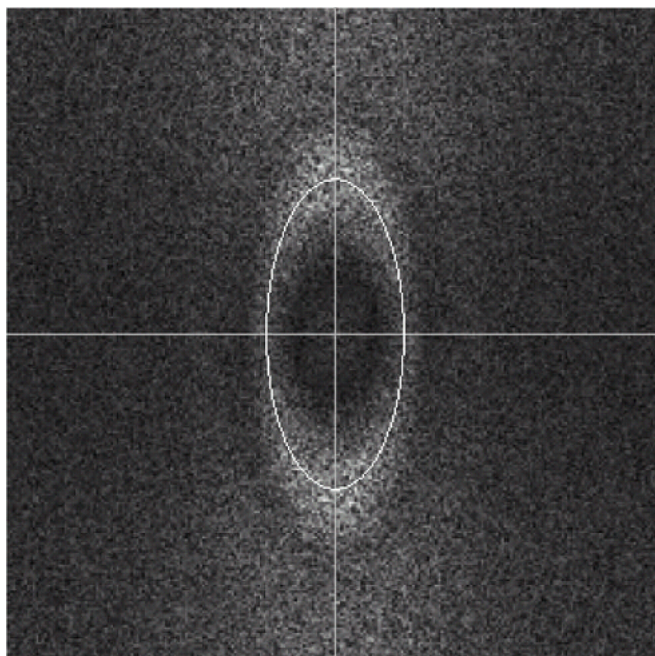


Figure 4.2. Representative images of embryonic epithelia [Iles and Brodland, 2007].



(a)



(b)

Figure 4.3. An image of a cellular tissue and its corresponding magnitude response image [Iles and Brodland, 2007].

### 4.3 Determining the thickness of embryonic epithelium

At the beginning of neurulation, the embryo consists of three layers – the ectoderm, the mesoderm, and the endoderm. The thicknesses of each of these layers can be obtained from serial sections (Figure 4.4). For each serial section, the outline of different layers can be highlighted by customized software or manually. Then by doing registration, we can put all these serial sections together and merge with the surface reconstruction data. The drawback of this approach is the embryo must be fixed to obtain the serial section, and therefore no time lapse is available. The micro Magnetic Resonance Imaging (MRI) could be an ideal solution for extracting sufficient data without fixing embryos, but the technique has not provided the geometric data required for the present project. In practice, layer data should be obtained from several embryos and averaged to improve data quality.

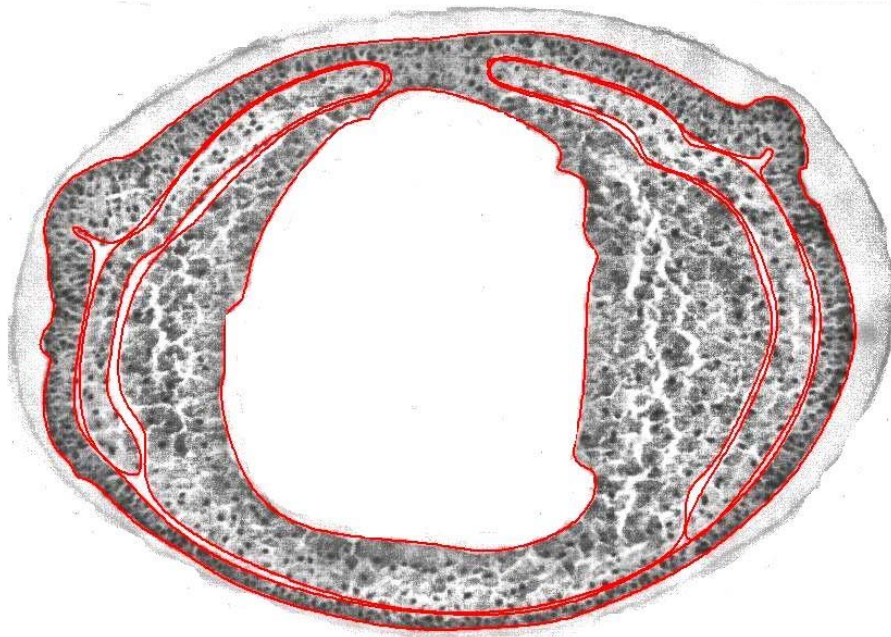


Figure 4.4. A transverse serial section.

## 4.4 Measuring material properties

The tissues in an embryo are extremely fragile and, as a result, measurement of material properties is difficult. To obtain stress-strain data, a small specimen (300 by 500  $\mu\text{m}$ ) of tissue is attached to very thin wires. The specimen is stretched by drawing the wires apart under computer control (Figure 4.5). Applied force is calculated from measurements of wire bending, and real-time feedback is used to prevent the strain reduction that would otherwise arise from the wire deflections. Companion, cellular scale finite simulations are used to back calculate the  $\gamma$  and  $\mu$  values [Wiebe and Brodland, 2005]. Specimens are excised from different locations on the embryo, including three representative specimens from the neural plate (Figure 4.6a) and four from the non-neural epidermis area (Figure 4.6b). The stretching directions include in the medio-lateral direction and the cephalic-caudal direction.

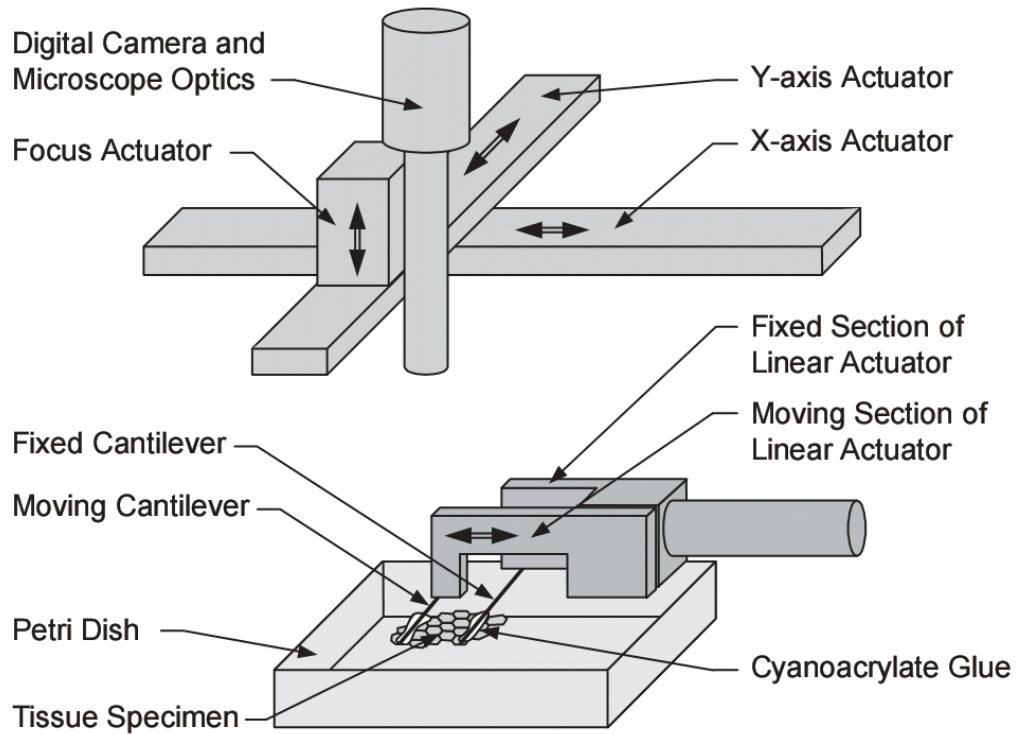


Figure 4.5. Schematic diagram of the tissue tester [Wiebe, 2005]. Cantilever wires are attached to the embryo using cyanoacrylate glue after which the specimen is excised from the balance of the embryo. The base of one of the wires is moved laterally under computer control to produce strain in the specimen, and wire deflection is used to measure the force in the specimen. An overhead camera system is used to obtain high-magnification images that are tiled together to provide high resolution images of the specimen and of the wires. Real-time feedback based on the images is used to correct for strain diminution that would otherwise occur due to wire flexure. Figure is not to scale.

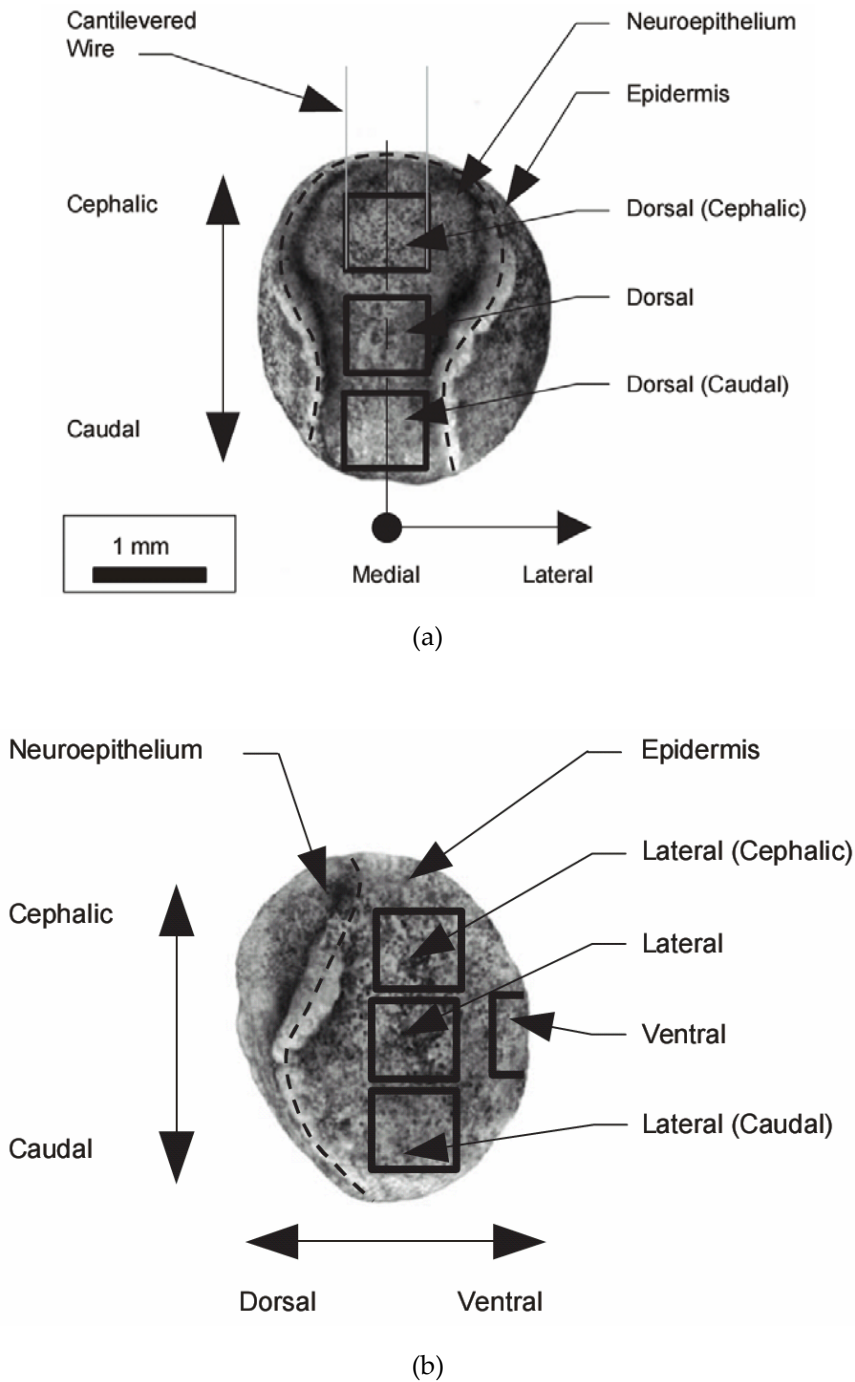


Figure 4.6. Embryo coordinate system and specimen locations [Wiebe, 2005]. (a) A dorsal view of a Stage 15 embryo showing the three dorsal locations from which specimens were excised. The position in which wires would be glued to the specimen is shown for a Dorsal (Cephalic) specimen that is to be stretched in the medio-lateral direction. The visual texture on the embryo's surface is due to pigment variations between cells. The dashed line indicates the approximate demarcation between the neuroepithelium, which will ultimately form the spinal cord and brain, and the epidermis, which will form the skin. (b) A lateral view showing four specimen locations, including one on the ventral surface, where the specimen wraps across to the opposing lateral side.

# Chapter 5

## Feature Grid

Geometric data – including geometric shape, fabric parameters and layer thickness – and material properties are primary data for our current simulations. In future research, more data such as surface curvature, magnetic field, and morphogen field could be incorporated to extend the content of the computational model. These data are measured in a 3D environment over time span; thus the term “spatial-temporal data” will be used to represent these data in this report.

For a 3D embryonic finite element model, the spatial-temporal data binding with each node or element will be calculated by averaging the experimental data from different real embryos. Usually spatial-temporal data measured in experiments are stored with local parametric coordinates instead of Cartesian coordinates because of the difference in measurement environment and approaches. The problem is how to correlate each node or element in the finite element model with the node or element that we have measured in the experiment? An appropriate framework is required to combine these data in local parametric coordinate systems into global Cartesian coordinates. The framework should have the capability of mapping local parametric coordinates into Cartesian coordinates and mapping between different local parametric coordinates. In our finite element (FE) model an embryonic surface coordinate system (feature grid) will be employed to correlate the experimental spatial-temporal data with the finite element model.

## 5.1 Parametric Coordinate Systems

To date there has not been a standardized coordinate system for describing the surface of embryos due to their diversity and complexity. However, when it is applied in practice, there is no need to describe the entire embryonic surface with one unified parametric coordinate system because each area on the embryo surface with similar material properties can have its own parametric coordinate system. During embryonic development, cells in different areas have totally different mechanical or biological properties. In the finite element model we surely do not want to model a patch of cells with different mechanical properties into one element since that will bring about difficulties to finite element analysis. To avoid that, a region based parametric coordinated system is adopted in our model.

Biologists usually divide embryos into three main regions: the neural plate region, the neural fold region and the non-neural epidermis region and we adopt the same scheme in our FE model (Figure 5.1).

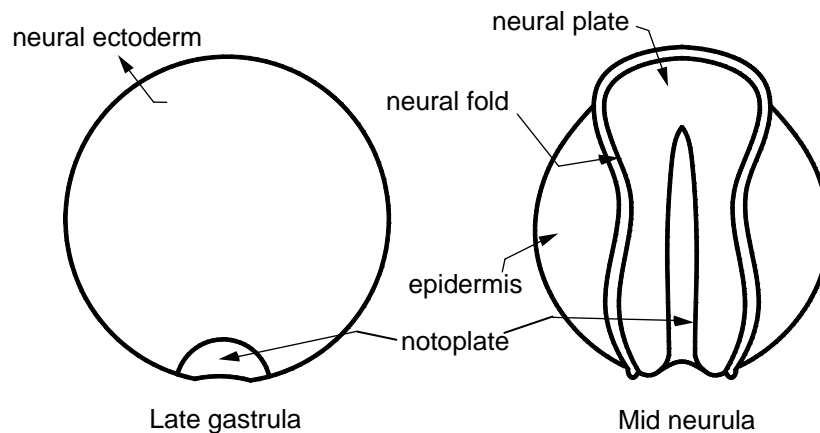


Figure 5.1. Embryonic region identification.

Although the parametric coordinate systems, which will be discussed in the following paragraph, are proposed based on Axolotl embryos, they can also be applied to other species depending on the similarity. The candidates of parametric coordinate system for the neural plate region are listed as follows (Figure 5.2):

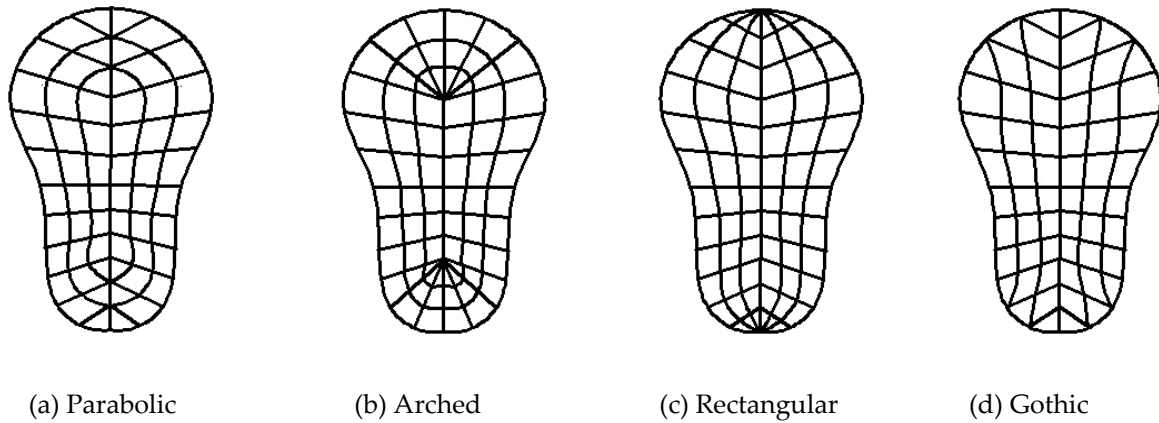


Figure 5.2. Parametric coordinate systems.

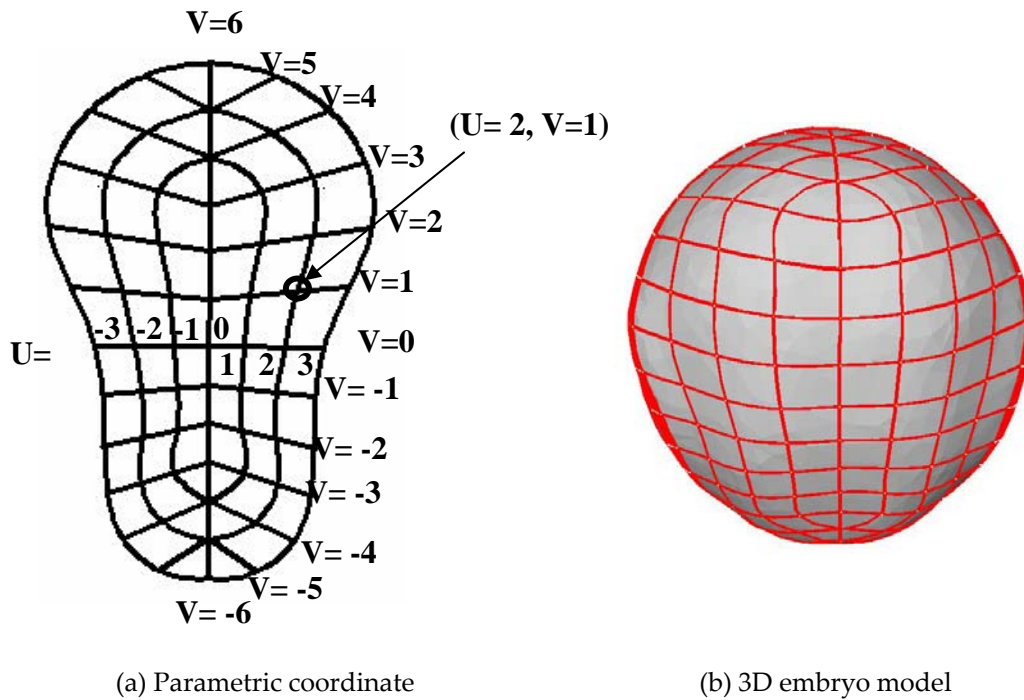


Figure 5.3. Mapping from parametric coordinate onto the 3D embryo model.

The criteria for choosing an appropriate coordinate system are based on requirements such as grid description in the finite element model, programming convenience and interpolation methods. In our FE model the “parabolic” parametric coordinate system is adopted according to the above factors and our observation of cell motion during Axolotl

embryonic development. In Figure 5.3a, each cross point has its  $u, v$  value. If we map the parabolic coordinate system onto the 3D embryo model we can get the result shown in Figure 5.3b. Therefore, each node in parabolic coordinate system will correspond to its peer in the 3D embryo model. We call the grid on the 3D embryo surface a “feature grid”.

From the perspective of coding, the feature grid is a table maintaining the node mapping of  $(u, v) \rightarrow (x, y, z)$  which is used to calculate the transformation from  $(u, v) \rightarrow (x, y, z)$  or  $(x, y, z) \rightarrow (u, v)$ .

### 5.2 Transformation from parametric to Cartesian coordinates $(u, v) \rightarrow (x, y, z)$

For an arbitrary given  $(u, v)$  in a parametric coordinate system, to get its corresponding  $(x, y, z)$  value in a 3D model, a transformation from parametric coordinates to Cartesian coordinates is required. The interpolation algorithm used here can be linear or a higher order polynomial.

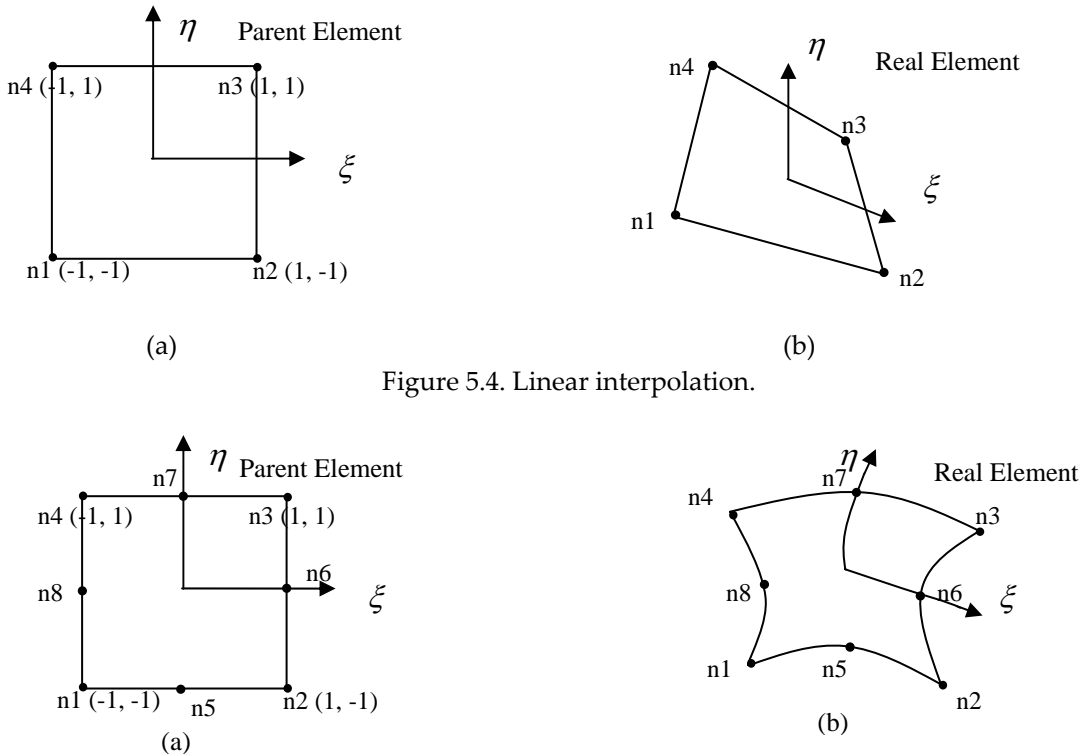


Figure 5.4. Linear interpolation.

Figure 5.5. Quadratic interpolation.

In the case of linear interpolation, shown in Figure 5.4, the weighted value (shape function) on each node is given as follows:

$$\begin{aligned}
 N_1(\xi, \eta) &= \frac{1}{4}(1-\xi)(1-\eta) \\
 N_2(\xi, \eta) &= \frac{1}{4}(1+\xi)(1-\eta) \\
 N_3(\xi, \eta) &= \frac{1}{4}(1+\xi)(1+\eta) \\
 N_4(\xi, \eta) &= \frac{1}{4}(1-\xi)(1+\eta)
 \end{aligned} \tag{5.1}$$

With the  $(x, y, z)$  value of the four nodes, the transformation can be calculated by:

$$\begin{aligned}
 x &= \sum_{i=1}^4 N_i(\xi, \eta)x_i \\
 y &= \sum_{i=1}^4 N_i(\xi, \eta)y_i \\
 z &= \sum_{i=1}^4 N_i(\xi, \eta)z_i
 \end{aligned} \tag{5.2}$$

In the case of a higher order interpolation algorithm, we employ the coordinate mapping of the quadratic element in the finite element method (Figure 5.5). The weighted value (shape function) on each node is given as follows:

$$\begin{aligned}
 N_1(\xi, \eta) &= \frac{1}{4}(1-\xi)(1-\eta)(-\xi-\eta-1) \\
 N_2(\xi, \eta) &= \frac{1}{4}(1+\xi)(1-\eta)(\xi-\eta-1) \\
 N_3(\xi, \eta) &= \frac{1}{4}(1+\xi)(1+\eta)(\xi+\eta-1) \\
 N_4(\xi, \eta) &= \frac{1}{4}(1-\xi)(1+\eta)(-\xi+\eta-1) \\
 N_5(\xi, \eta) &= \frac{1}{2}(1-\xi^2)(1-\eta) \\
 N_6(\xi, \eta) &= \frac{1}{2}(1-\eta^2)(1+\xi) \\
 N_7(\xi, \eta) &= \frac{1}{2}(1-\xi^2)(1+\eta) \\
 N_8(\xi, \eta) &= \frac{1}{2}(1-\eta^2)(1-\xi)
 \end{aligned} \tag{5.3}$$

With the  $(x, y, z)$  value of the four nodes, the transformation can be calculated by:

$$\begin{aligned}
 x &= \sum_{i=1}^8 N_i(\xi, \eta) x_i \\
 y &= \sum_{i=1}^8 N_i(\xi, \eta) y_i \\
 z &= \sum_{i=1}^8 N_i(\xi, \eta) z_i
 \end{aligned} \tag{5.4}$$

Linear and higher order polynomial interpolation algorithms are both implemented in our model depending on situations.

### 5.3 Transformation from Cartesian to parametric coordinates: $(x, y, z)$

$\rightarrow(u, v)$

Transformation from Cartesian to parametric coordinates is not just a simple reverse of transformation from parametric to Cartesian, because we cannot obtain  $(u, v)$  by only solving linear equations. To implement the transformation, a gradually approaching algorithm is adopted. The basic idea of the algorithm [Bootsma, 2003] is to find the four nodes that embrace the input node and then gradually update the  $(u, v)$  to find the closest node to the input node.

The procedure can be summarized as follows:

1. Find the nearest node C to the input node A. (Figure 5.6a)
2. Find the neighbouring nodes of node C ( $n_1, n_2, n_3, n_4, n_5, n_6, n_7, n_8$ ). These nodes compose four quadrants shown in Figure 5.6a. For each quadrant the following steps are performed.
3. Divide the quadrant into four curvilinear quadrants and determine which of these sub-quadrants contains node A (Figure 5.6b). By comparing the distances between the center of each sub-quadrant to node A. For example, node B is the center of the lower-left sub-quadrant that contains node A. The quadrant containing node A becomes the new quadrant.
4. Repeat step 3 until the distance is less than a specified value.
5. The center of the sub-quadrant containing node A is the coordinate.

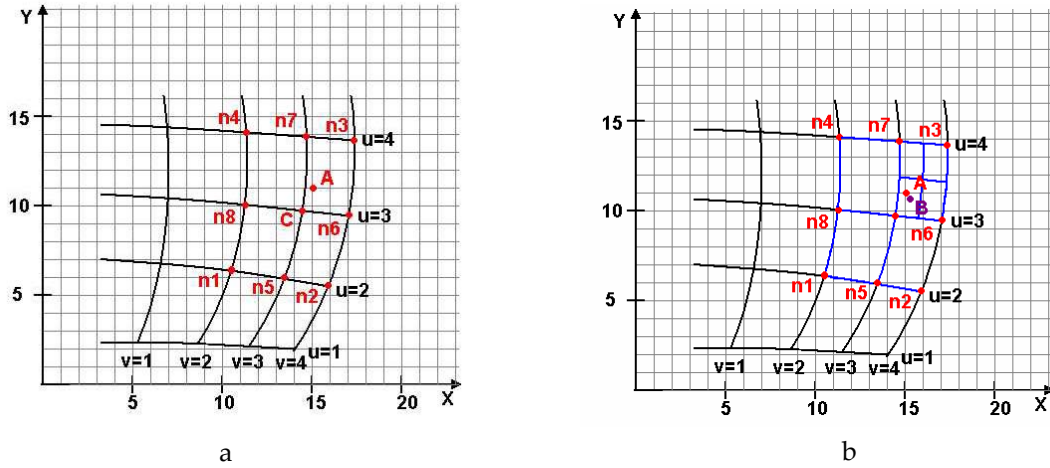


Figure 5.6. Gradually approaching algorithm [Bootsma 2003].

With the function of transformation from Cartesian coordinate systems to parametric coordinate systems and vice versa, transforming a different parametric coordinate system can easily be done as long as a reference frame in the Cartesian coordinate system is provided (Figure 5.7).

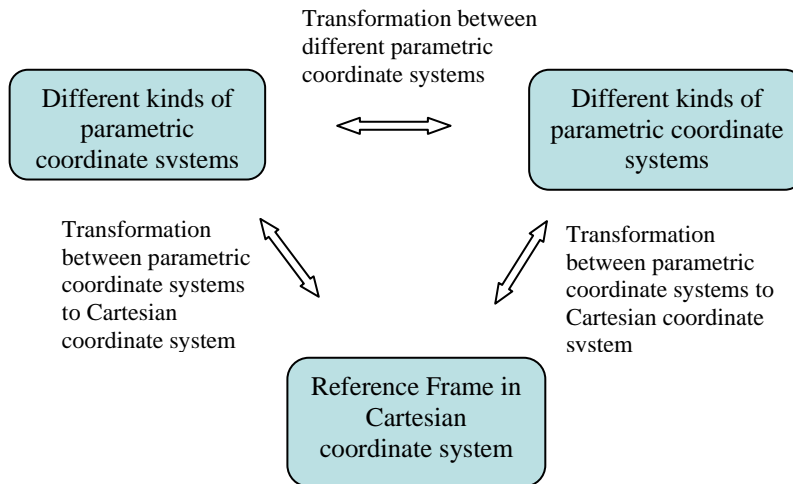
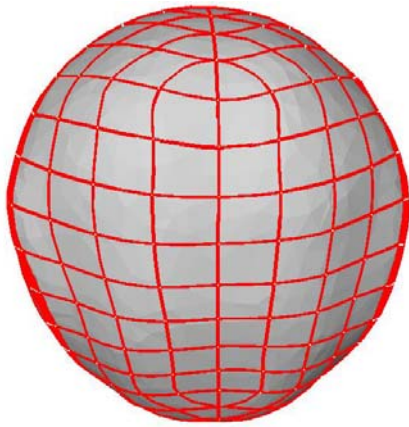


Figure 5.7. Transformation between different coordinate systems.



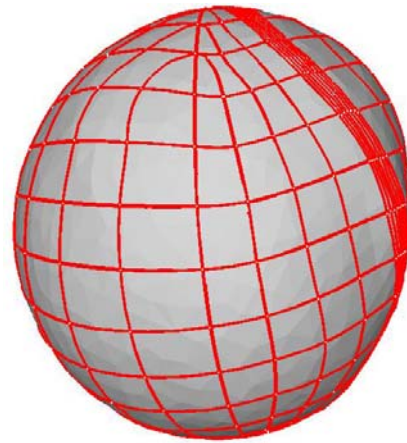
(a) Neural plate region



(b) Neural ridge region



(c) Non-neural epidermis region I



(d) Non-neural epidermis region II

Figure 5.8. Parametric coordinate systems of different regions on embryo's surface.

There are a total of four parametric coordinate systems (two types) used to map the three main regions on the surface of an embryo to the 3D model. For the neural plate region, a parabolic parametric coordinate system is used (Figure 5.8a). For the neural ridge region a radiant coordinate system is used (Figure 5.8b). For the neural epidermis region which has a much bigger area than the neural plate, we divide it in half. For each half, a parabolic parametric coordinate system is applied (Figure 5.8c and d) to make the size of the grids similar to those on the neural plate region.

## 5.4 Database Inquiry System

Spatial-temporal data from different sources are always based on their own parametric coordinate systems, which might be different from the parabolic parametric coordinate system. For instance, the parametric coordinate for electrical fields on embryo surfaces may be planar rectangular coordinates, different from the “parabolic” parametric coordinates we used in the 3D model. Suppose we want to obtain the mechanical properties of one node in the FE model. In one inquiry action for this node, we can only obtain one piece of spatial-temporal data each time. To obtain another type of spatial-temporal data for the same node, we need to repeat the inquiry action because their parametric coordinate systems are different. To reduce the inquiry time, a preprocessing can be applied to convert the data in different parametric coordinate systems into a uniform parametric coordinate system based on different regions of the embryo. With a uniform parametric coordinate system, one inquiry action can provide all the spatial-temporal data for one node.

Two kinds of databases are adopted in our framework; one is the database for the raw data, which can be used to store the original format of these spatial-temporal data. The other one is the database for the preprocessed data, which uses the uniform parametric coordinate system. In the framework, the finite element model will use a “feature grid” to do the data inquiry and interpolation between the two databases. Their relationships are shown in Figure 5.9:

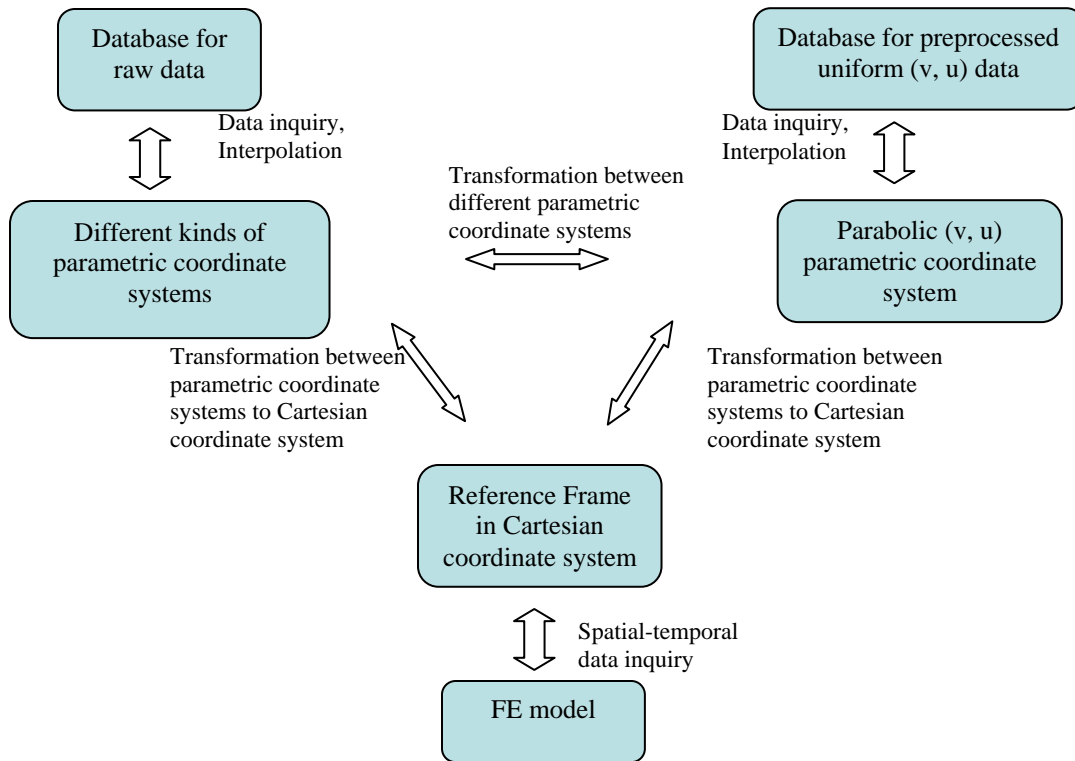


Figure 5.9. Schematic chart for inquiry system.

In these two databases, for each spatial-temporal data type there is one corresponding table (Table 5.1). Each table has these fields: virtual embryo ID, real embryo ID, region ID,  $U$ ,  $V$ , and spatial-temporal data value.

**The virtual embryo ID** represents the reference model of 3D embryo.

**The real embryo ID** is used to track the real embryo from which the experimental data are obtained.

**The region ID** represents the type of region where the spatial temporal data exist.

**The  $(u, v)$**  is the parabolic parametric coordinate value in the database of preprocessed data.

In the raw data database,  $(u, v)$  may change to  $(\xi, \eta)$  or other symbols.

**Spatial-temporal data** can be a real number or a vector.

**Table 5.1. Database table**

| Virtual Embryo ID | Real embryo ID | Region ID | U   | V   | Spatial-temporal data |
|-------------------|----------------|-----------|-----|-----|-----------------------|
| 1                 | 1              | 3         | 2   | 2   | 2.44                  |
| 1                 | 2              | 4         | 3   | -4  | 3.55                  |
| ...               | ...            | ...       | ... | ... | ...                   |

Thus far, the feature grid framework and database inquiry system compose the input functionality of our framework. Based on them, a standard inquiry procedure for a given finite element model can be summarized as follows:

1. Select one node in the model and get its  $(x, y, z)$  value.
2. Use the transformation from the Cartesian coordinate system to the parametric coordinate system in the feature grid framework to determine the region and parametric value of this node. (There are a total of four parametric grids on the embryo's surface, which correspond to different region.)
3. Determine the virtual embryo ID, the real embryo ID, the region ID, U and V.
4. Inquire the preprocessed database to find the spatial-temporal data corresponding to these values. (The conversion from the raw database to the preprocessed database is done before any inquiry action.)

# Chapter 6

## Finite Element Model

### 6.1 Package structure

Like most element method (FEM) packages, our software package can be divided into three main parts, preprocessing, computational engine and postprocessing (Figure 6.1).

#### 6.1.1 Preprocessing and postprocessing:

Preprocessing and postprocessing are usually involved in dealing with geometric configurations, assigning mechanical properties, and visualizing of results. Two main sub-packages are written to serve these functions: ChiChi3D (Figure 6.2) and Zazu (Figure 6.3).

ChiChi3D is a Windows 32 based program which uses the Coin3D library (an open source OpenGL library) to revise, manipulate and visualize the 3D geometry of the tissue scale computational simulations.

Zazu is a MFC (Microsoft foundation class) based program, which uses a number of open source libraries such as image processing and manipulating triangular surface meshes to deal with the 2D geometry of the cellular scale computational simulations.

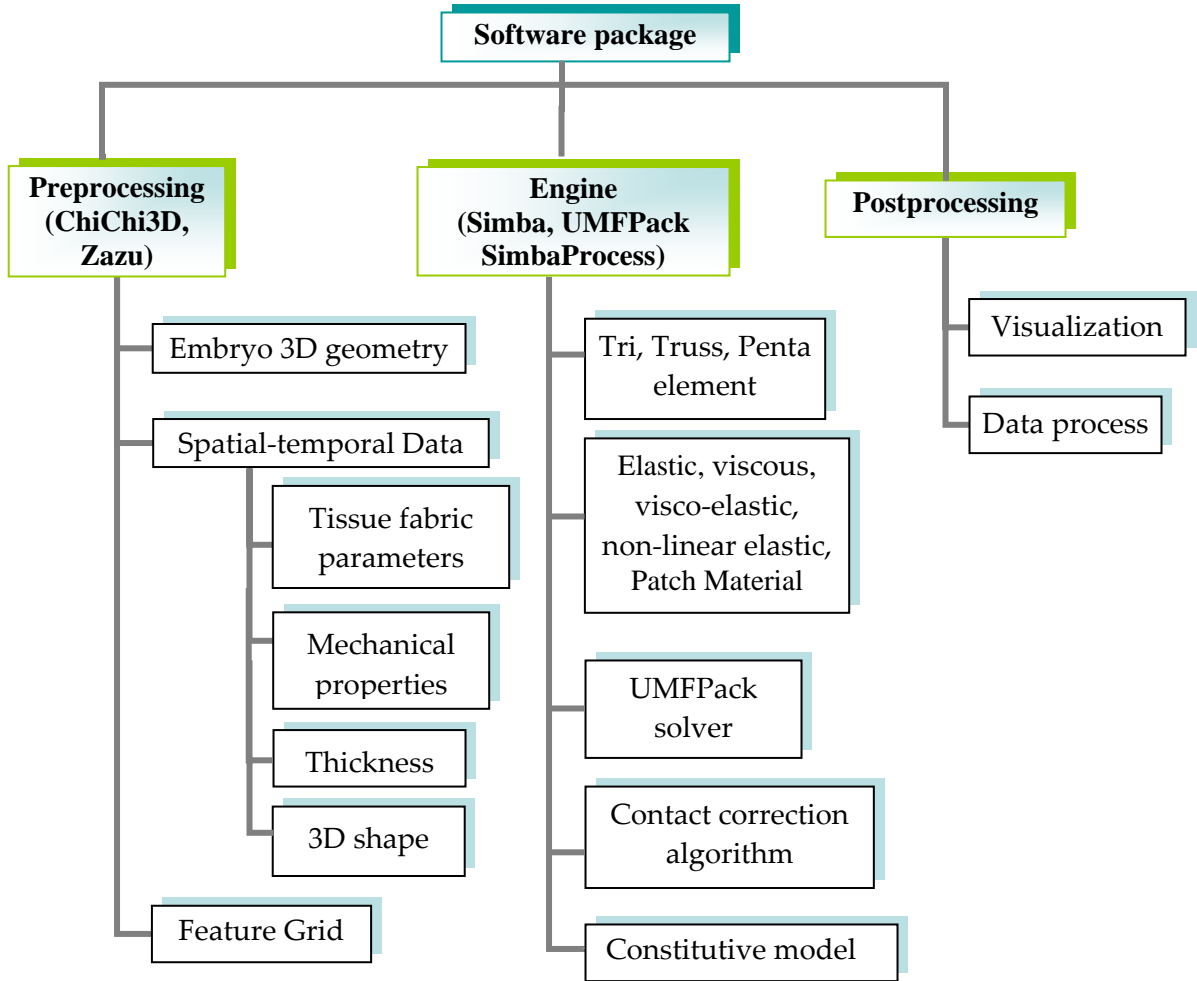


Figure 6.1. Software package.

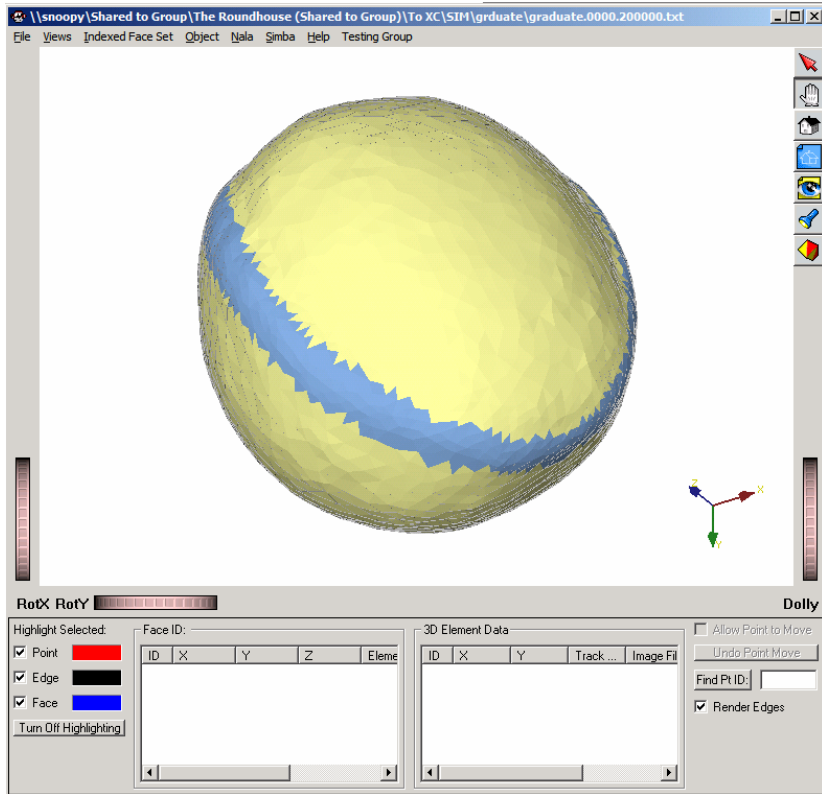


Figure 6.2. Graphic user interface of ChiChi3D.

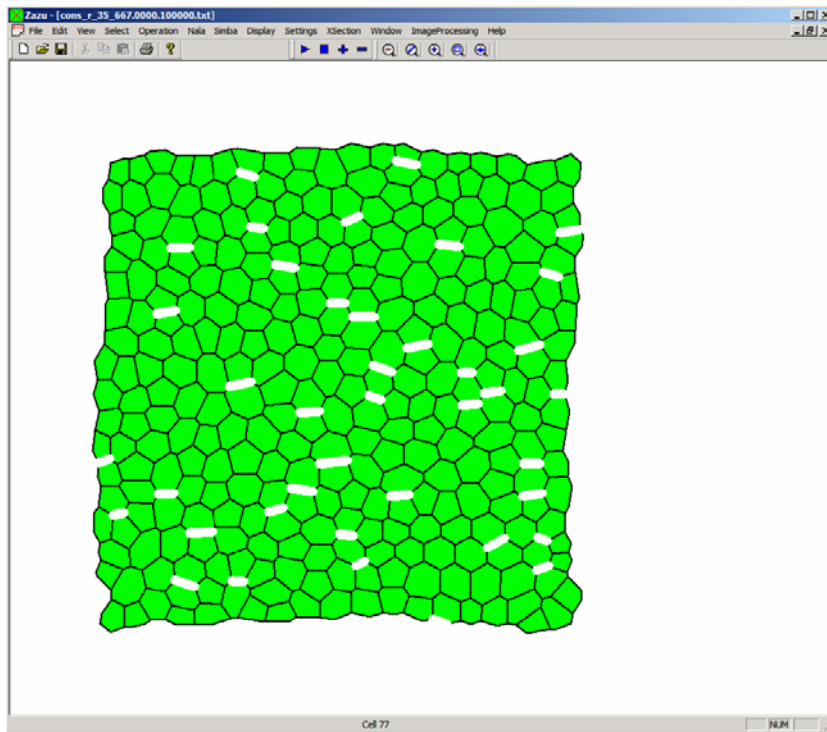


Figure 6.3. Graphic user interface of Zazu.

### 6.1.2 Computational engine

In Chapter 3, the equilibrium equation of this model is:

$$\mathbf{C}\dot{\mathbf{u}} + \mathbf{K}\mathbf{u} = \mathbf{f}, \quad (6.1)$$

where  $\mathbf{K}$  is the stiffness matrix of this model,  $\mathbf{C}$  is the damping coefficient matrix of this model, and  $\mathbf{f}$  is the nodal force (equation 3.31). Note that  $\mathbf{K}$  is zero because there is no elastic element in this model; thus the equation in the incremental form can be rewritten as

$$\mathbf{C}\dot{\mathbf{u}} \approx \mathbf{C} \frac{\Delta \mathbf{u}}{\Delta t} = \frac{1}{\Delta t} \mathbf{C} \Delta \mathbf{u} = \mathbf{f} = \mathbf{f}_{ext} + \mathbf{f}_{int} = \mathbf{f}_{ext} + \sum_{i=1}^r \mathbf{f}_{int}^i. \quad (6.2)$$

By using a forward difference scheme, the non-linear equation can be solved.

To implement this program, custom software called Simba and Simbaprocess are employed. Simbaprocess is a wrapper that connects the Simba library to the UMFPac library for solving asymmetric sparse linear systems (<http://www.cise.ufl.edu/~davis/>).

Simba is a large-strain, large-deformation finite element program written in C++. It works in conjunction with ChiChi3D and Zazu and provides the graphic user interface (GUI) for the construction of geometries, boundary conditions (BCs), and material properties. The features of Simba include:

1. General constraint handling including proportional, edge, and volume constraints. Other boundary conditions include body forces, angled rollers, distributed loads and nodal forces, displacements, velocities, and strain rates.
2. Elastic, viscous, visco-elastic (Maxwell and Kevin-Voigt), truss (including microfilaments), and non-linear elastic materials.
3. 1D, 2D, and 3D elements.
4. Truss, Tri, Pentahedra, and Cell elements (cell elements include neighbouring changing).
5. Error equations for direct solver.
6. Full simulation control through input text file.
7. New materials, elements, and boundary conditions can easily be integrated into Simba.

**Element description****Tri Element**

Tri elements contain 3 nodes and can exist in XY or XYZ space. All element calculations are performed in a local XY space. XYZ calculations are obtained by first rotating the element into the XY plane and then rotating the results back into XYZ space. The input file in XY space may look like this: "5 Tri EL1 EC2 5 7 8 5.4 1.0," meaning that element 5 is a tri element using material EL1, element control EC2 and connecting nodes 5, 7 and 8 with a thickness of 5.4 and a growth factor of 1.0. Other optional parameters may also be specified such as age, color, or residual stresses.

**Truss Element**

Truss elements contain 2 nodes and can exist in X, XY or XYZ space. The input file may look like this: "5 Truss VI1 5 7 5.4 1.0," meaning that element 5 is a truss element using material VI1 and connecting nodes 5 and 7 with a cross-sectional area of 5.4 and a growth factor of 1.0. Other optional parameters may also be specified such as age, colour or residual stresses. Truss elements currently do not have an element control.

**Pentahedra Element**

Pentahedra elements contain 6 nodes. The input file may look like this: "5 Penta VIPenta5 ECPenta5 2 3 4 5 6 7 InitialVolume 49018.6," meaning that element 5 is a Pentahedra element using material VIPenta5, element control ECPenta5 and connecting nodes 2, 3, 4, 5, 6 and 7 with an initial volume 49018.6. Each Pentahedra element typically represents a group of 1 to 100 cells. The volume of each Pentahedra element remains constant. Each Pentahedra element has two Tri elements, one attached on the top and the other one on the bottom (Figure 6.4). In the above example, one Tri element consists of nodes 2, 3, 4 and the other Tri element consists of node 4, 5, 6. The volume constraints for Pentahedra element are implemented by adding an auxiliary node in the center of the Pentahedra element. By connecting this node to the 6 nodes of the Pentahedra element we obtain 8 tetrahedrons. The volume of the Pentahedra element is calculated based on these 8 tetrahedrons, and the

Lagrange multiplier is employed to ensure a constant volume constant. Figure 6.4 illustrates how elements are employed in the 3D finite element model. The FE model uses a group of Pentahedra elements to represent one layer of the embryo. So far, we have simulated the morphogenesis with one layer, but it is not difficult to add more layers to our model with more Pentahedra elements.

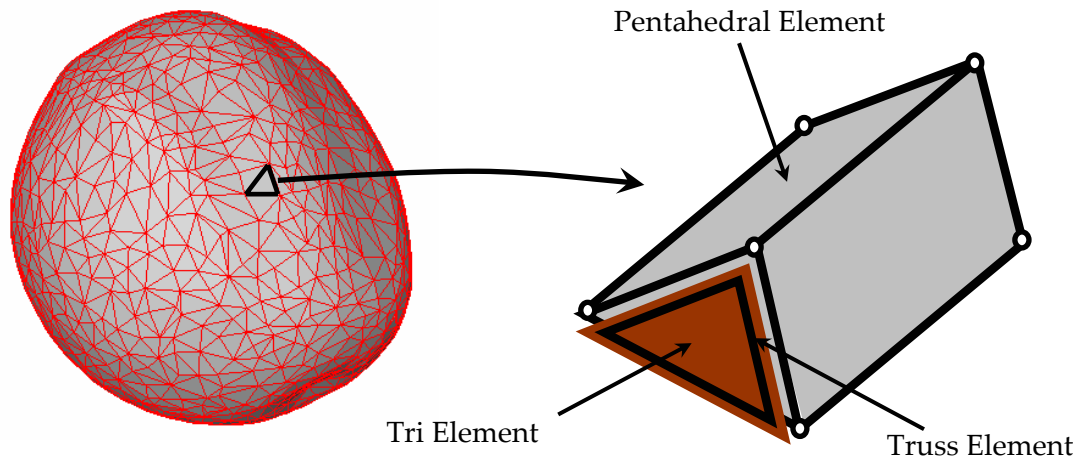


Figure 6.4. Pentahedral element.

### Material description

Material descriptions available in Simba include elastic, viscous, visco-elastic (Maxwell and Kelvin-Voigt), truss (including microfilaments) and non-linear elastic. A supplementary class (Patch material) is incorporated in the package to represent the tissue fabric parameters such as  $\alpha$ ,  $\beta$  and  $\kappa$ . The Patch material usually works in conjunction with the Tri element. The shape change of the Tri element affects the tissue fabric, thereby changing the properties of the Patch material. Corresponding functions for changes in  $\alpha$ ,  $\beta$  and  $\kappa$  over time are embedded in the Patch material routines.

### Element Control description

Element controls (ECs) contain additional descriptions that usually apply to many elements. ECs serve to assign a certain material property to one element or a group of elements. Each element type has a corresponding EC type. The following ECs are supported: ECTri, ECPenta and ECCell. Truss elements do not have an Element Control class.

### Boundary Condition description

There are several supported types of boundary conditions (BCs): Node, Contact, Distributed Load (DL), Angled Roller, Function, BodyForce, EdgeN, EdgeTN, Volume Constancy, and Corner. Node and Corner Boundary conditions specify the force, displacement, velocity or strain rate of a single node. In contrast, Edge, Function, Angled Rollers and Volume conditions specify a relationship between all nodes that are part of that condition. Body forces are applied to an element or group of elements and affect the nodes that are connected to that element or group. DLs apply to an edge and affect all nodes along that edge.

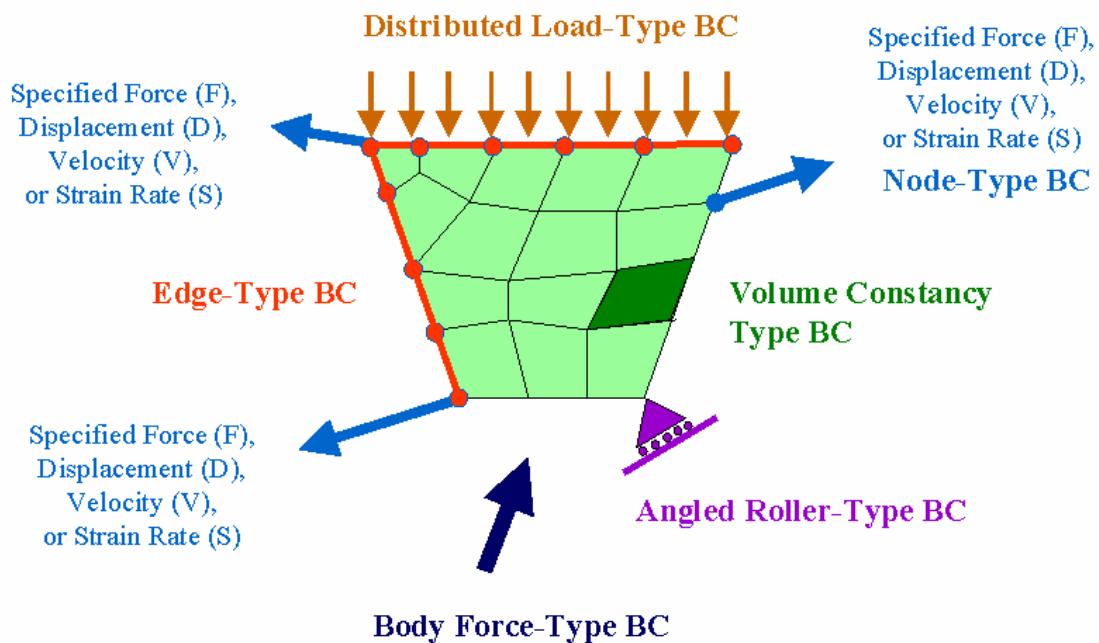


Figure 6.5. Various boundary conditions.

### **Description of linear system solving engine**

The introduction of the Lagrange multiplier and the implementation of complex boundary conditions bring asymmetry to the system of simultaneous equations that must be solved incrementally. The open source package UMFPack (<http://www.cise.ufl.edu/~davis/>) is employed to solve the resulting asymmetrical sparse linear systems using an asymmetrical multiFrontal method.

The detailed steps for conducting 3D and 2D simulations are summarized as follows:

#### **Steps for 3D simulations:**

1. Obtain a 3D reconstruction of an Axolotl embryo and open with ChiChi3D.
2. Use “attach feature grid” function of ChiChi3D to assign feature grid to the surface mesh of the embryo.
3. Extend the nodes on the triangular surface mesh perpendicularly to the surface at a distance determined by the thickness data stored in the database.
4. Connect the top and bottom triangular surface to generate a Pentahedra element.
5. Assign Patch material to Tri elements on the top and the bottom of Pentadhedra element and Viscosity material to the Pentahedra element.
6. Set the volume constraint of the Pentahedra element and the volume constraint of the extracellular fluids contained in the center of the embryo to be constant.
7. Output the finite element model as .txt file which can be edited with a general text processor.
8. Execute Simbaprocess.exe in Windows console or Linux console with the above output file name as an input parameter. Simbaprocess generates the result .txt files for every time step, and they can be viewed and manipulated with ChiChi3D.

#### **Steps for 2D simulations:**

1. Use Zazu to generate a 2D Voronoi mesh with specific size and properties.
2. Output the model as .txt file, and use text processor to modify the boundary conditions (BCs) and material properties.

3. Execute Simbaprocess.exe in Windows console or Linux console with the above output file name as an input parameter. Simbaprocess generates the result .txt files for every time step and they can be viewed and manipulated with Zazu.

## 6.2 Contact Algorithm

In our computational simulations of the rolling up of a neural plate strip some elements would contact others and penetrate one another as the rolling up progresses (Figure 6.6). A contact correction algorithm is therefore fashioned to address this problem.

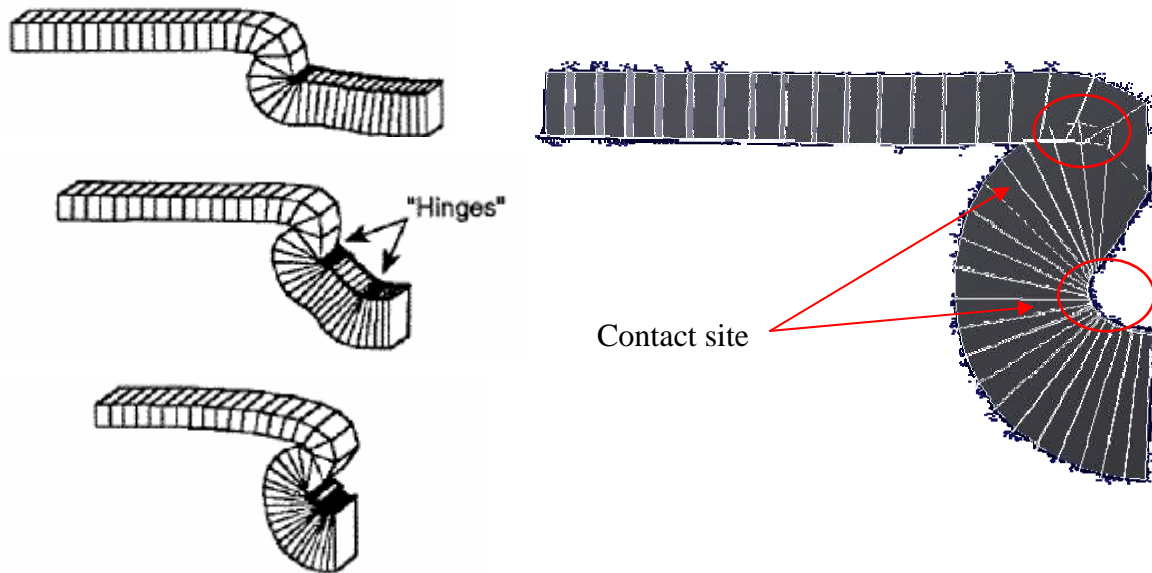


Figure 6.6. Contact problems.

Contact correction algorithms fall into these two categories: Lagrange Multiplier methods and penalty methods. The first one is a generalized method, which is widely used as an implementation of constraint conditions in the FEM. In the Lagrange Multiplier method, the contact constraint means that no penetration happens between two contacting elements, and this constraint is enforced in each iteration step. The method does not need any additional parameters to describe the contact problem, and it supports different friction

conditions. Although the Lagrange Multiplier method can guarantee non-penetration on every point of the surface of the contact element, it comes at a price. That is the updated stiffness matrix becomes significantly more complex than the original one. Thus, it is more difficult to solve.

In the penalty method, a penalty force will be applied to the penetrating node and will allow the time integration to correct the penetrations. The force is dependent on many parameters such as surface stiffness.

The procedure of penalty methods can be summarized as follows [Wriggers, 1996]:

1. Perform the regular FE procedure without considering the contact problem.
2. Search for global and local contact, calculate of the penetration distance, and then calculate the corresponding nodal contact force.
3. Update the nodal displacements and velocities.

To avoid the complexity of stiffness matrix by using Lagrange multiplier and the difficulties for defining additional parameters to describe the contact problem, we employ a relatively simple algorithm to implement the contact correction problem.

The basic idea of our algorithm [Wiebe, 2002] is that a backward action will be done if any penetration is observed. The procedure can be summarized as follow:

1. Complete the routine FE iteration with a search of penetration at every iteration step.
2. If a penetration is found (Figure 6.7a), go back to the configuration of the last step and set up a constraint between the penetration node and the element (Figure 6.7 b) (the functional constraint is implemented by the Lagrange Multiplier).
3. Continue the routine FE iteration.
4. If the node moves to the boundary of the attached element, free the constraint (Figure 6.7d).

The functional constraint in step 2 can vary. It can allow the nodes to move freely on the surface or with friction. In our current model, the 3D embryo has only one layer, but in future work there will be three layers in our model. The friction constraint is intended to simulate the contact of between the layers.

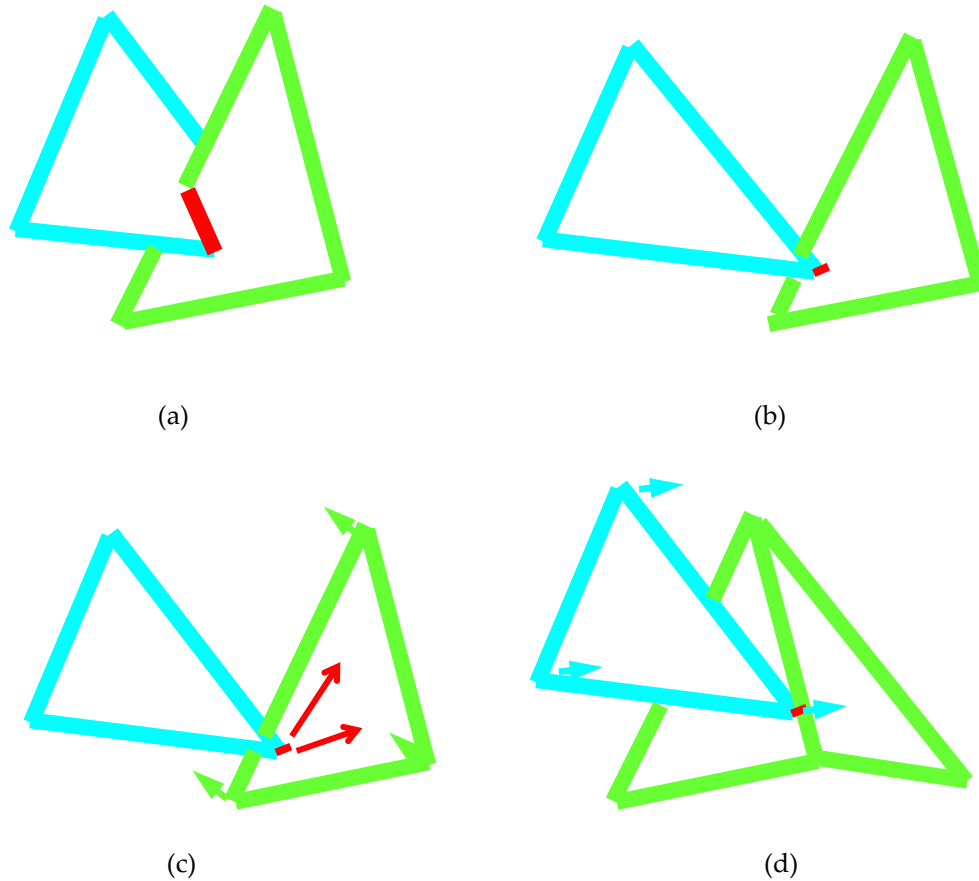
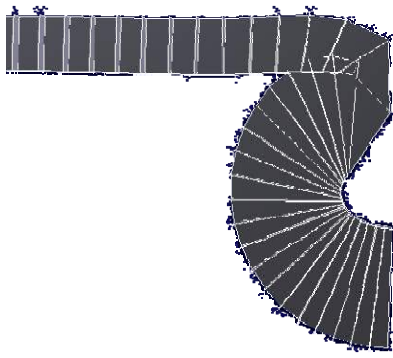


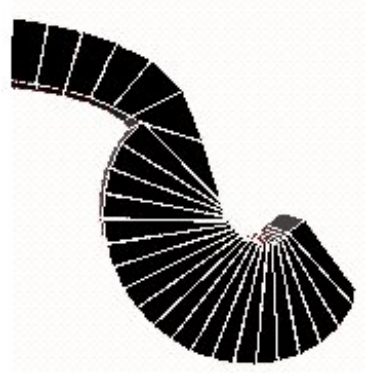
Figure 6.7. Schematic of contact algorithm.

In our penetration search, we calculate the cross section of the two elements to determine the occurrence of contact event happening. We assume that if two elements can pass through, there will be some penetration elsewhere. Going back to the last time step and applying functional constraints will reduce the possibility of this permeability issue.

The contact conditions involved in neurulation process is not very severe compared with those high-speed crashing problems. And most of them occur in the late stage of embryonic neurulation. Although this algorithm simplifies the contact problem to some extent, and no contacting forces are generated, according to our model, no elastic element exists. This simplification functions to avoid the crashing of the program and generate realistic results (Figure 6.8).



(a)



(b)

Figure 6.8. Comparison of simulation with and without contact algorithm. (a) Without contact algorithm. (b) With contact algorithm.

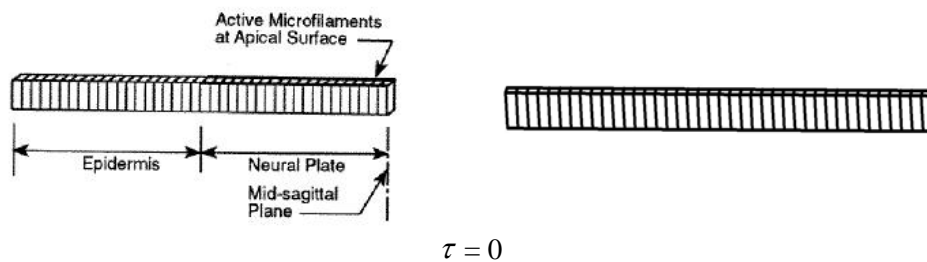
# Chapter 7

## Computational Simulations

### 7.1 Reference case for normal Axolotl embryo development

Sets of conditions associated with specific hypotheses were input into the computational model introduced previously. Due to the complexity of the numerics, a typical run required nearly a week to complete on a powerful PC, and manual intervention was frequently required to overcome numerical issues. Thus, the cost of running simulations is quite high. Many tens of simulations were run in total, and the most instructive and trustworthy are shown here.

As part of the code validation, the software is used to duplicate previously run simulations of the transverse aspects of neural tube development [Clausi and Brodland 1993]. The comparison is shown in Figure 7.1. In Clausi's simulation, the apical contraction force is simulated by truss elements, while in our recent tests, the contraction force is determined by tissue fabric evolution.



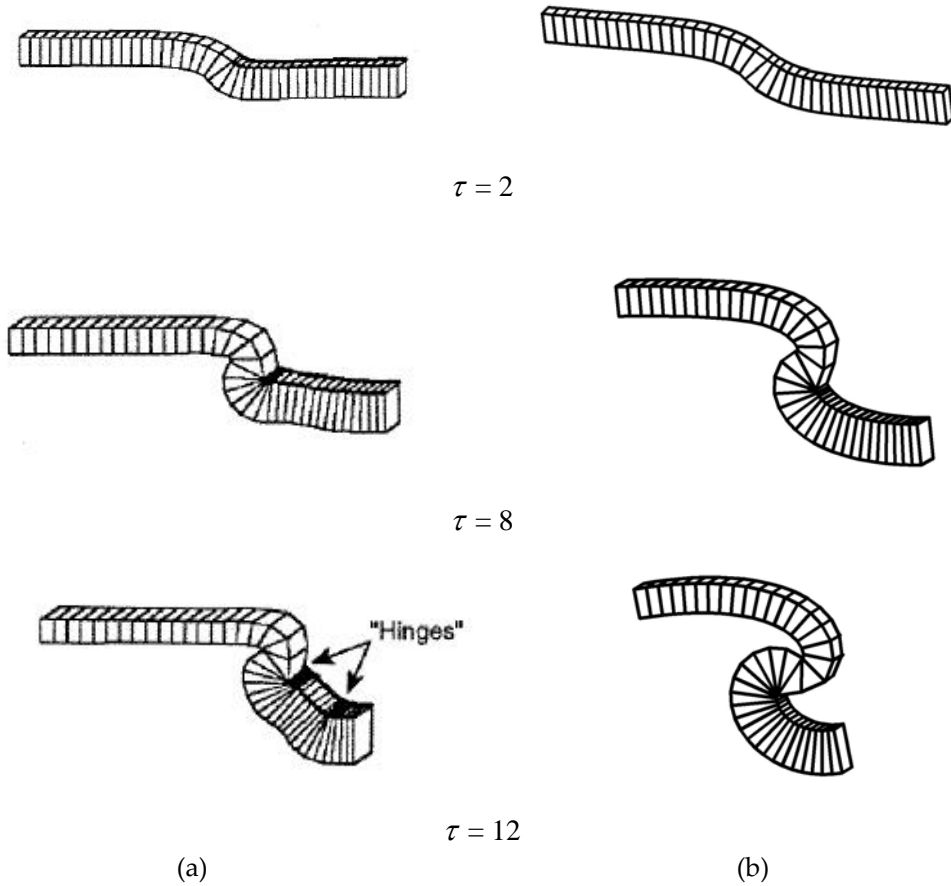


Figure 7.1. Comparison of simulations of a transverse strip of tissue. (a) Clausi's Simulations (b) tissue scale model computational simulations.

As mentioned in the introduction, the details of the force and mechanical properties of tissues and cells are very important to the success of our model. The process how we obtained a whole-embryo simulation of normal neurulation is a rather long story. A great number of simulations were conducted to determine the mechanical properties “necessary” to generate the correct embryo geometry. As expected, the model served, in part, to identify key mechanical features that were not included in our previous understanding of neurulation.

We first started from Clausi's model by expanding the simulation of a strip of neural plate tissue to the simulation of a whole embryo. Initially, values of mechanical properties such as  $\gamma$  and  $\mu$  were adopted from Clausi's model. In the Clausi model, apical constriction and axial elongation are sufficient to produce realistic motions that result in neural tube

closure. However, when these properties are applied to a 3D model, abnormal geometries result. We thus realized that the transition from 2D simulations to 3D simulations is not as easy as expected. More details and constraints needed to be incorporated into our model.

As our next step, we explicitly included the volume constraint of the fluid and cells that form the central portion of the embryo, something that was not necessary in the Clauis model.

We also recognized from the biological literature that an active convergence-extension process was occurring in the neural plate [Keller, 2005; Wallingford, 2002]. To this end, we introduced a lamellipodium-driven convergent-extension effect. Initially, we assumed that the lamellipodium effect was uniform across the neural plate region, and the result we obtained was not very satisfying. A more careful examination of the literature showed that the effect of teratogens varies with the medio-lateral position at which it is applied [Wallingford, 2002]; the medial tissue seems to be more important to tube closure than lateral tissue. With this in view, we made the lamellipodium effect decrease linearly from the midline of the embryo to the lateral edge of the neural plate. Realistic keyhole-shaped in-plane geometries resulted, but the neural folds did not rise appropriately.

The tissue in the neural fold region is known to have different mechanical properties than the tissues on each side of it due to Shroom expression effects [Haigo *et al.*, 2005]. To capture this fact, the  $\gamma$  and  $\mu$  values in neural fold region were made different from those in the neural plate region and the non-neural epidermis region. To facilitate the occurrence of neural folds we assumed constriction on the basal surface of the tissue in the neural fold region. Although the gene, Shroom, expressed there is associated with apical constriction forces applied to the basal surface produce more satisfactory ridges.

A number of numerical challenges arose. For instance, the Penta element sometimes can not describe the convoluted twisting motions that occur in cell groups near the neural ridges. A specific constraint is imposed on Pentahedra elements to prevent excessive element deformation.

This model refinement process led to an improved understanding of the mechanics of the neurulation process.

For the whole-embryo simulations, the surface geometry is reconstructed using data from the Frogatron 3000. The approximate diameter of the embryo is 2200 $\mu\text{m}$ . To simplify the modeling and computation, only one ectoderm layer is explicitly represented in the model and its thickness (30~60 $\mu\text{m}$ ) profile is determined from serial section data.

A typical whole finite element model consists of 10239 Pentahedra elements, but the number can be increased or decreased as needed to model specific feature associated with particular hypotheses. Each Pentahedra element is attached to Tri elements on its top and bottom surfaces. The tissue fabric parameters are included in the Tri element material. The whole-embryo model is like a shell containing liquid in its center, and the volume of the liquid remains constant. The whole-embryo model is divided into three parts which are shown in the Figure 7.3 with different colors. Yellow represents the neural plate region, the blue area represents the neural fold region and green means the non-neural epidermis region.

#### 1. Neural plate region

As described in the introduction, neural tube closure involves apical constriction, convergent extension (CE), and other mechanisms (Figure 7.2). In current simulations, apical constriction is modeled by assigning a larger value to  $\gamma$  in the top Tri element of the Pentahedra element than in the bottom Tri element. The microfilament constriction can cause the top surface area of the cell to constrict. As for convergent extension, cells rearrange to drive the narrowing of tissue. Additional force will be generated and the Pentahedra element shape is narrowed in a specific direction while the fabric parameters of the Pentahedra element remain constant. Further details are provided in later sections.

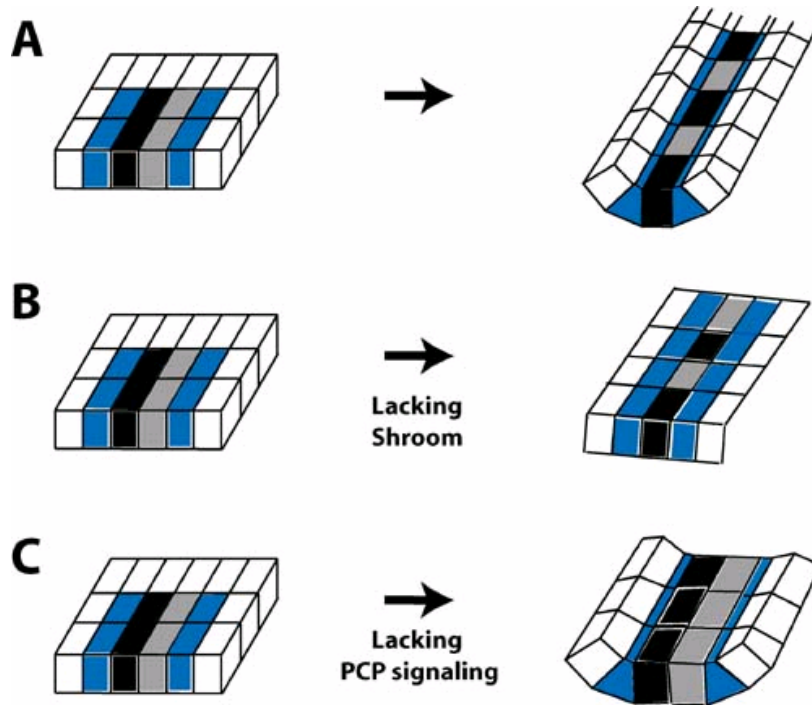


Figure 7.2. Apical constriction and convergent extension facilitate the medial movement of neural folds [Wallingford, 2005]. A: Bending of the neural plate by apical constriction (blue cells) can facilitate neural tube closure. Convergence of the midline (gray and black cells) can also contribute to neural tube closure, by progressively decreasing the distance between the neural folds. B: In the absence of Shroom, apical constriction fails, as does neural tube closure. C: In the absence of PCP signaling, convergent extension fails, as does neural tube closure. Experiments now suggest that apical constriction is primarily involved in rostral neural tube closure, while convergent extension is more important for caudal neural tube closure.

## 2. Neural folds region

There are quite a few hypotheses about how neural folds are shaped in this particular way. One hypothesis attributes it to the pushing of non-neural epidermal tissue [Lawson *et al.*, 2001], and the other one assumes it to be byproduct of the rolling up of the neural plate [Odell *et al.*, 1981]. Both mechanisms have been implemented in our model.  $\gamma$  is set to zero in this region and  $\mu$  carries the same value as the one in the neural plate region and the non-neural epidermis region.

## 3. Non-neural epidermis

The common understanding of non-neural epidermis is that these tissue movements are stretched by narrowing and rolling up of the neural plate. They react passively to the force generated by neural plate movements. However, recent studies indicate that the non-neural epidermis may also contribute to the rolling up of the neural plate, and in some cases [Lawson *et al.*, 2001] it is even the main driving force of neural ridge formation. Based on these facts and the hyperextension work done by Beloussov [Beloussov, 1990; Beloussov, 2006; Cherdantsev, 2006; Lakirev and Beloussov, 1986], we later introduce biomechanical feedbacks into the current model so that the convergent extension in the neural plate area can induce a CE-like behaviour in the non-neural epidermis (Figure 7.3). The comparison in the later section shows that a more realistic geometry can be obtained.

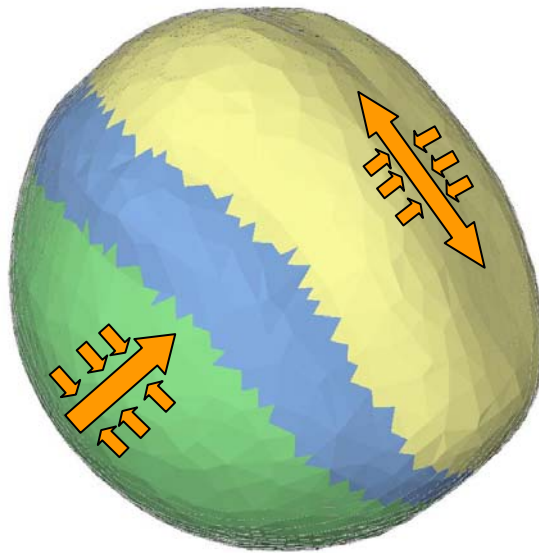


Figure 7.3. The CE-like behaviour in the non-neural epidermis. The convergent extension direction in the non-neural epidermis is perpendicular to that in the neural plate area. The large arrows indicate the extension direction and the small arrows indicate the convergent direction.

Different mechanical properties ( $\mu$ ,  $\gamma$ ) are assigned to the three regions according to different scenarios. And to simplify the problem, all these regions begin with isotropic fabric parameters ( $\kappa=1$ ). The computational simulations for normal embryonic neurulation (the reference case) are conducted and demonstrated in Figure 7.4 (Table 7.1 case 1).  $\gamma$  is 61 nN

in the neural plate region, 0 in the neural folds region and 9.15 nN in the non-neural epidermis region.  $\mu$  is 0.016 nN min /  $\mu\text{m}^2$  in all these regions. These values are obtained by back calculations based on tissue stretching tests [Wiebe and Brodland, 2005]. Convergent extension and apical constriction are enabled in our simulation. Convergent extension (lamellipodium effect) are applied to the model by imposing a lamellipodium stress in the Tri elements. The value in the midline is assumed to be 20 nN /  $\mu\text{m}^2$ . Images of stage 13,14,15,17 are reported here. The left column is the schematic representation of Axolotl's embryonic neurulation process. The right column is its corresponding computational simulation. The ratio of the length in the caudal-cephalic direction over the length in the medio-lateral direction is recorded and compared with the real embryo. The ratio changes from 1 to 1.29 in the real case, and the simulation result moves from 1 to 1.21. The time span from stage 13 to stage 17 is about 8 hours, and the simulation result is slightly different at 5 hours. The choice of  $\gamma$  and  $\mu$  can easily account for this discrepancy. The tissue fabric evolution is also tracked in our simulation.  $\kappa$  from a different area on Axolotl's embryonic surface is extracted through image processing software.  $\kappa$  in the neural plate area changes from 1 to 1.05~1.2 in real cases, and the simulation yields the same result. Other quantitative comparisons are also available. The simulation results show that the change in the neural plate area and the change in the neural fold's perimeter are quite close to the real case. In addition, we measure the stress resultant of embryonic epithelia [Benko and Brodland, 2007] by cutting a slit on the surface the embryo. However, the data is not quite consistent with our simulation result. Part of the reason may be the techniques used to make a slit on the embryo bring errors into the experiment. Another reason could be that unknown genes may express themselves in the neural plate and change the force of cell microfilaments, which in turn change the stress in embryonic epithelium. More accurate experiment data and understanding of gene expression in the neural plate need to be obtained to make the stress resultant comparison.

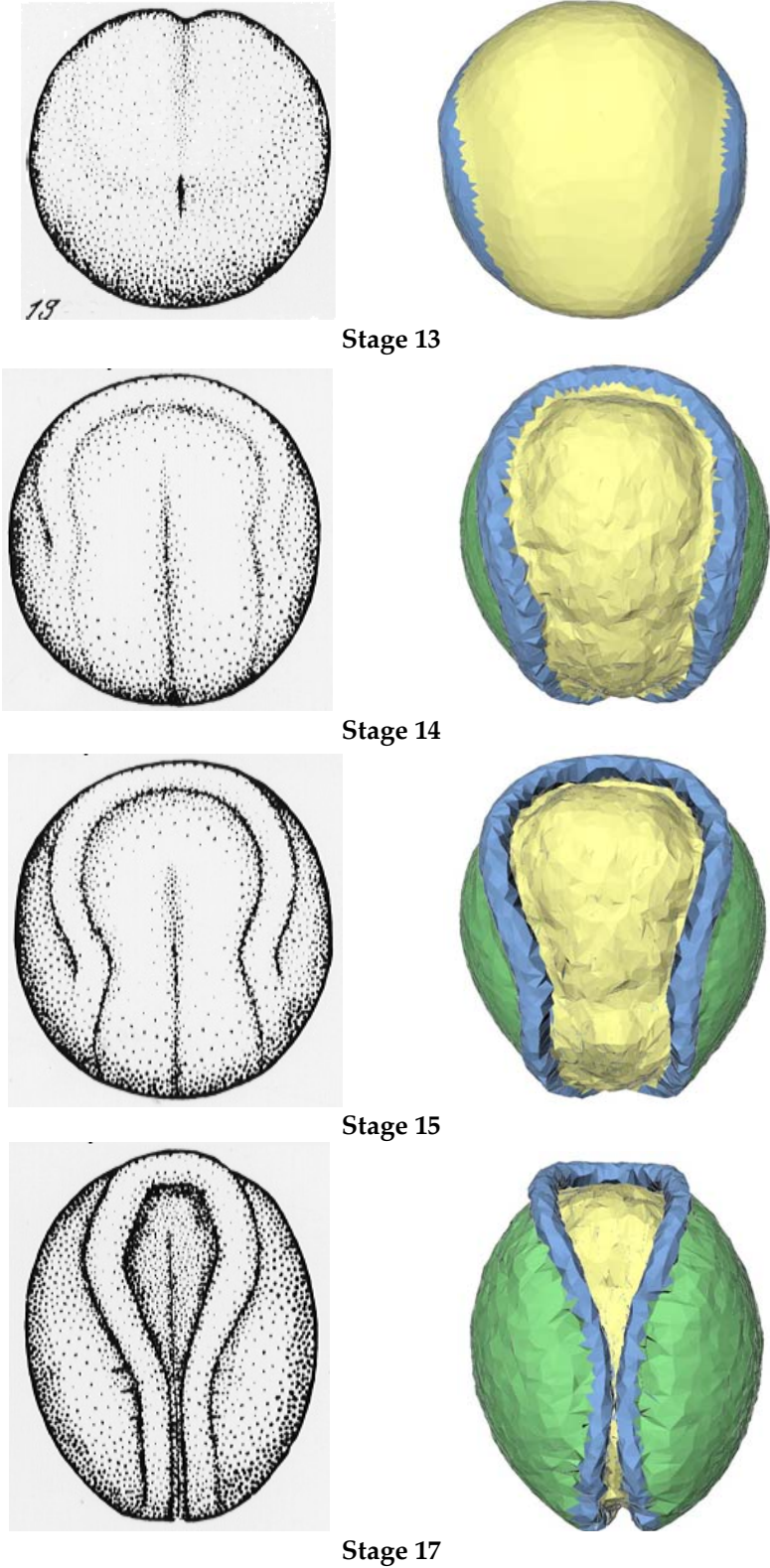


Figure 7.4. Normal development of Axolotl embryo (Table 7.1 case 1).

## 7.2 Impact of tissue mechanical property defects on neurulation

To investigate the impact of the mechanical property defects on Axolotl embryo neurulation, two simple cases, the mechanical property defect on the neural plate (Table 7.1 case 2) and the mechanical property defect on the non-neural epidermis (Table 7.1 case 3) are conducted here.

In the first case, we change the neural plate area to 80% of its original size and keep the fabric parameters and mechanical parameters unchanged: The  $\gamma$  is 61 nN in the neural plate region, 0 in the neural folds region and 9.15 nN in the non-neural epidermis region.  $\mu$  is 0.016 nN min/ $\mu\text{m}^2$  in all these regions. The neural plate region in the left column which is indicated in yellow is 80% of the one in the right column, all shown in Figure 7.5. This defect in the neural plate region leads to abnormal results. The neural folds do not close properly, and the cross-section image shows that the neural folds are not attached to the neural plate which is not consistent with the reference case.

The second case is shown in Figure 7.6.  $\gamma$  in the non-neural epidermis is set to be 18.3 nN, 2 times its original amount. The other parameters are not changed. The change leads to an incomplete closure of the neural plate. The neural folds are separated by a half-width of the neural plate. This result also leads to the detachment of neural folds from the neural plate.

From the simulations of the two cases, we find that the impact of mechanical property defects is quite huge, and these defects may as well be the direct cause of neural tube closure defects. Corresponding experiments on chemically induced mechanical property defects in the neural plate tissue provide the direct proof of this standpoint [Kakal, 2007]. The injected chemical material disassembles the microfilaments in cells which can be implemented with the adjustment of  $\gamma$  in simulations. The disassembly of microfilaments leads to the reduction in surface tension, in turn causing a severe neural tube defect.

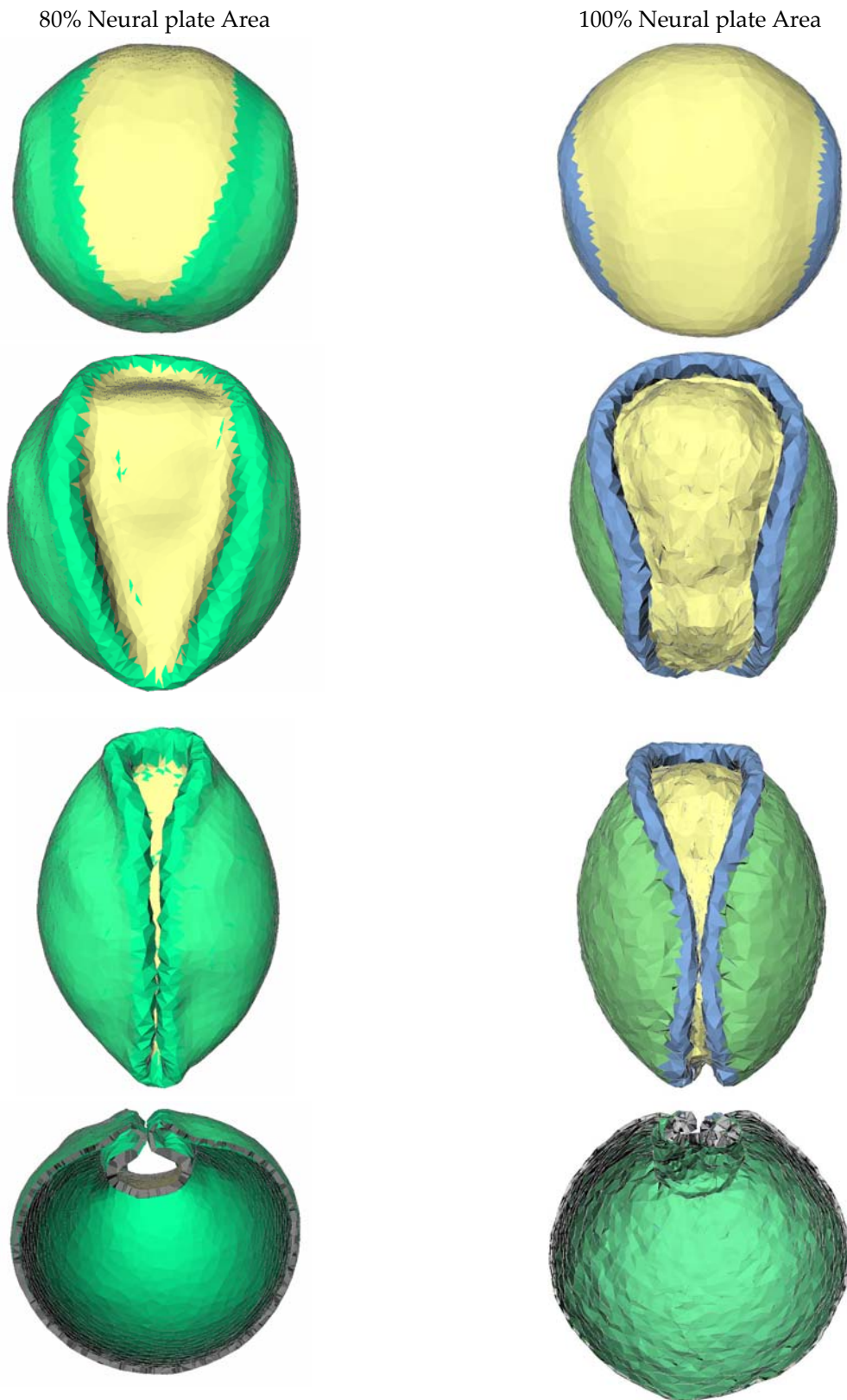


Figure 7.5. The mechanical property defect in neural plate region (Table 7.1 case 2).

Non-neurual epidermis  $\gamma = 30\%$  of neural Plate

Non-neurual epidermis  $\gamma = 15\%$  of neural Plate

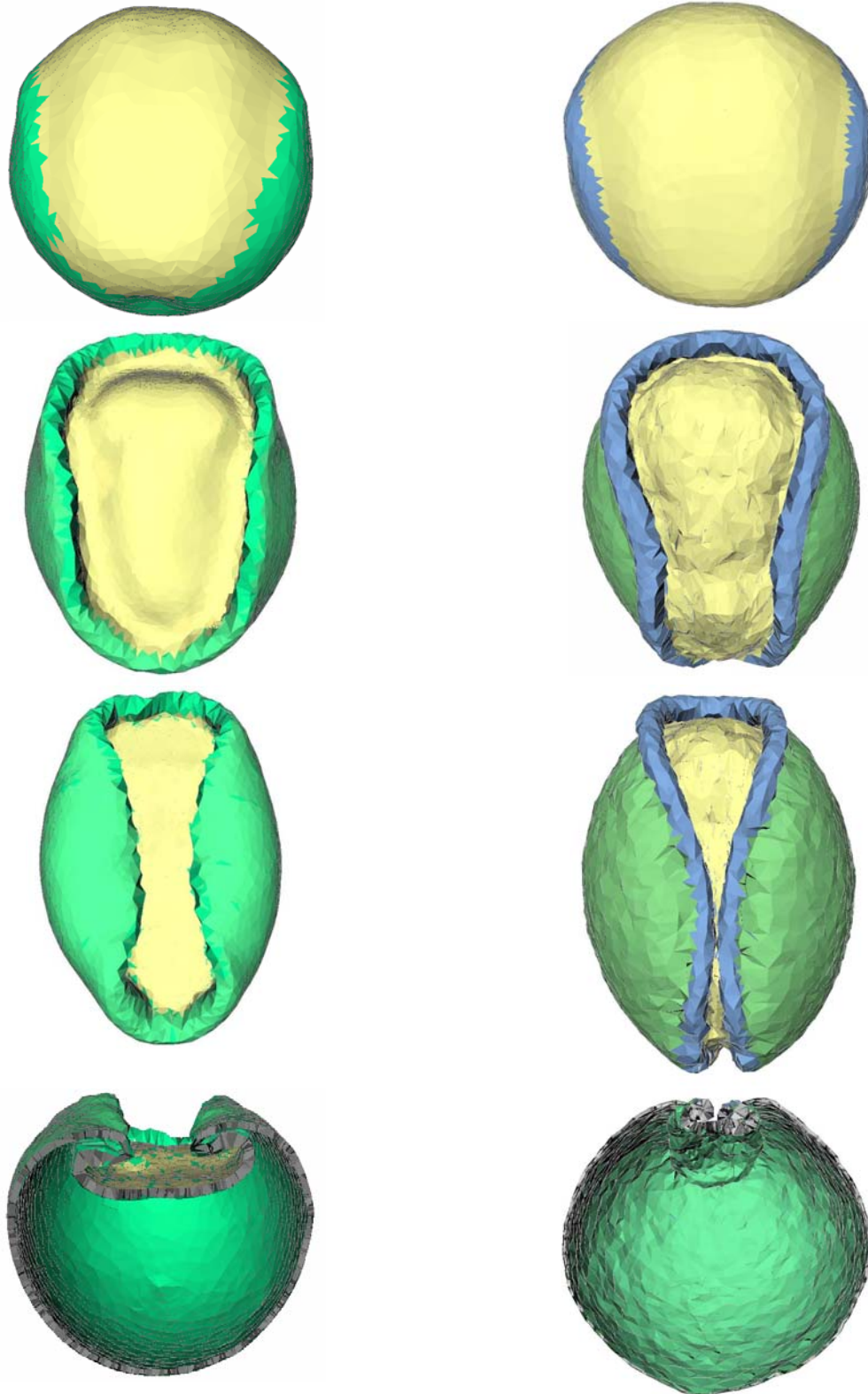


Figure 7.6. The mechanical property defects in non-neurual epidermis region (Table 7.1 case 3).

## 7.2 Impact of biochemical mechanism defects on Axolotl neurulation.

### Apical constriction

Recent studies [Haigo *et al.*, 2003] have shown that the protein Shroom is sufficient to induce apical constriction of neural plate cells [Hildebrand, 2005]. And it is also important to note that apical constriction during neurulation does not occur uniformly throughout the neural plate. The protein Shroom concentrates in the area of the midline of the neural plate and the boundary between the neural plate and the neural folds. Because the cells in these regions have a wedge shape, they are usually called hinge points. To study the impact of the apical constriction defect on neurulation, we disable the apical constriction mechanism in our simulation by setting the  $\gamma$  value of the Tri element in those regions to the same value as those in the non-neural epidermis region (Table 7.1 case 4). The simulation result is demonstrated in Figure 7.7e (normal case) and 7.7f (Shroom disabled), and Figure 7.7 a, b, c, d are their corresponding biological experiments. The embryo used in the biological experiment is *Xenopus*, a kind of frog like Axolotl. The difference between them is the embryo size and the development time period. In the experiment, The *Xenopus* embryo is injected unilaterally and bilaterally with Xshroom-MO (a deletion mutant to disable Shroom expression). This change leads to missing hinge points (the noticeable boundary between neural plate and neural folds), which in turn cause a severe neural tube defect. The simulation result (Figure 7.7f) is consistent with the experimental results (Figure 7.7b, 7.7d). We find in the simulation result that although the embryo exhibits an obvious convergent extension, the missing hinge points in the neural plate make it incapable of forming neural folds and the following complete neural tube closure.

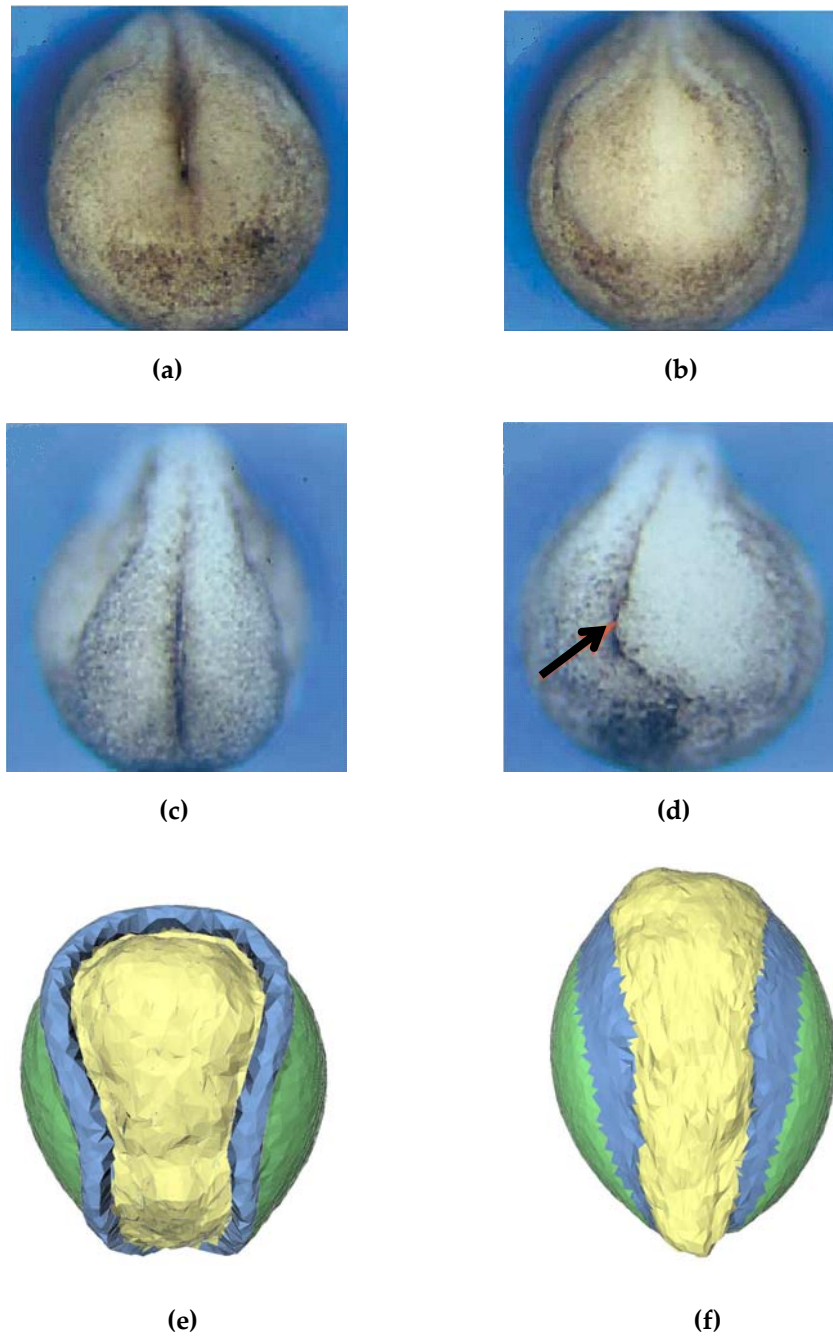


Figure 7.7. Disabling Shroom expression leads to severe neural tube defect. (a) Normal embryo, anterior view. (b) Bilaterally injected embryo displays a total lack of hinge points or anterior neural folds. (c) Normal embryo, anterior view. (d) Embryo injected unilaterally with Xshroom-MO. The hinge point forms normally on the uninjected side (arrow) but is missing on the injected (right) side [Haigo *et al.*, 2003]. (e) The normal embryo neurulation simulation. (f) Simulation result of the disabling shroom expression on the neural plate (Table 7.1 case 4).

## Convergent extension

It is widely understood that Dishevelled (X<sub>dsh</sub>) signaling is required for neural tube closure as well as Shroom expression [Wallingford and Harland, 2002; Ewald *et al.*, 2004]. The morphogenetic movement corresponding to X<sub>dsh</sub> signaling is convergent extension. Existing experiment results prove that the defective convergent extension fails to narrow the midline in the neural plate, and this narrowing is critical to neural tube closure. Figure 7.8 shows the biomechanical contribution of convergent extension to neural tube closure. The blue line represents the distance narrowed by convergent extension. The red line represents the distance narrowed by other biochemical mechanisms. The apical constriction mechanism mentioned above is one of them. Other mechanisms such as the pushing force exerted by the non-neural epidermis are still under debate.

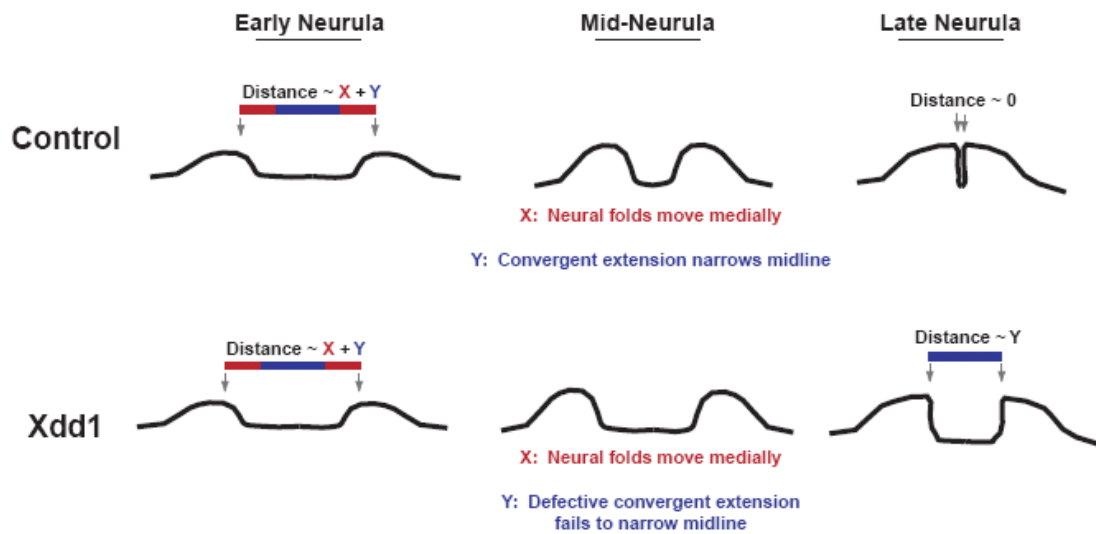


Figure 7.8. Biomechanical contribution of convergent extension to neural tube closure [Wallingford and Harland, 2002].

Severe and mild neural defect [Wallingford and Harland, 2002] caused by convergent extension is illustrated in Figure 7.9. The extent of NTD depends on the amount of X<sub>dd1</sub> mutant injected in the *Xenopus* embryo. A cup-shape of neural folds is formed around the neural plate. The constriction in the neural plate region reacts with the non-neural epidermis tissue to generate this irregular shape. Another typical symptom is the failure of the embryo to extend in a caudal-cephalic direction. The ratio of the length in the caudal-cephalic

direction over the length in the medio-lateral direction remains 1 instead of 1.29 in the real case. A corresponding computational simulation is demonstrated in Figure 7.9c and d (Table 7.1 case 5). Distinctive cup shape neural folds and the failure to extend in the caudal-cephalic direction are observed in simulation results.

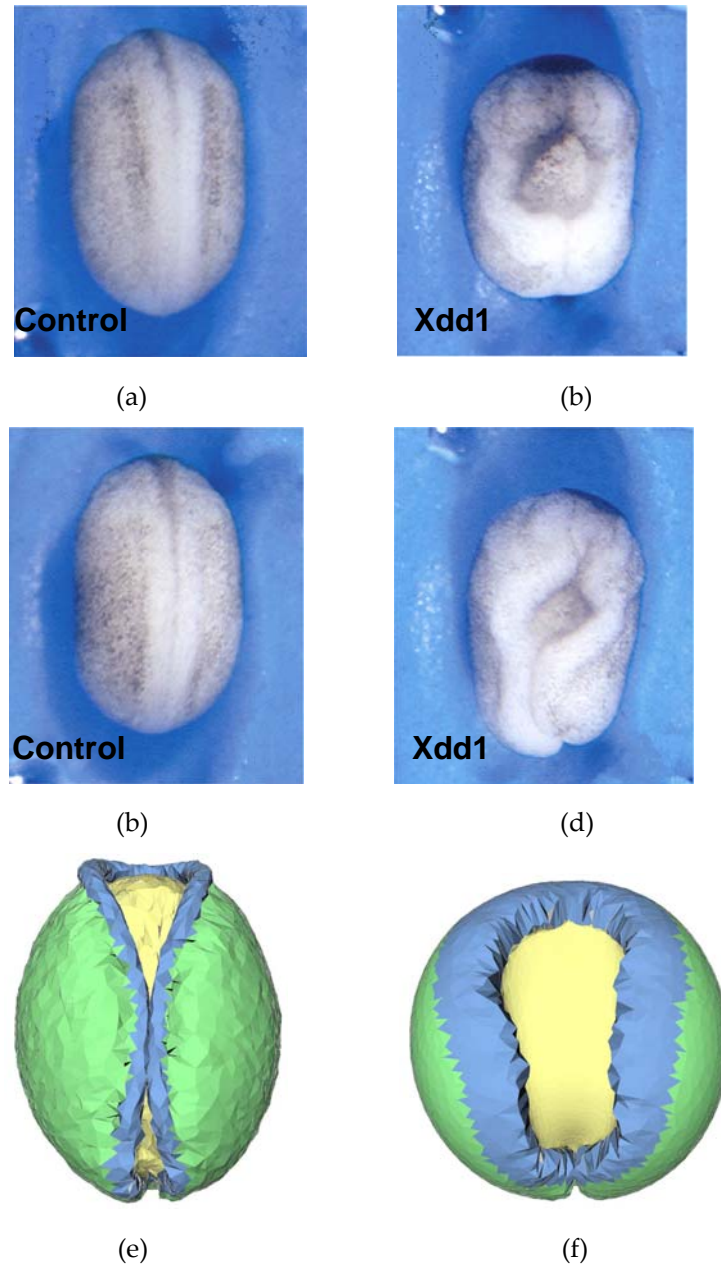


Figure 7.9. Disabling convergent extension leads to severe neural tube defect. (a) Normal embryo. (b) Large amount of Xdd1 injected embryo displays a cup-shape of neural folds. (c) Normal embryo. (d) Small amount of Xdd1 injected embryo displays a cup-shape of neural folds [Wallingford and Harland, 2002]. (e) The normal embryonic neurulation simulation. (f) Simulation result of the disabling convergent extension on the neural plate (Table 7.1 case 5).

The simulations of different defective scenarios discussed above are summarized in the following table.  $\gamma$  and  $\mu$  value are assigned according to this table, and  $L$  represents the lamellipodia effect. Fabric parameters are not included here because the isotropic configuration is adopted as a starting set up. As mentioned in the “apical constriction” section, the Shroom density may vary with its location in the neural plate region. The set up of the  $\gamma$  value becomes a bit more complex than the list in the table. A  $\gamma$  fields may be employed in simulations according to requirements.

**Table 7.1. Comparison of different defective scenarios**

| Regions              |          | Cases   |  | 1.             | 2.                  | 3.                          | 4.                         | 5.                          |
|----------------------|----------|---------|--|----------------|---------------------|-----------------------------|----------------------------|-----------------------------|
|                      |          |         |  | Reference case | Neural plate defect | Non-neural epidermis defect | Apical constriction defect | Convergent extension defect |
| Neural plate         | $\gamma$ | top     |  | 61             | 61                  | 61                          | 9.15                       | 61                          |
|                      |          | bottom  |  | 9.15           | 9.15                | 9.15                        | 9.15                       | 9.15                        |
|                      |          | $\mu$   |  | 0.016          | 0.016               | 0.016                       | 0.016                      | 0.016                       |
|                      |          | $\beta$ |  | 0.0085         | 0.0085              | 0.0085                      | 0.0085                     | 0.0085                      |
|                      |          | $L$     |  | 20             | 20                  | 20                          | 20                         | 0                           |
| Neural folds         | $\gamma$ | top     |  | 0              | 0                   | 0                           | 0                          | 0                           |
|                      |          | bottom  |  | 2              | 2                   | 2                           | 2                          | 2                           |
|                      |          | $\mu$   |  | 0.016          | 0.016               | 0.016                       | 0.016                      | 0.016                       |
|                      |          | $\beta$ |  | 0.0085         | 0.0085              | 0.0085                      | 0.0085                     | 0.0085                      |
|                      |          | $L$     |  | 0              | 0                   | 0                           | 0                          | 0                           |
| Non neural epidermis | $\gamma$ | top     |  | 9.15           | 9.15                | 18.3                        | 9.15                       | 9.15                        |
|                      |          | bottom  |  | 9.15           | 9.15                | 18.3                        | 9.15                       | 9.15                        |
|                      |          | $\mu$   |  | 0.016          | 0.016               | 0.016                       | 0.016                      | 0.016                       |
|                      |          | $\beta$ |  | 0.0085         | 0.0085              | 0.0085                      | 0.0085                     | 0.0085                      |
|                      |          | $L$     |  | 0              | 0                   | 0                           | 0                          | 0                           |

Note: unit for  $\gamma$  is nN, unit for  $\mu$  is nN min /  $\mu\text{m}^2$  and unit for  $\beta$  is  $\mu\text{m}^{-2}$ .  $L$  represents the lamellipodium effect in the midline of neural plate

### 7.3 Biomechanical feedbacks

Positive feedbacks and negative feedback are widely recognized in genetic regulatory networks and some of them have biomechanical counterparts. The studies carried out by Belousov have provided insights into the importance of the positive feedbacks and negative feedbacks in the embryonic developmental morphodynamics. The experiments [Belousov, 2006] describe an interesting phenomenon in embryo development. During the gastrulation stage, stretching a piece of tissue from the blastocoel roof leads to the increase of tension in this tissue. And the tension tends to be restored to its initial value by cell deformation and intercalation. When the tension is restored to its initial value, the cell deformation and intercalation does not stop, and the stress in this piece of tissue may be reduced to zero, and even to compression stress. Belousov calls this phenomenon “hyper-restoration” (HR) and provides some empirical evidences of HR reactions from the multi-cellular level and the individual cell level [Belousov, 2006].

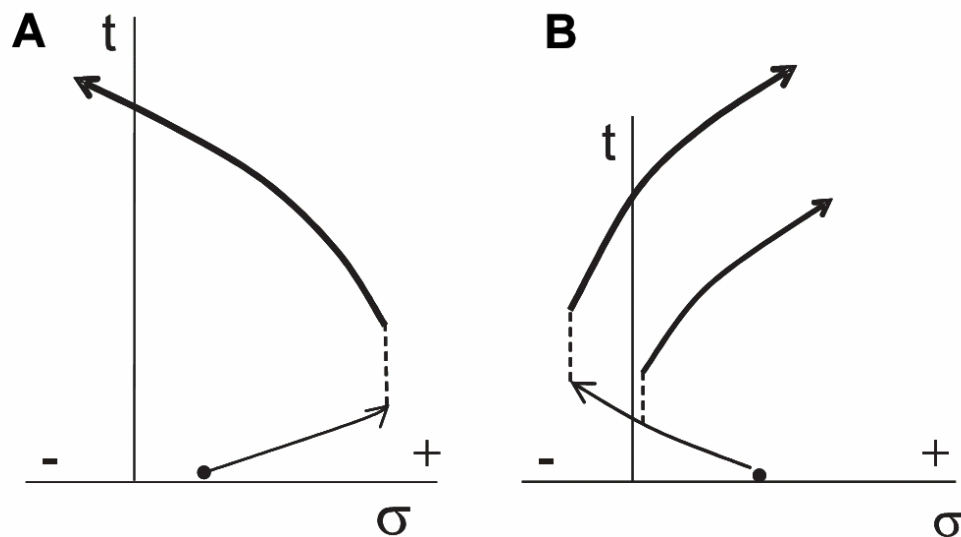


Figure 7.10. Schemes of hyper-restoration responses to the shifts of mechanical stresses from the initial values denoted by black spots [Belousov, 2006]. Fine lines indicate the stress in the tissue generated by external forces, stretching (A) and compression (B). Solid lines represent the stress restoration process. Note that the solid lines pass initial values and the stress is over restored. The vertical dashed lines represent lag periods between the stabilization of an external force and the start of an active response to it. Horizontal axes are stress, and vertical axes are time.

In Belousov's paper, hyper-restoration reactions can be coupled to generate positive feedbacks such as contraction-extension (CE) feedback. Figure 7.11a is a piece of tissue with different mechanical properties in the  $\alpha$  area and  $\beta$  area. Part  $\alpha$  actively contracts, thus part  $\beta$  is passively stretched. The hyper-restoration reactions happen in part  $\beta$  and the tissue over extends to give part  $\alpha$  compression in the vertical direction. This will drive hyper-extension to happen in part  $\alpha$ . This loop can occur several times and generate the tissue shape as demonstrated in Figure 7.11c.

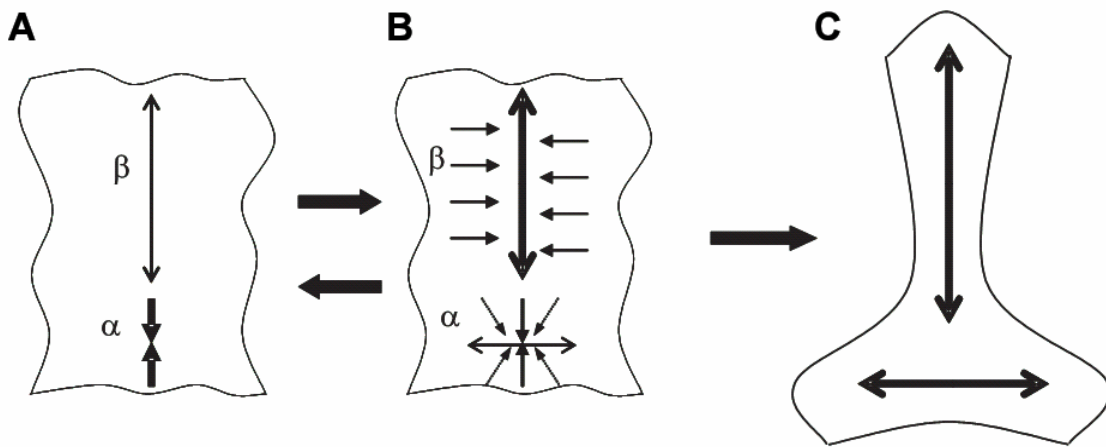


Figure 7.11. A scheme of contraction-extension (CE) feedback [Belousov, 2006].

The hyper-restoration theory and CE feedback example in the gastrulation process drive us to ponder if there is any evidence showing its existence in the neurulation process. As mentioned above, the neural tube closure depends on apical constriction, convergent extension, and other mechanisms [Kiehart *et al.*, 2000]. In Wallingford's paper, a hypothesis is proposed concerning non-neural epidermis generating pushing force on neural folds and contributing to their closure. There are a couple of other experimental results supporting this hypothesis. Holland argues that the non-neural epidermis is actually neural [Holland, 2005] which indicates that non-neural epidermis is patterned anteriorly and posteriorly by some mechanisms. Jacobson's experiments [Burnside and Jacobson, 1968; Jacobson, 1973; Karfunkel, 1974], excision of ectodermal strips within and outside the neural plate,

pioneered the research field of morphogenetic movements during neural tube closure in amphibians. His results indicate that the non-neural epidermis can move towards neural plate midline even if the tissue between neural folds and non-neural epidermis is excised. Schoenwolf did experiments similar to Jacobson [Lawson *et al.*, 2001; Brouns *et al.*, 2005], and the results provide direct evidence that the non-neural epidermis is essential for normal folding of the neural plate. Our image capturing results of the movements of non-neural epidermis indicate that there are strong cell intercalations occurring in those areas. In addition, the Axolotl embryo stress resultant summary in Table 7.2 [Benko and Brodland, 2007] exhibit an abnormal phenomenon, the stress resultant in the cephalic-caudal direction is larger than the one in the medio-lateral direction. Considering the CE happening in the neural plate which demonstrates strong anisotropic tendencies of measurements made on the dorsal aspect regions of stage 13 and 15 embryos, there should be a relaxation for stress resultant in cephalic-caudal direction in the non-neural epidermis region. Thus an opposite answer should be obtained. This could be an evidence for a weak CE occurring in non-neural epidermis regions.

Connecting these clues and experiment results with hyper-restoration theory and CE feedback, we arrive at the following hypothesis: the convergent extension in the neural plate may cause a corresponding weak convergent extension in the non-neural epidermis as demonstrated in Bloussov's CE feedback example. The direction of the convergent extension in the non-neural epidermis region is demonstrated in Figure 7.3. To test our hypothesis, we run the simulations of two cases, with CE feedback and without CE feedback on the non-neural epidermis. In the simulation, the CE in the neural plate induces the occurring of CE in the non-neural epidermis. The positive feedback mechanism is implemented by increasing the effect of CE in the non-neural epidermis with the reduction of the length of the midline in the non-neural epidermis (the bold line in Figure 7.12a). The simulation results are illustrated in Figure 7.12. The side view and dorsal view of simulation results in both cases (Figure 7.12) indicate that the convergent extension in the non-neural epidermis region is capable of generating more realistic geometry and they can be illustrated as follows:

1. The ratio of the length in the caudal-cephalic direction over the length in the medio-lateral direction is 1.28, which is very close to the real cases (Figure 7.12e).
2. The curvature of the midline of the non-neural epidermis (the bold line in Figure 7.12a) in the “with CE feedback” case is less than the “without CE feedback” case. This is more consistent with the real case.
3. From stage 14 to 16, the length of the midline of the neural plate increases in both cases while the length reduction of the midline of the non-neural epidermis in the “with CE feedback” case is larger than the “without CE feedback” case (Figure 7.12a, b). In real embryonic development, the midline of the non-neural epidermis experiences a large reduction which cannot be explained by the simulation result of the case “without CE feedback” (Figure 7.12b and 7.12f). There must be some other mechanism occurring to reduce the midline length. The simulation result of the case “with CE feedback” yields a proper shape resembling the real case.

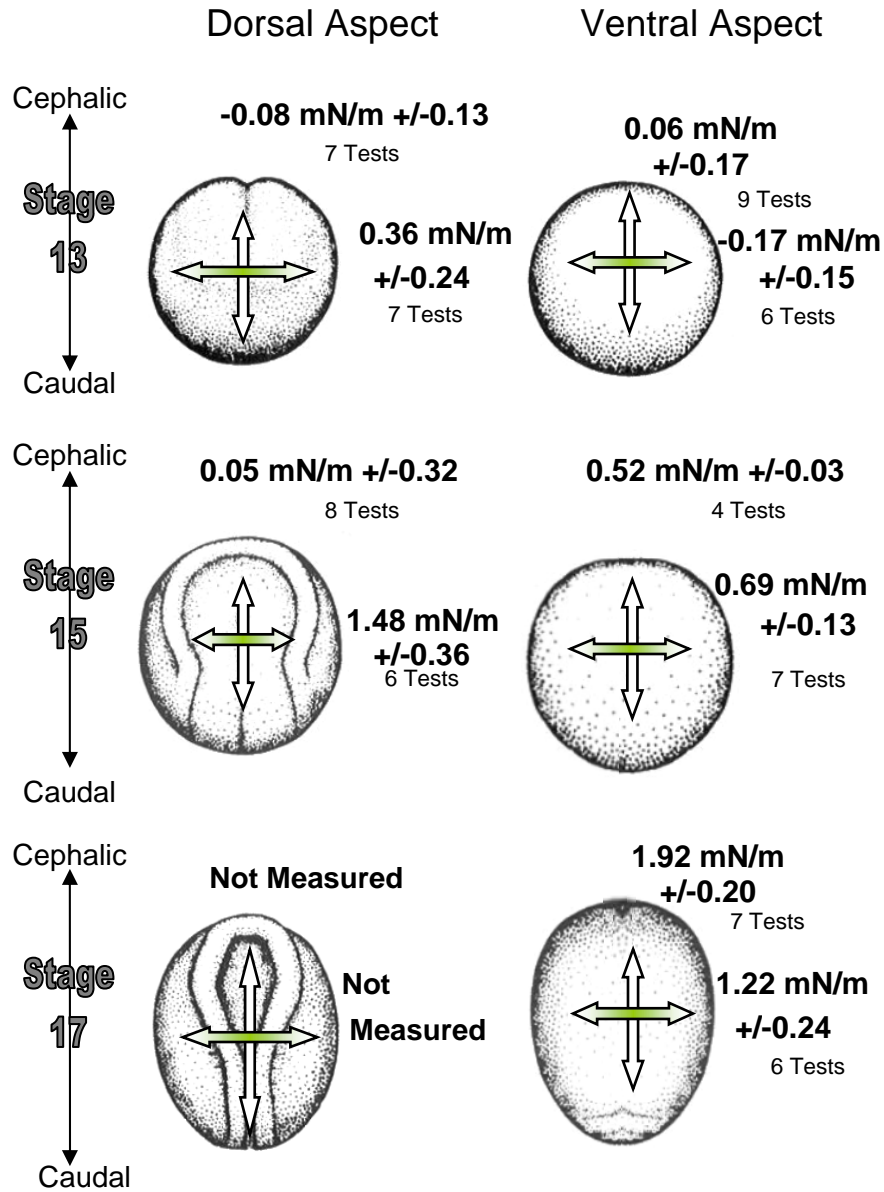
The simulations presented here can have following interpretations:

1. Apical constriction (Shroom) and convergent extension (Xdsh) have a strong tendency to produce neural tube closure. Any failure of these two mechanisms may cause severe NTD. Other mechanisms under research may still be found to affect neural tube closure; however, from a mechanical perspective, these two mechanisms seem to be the main contributors to neural tube closure.
2. Boundary conditions and mechanical properties have a great effect on embryonic development. Even small perturbations of those factors, which are magnified during the embryonic development, may cause a severe NTD. These evidences suggest that the cause of spina bifida may exist in the wrong mechanical properties of embryos and the wrong boundary value of embryonic environment. The mechanics play an important role in embryonic development. Comprehensive knowledge database and strictly monitoring the development of embryonic geometry and mechanical properties could be a future solution to the prevention of NTD.
3. Positive and negative feedbacks in the genetic network may have their biomechanical counterparts [Taber, 2007]. Because neural tube closure and

embryonic morphogenesis are strongly influenced by mechanics, the mechanical model provides us with a platform to speculate and propose different biomechanical feedbacks. This assists scientists to focus on interesting areas and finding the corresponding biochemical feedbacks. For instance, the fact that the hypothesis of convergent extension acting in non-neural epidermis makes our simulation results closer to the real case can inspire scientists to discover if there is any biochemical pathway related to this mechanical phenomenon.

4. Biomechanical feedbacks bring complexity into the whole model. The initial defects in configuration or mechanical properties may be magnified by these feedbacks and cause severe consequences. Therefore, to capture the essence of embryonic development, biomechanical feedbacks become extremely important.

Table 7.2. Stage 13, 15, 17 stress resultant summary (Modified from Bordzilovskaya and Dettlaff, 1979). The arrows represent the direction of stress resultant.



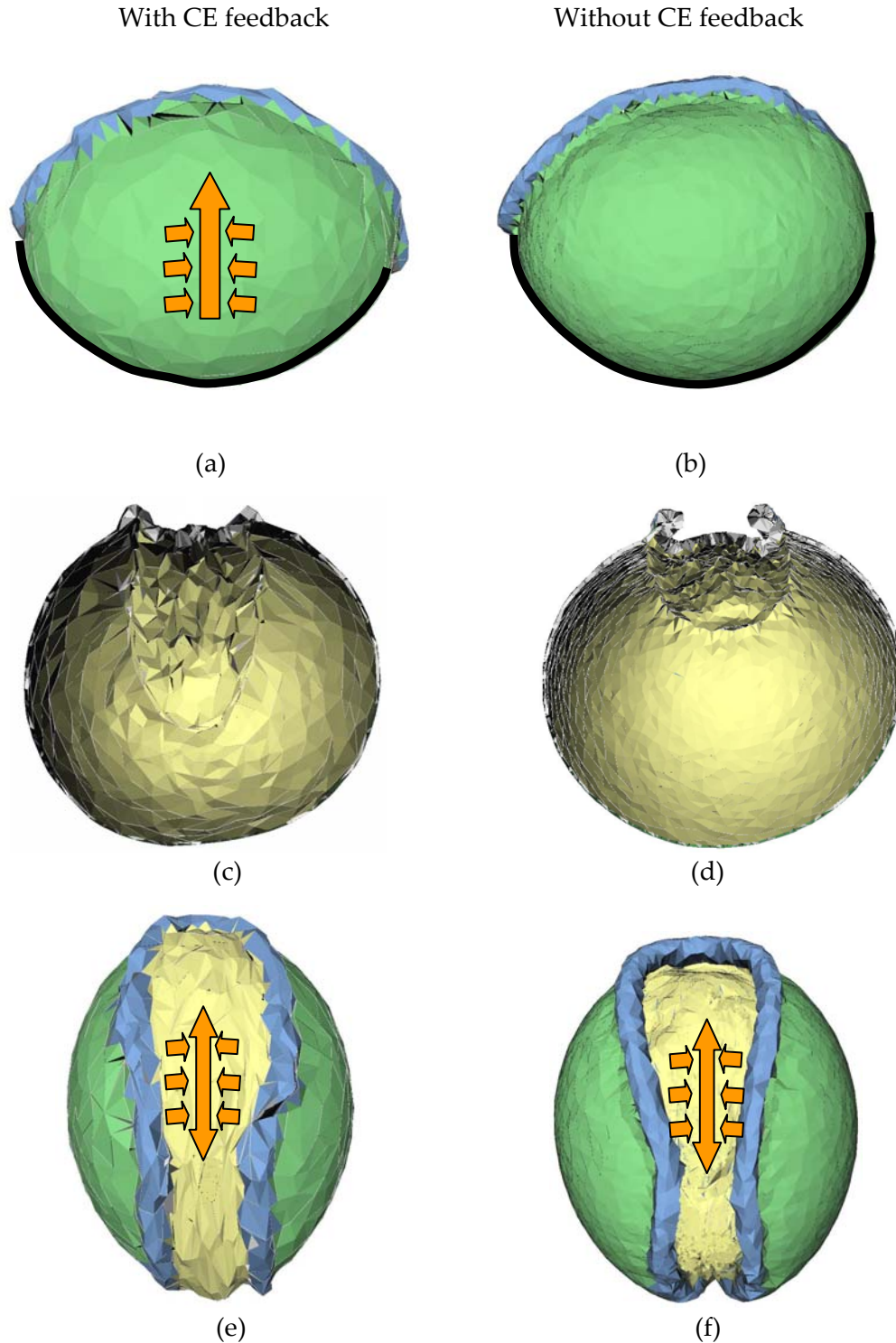


Figure 7.12. With and without CE feedback on non-neural epidermis. (a) The side view of “with CE feedback” simulation at stage 15. (b) The side view of “without CE feedback” simulation at stage 15 (Bold line represents non neural epidermis midline). (c) The cross section of “with CE feedback” simulation at stage 15. (d) The cross section of “without CE feedback” simulation at stage 15. (e) The dorsal view of “with CE feedback” simulation at stage 15. (f) The dorsal view of “without CE feedback” simulation at stage 15. (Large up-down arrows represent the CE direction)

## Chapter 8

# Discussions and Future work

The finite element simulation presented here is the first published whole-embryo model of neurulation. In time, it will be refined, as were its 2D predecessors, so that differences between the model and real embryos can be eliminated. The process of resolving these differences is an important scientific task because through it, deficits in understanding can be identified and relevant new experiments conceived.

The model demonstrates that realistic tissue motions are possible when a suitable cell-based constitutive equation is used. A key feature of the current constitutive model is that cells are able to flow past each other in-plane, a characteristic known to be important in real embryos. In previous (unpublished) attempts to model neurulation in 3D, cells were not free to rearrange in plane. This deficiency caused the tissues to be excessively stiff, especially with respect to in-plane shear, and it impeded the complex 3D deformations that must occur near the ends of the neural plate region. The present constitutive equation also made it possible for single finite elements to model multiple cells, making whole-embryo models computationally practical.

Recent experiments have shown that, during development, the fabric of the embryonic epithelia varies substantially with tissue type, location, and development stage. The constitutive model used here is able to successfully predict the fabric evolution during *in vitro* tests, but additional statistical analysis software must be written before the accuracy of

those predictions can be assessed in the context of neurulation. Such comparisons, however, are important to full model validation.

The constitutive model is structured so that, as the biochemical pathways involved in tissue regulation are identified, their effects can be incorporated into the model. The model can hence serve as a bridge between gene expression and the morphogenetic movements of critical developmental events. This important integration of biology and mechanics is possible because the finite element method provides an open computational framework.

Simulations conducted to date show that tissue motions are highly sensitive to tissue mechanical properties. This finding suggests that spina bifida and other neural tube defects might arise through a variety of subtle mechanical means. It also suggests that modest interventions might be sufficient to prevent neural tube defects. Identifying appropriate intervention methods is a critical goal for additional research, and the finite element model presented here holds promise as the means to carry out preliminary evaluations of proposed interventions.

A hypothesis about a CE feedback occurring in non-neural epidermis has been discussed in detail with biological experiments and computational simulations. Although it still needs more solid support from biologists, the approach of inferring biochemical positive feedbacks from their biomechanical counterparts can assist scientists to discover new mechanisms.

With the comparisons between thousands of simulations and experimental data, the finite element implementation has proven to be effective and reliable. However, a number of issues need more attention in future work. The Pentahedral element used in the model sometimes experienced over-twisted motions, which caused volume constraints to fail. A more robust replacement needs to be developed. The meshless numerical method for irregular evolving grids can be a good candidate [Braun and Sambridge, 1995; Sukumar *et al.*, 1998]. Considering the computation scale, a simplified contact algorithm is employed in this model. However, as a multilayer model is developed, a more complex contact algorithm needs to be incorporated into the model to make the computation accurate and reliable. Tensor representations, which have been proven successful for describing fabric in a

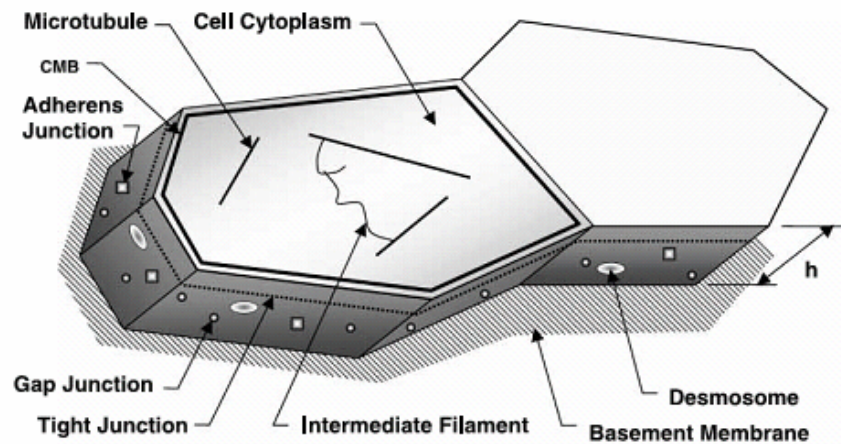
number of micromechanical applications [Rothenburg, 1981], should be included in the constitutive model. In addition, more materials can be developed based on the biological experiments and employed in the future simulations.

# Appendix A

## Assembly of the Matrix Equations

In Denis and Brodland's model, the key assumptions can be summarized as follow:

1. The net driving force in cell-cell interactions is approximated by an interfacial tension along each of the cell boundaries. The tension is generated by circumferential microfilament bundles (CMBs), other microfilaments and cell membrane tension. Forces generated by cell adhesion molecules (CAMs) reduce this contraction.
2. The cell cytoplasm, including its embedded networks of intermediate filaments, is considered to be incompressible and is modeled by an effective viscosity  $\mu$ .



(a)

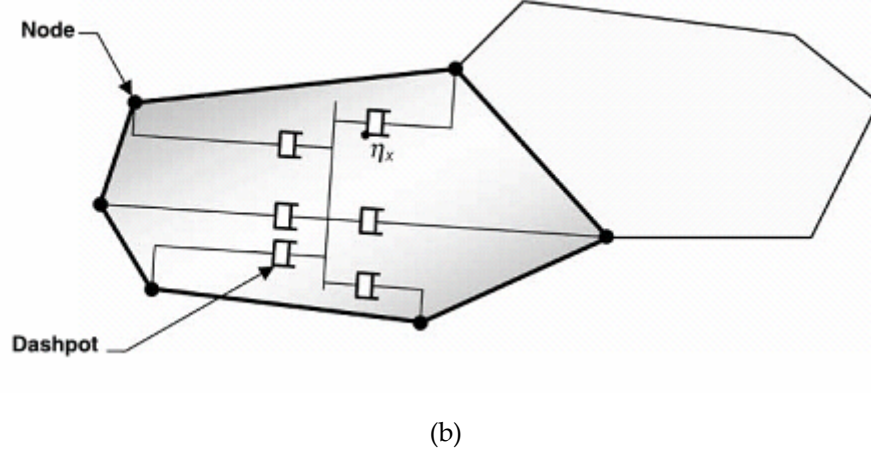


Figure A.1. The cell and finite element models [Brodland *et al.*, 2007]. (a) A schematic representation of two cells that are assumed to form part of a generic embryonic epithelium. (b) A model based on systems of orthogonal dashpots. In the interest of image clarity, only the dashpots aligned with the long axis of the cell are shown. The second set of dashpots would run orthogonal to those shown. Truss elements, like those shown in (a), are assumed to act along each cell-cell interface.

Based on the above assumptions, there are a total of two free material parameters in this model: a constant tension  $\gamma$  along each cell-cell interface and the cell viscosity  $\mu$ . To model this viscosity in the finite element method, nodes of each cell are connected with each other by an orthogonal dashpot system which is along with the principal axes of the cell (Figure A.1b). The introduction of the orthogonal dashpot system into the model overcomes the locking challenge that was present in the previous model. In the previous model, cells with  $n$  sides are divided into  $n$  triangular elements. The constitutive equation is expressed as,

$$\begin{bmatrix} \sigma_{xx} \\ \sigma_{yy} \\ \sigma_{zz} \\ \tau_{xy} \\ \tau_{yz} \\ \tau_{xz} \end{bmatrix} = \begin{bmatrix} -p \\ -p \\ -p \\ 0 \\ 0 \\ 0 \end{bmatrix} + \begin{bmatrix} \frac{4}{3}\mu & -\frac{2}{3}\mu & -\frac{2}{3}\mu & 0 & 0 & 0 \\ -\frac{2}{3}\mu & \frac{4}{3}\mu & -\frac{2}{3}\mu & 0 & 0 & 0 \\ -\frac{2}{3}\mu & -\frac{2}{3}\mu & \frac{4}{3}\mu & 0 & 0 & 0 \\ 0 & 0 & 0 & 2\mu & 0 & 0 \\ 0 & 0 & 0 & 0 & 2\mu & 0 \\ 0 & 0 & 0 & 0 & 0 & 2\mu \end{bmatrix} \cdot \begin{bmatrix} \dot{\epsilon}_{xx} \\ \dot{\epsilon}_{yy} \\ \dot{\epsilon}_{zz} \\ \dot{\epsilon}_{xy} \\ \dot{\epsilon}_{yz} \\ \dot{\epsilon}_{xz} \end{bmatrix}. \quad (\text{A.1})$$

If a fluid is incompressible, then  $\dot{\epsilon}_{kk} = \dot{\epsilon}_{xx} + \dot{\epsilon}_{yy} + \dot{\epsilon}_{zz} = 0$ . By integration, we are able to assemble the stiffness matrix based on this constitutive equation. The phenomenon that the

cytoplasm in a cell can move freely can be modeled by setting Poisson's ratio to zero in each triangle element and imposing a volume constrain on each cell. The locking problem arises because, as the edge of a cell shortens, the stiffness of any triangles adjoining that edge increases without bound because their strain rates tend to infinity.

To circumvent this problem, each dashpot in Figure A.1b is assigned the same damping coefficient  $\eta_x$ . The dashpots in the orthogonal direction are not shown in the Figure A.1b and we assume its damping coefficient is  $\eta_x$ . As a consequence, the movement of one node will produce the same reaction force on the other nodes (assuming they are fixed when the movement occurs). This brings simplicity to the stiffness matrix assembling. And through virtual work principle,  $\eta_x$  and  $\eta_y$  can be related to the cell viscosity  $\mu$  based on some geometric assumptions [Brodland *et al.*, 2007].

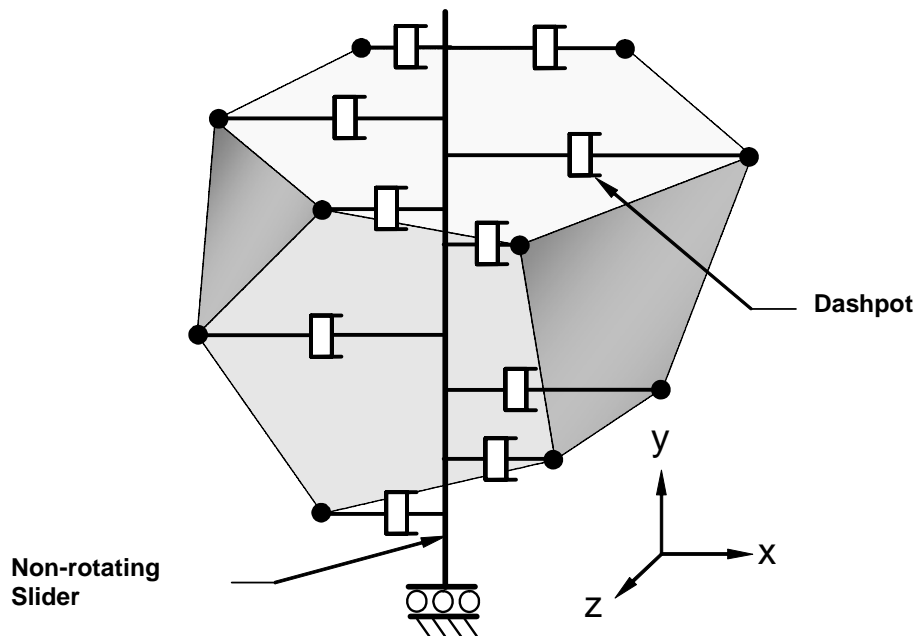


Figure A.2. System of Orthogonal Dashpots [Brodland *et al.*, 2007].

To calculate the stiffness of the dashpots for a 3D cell, an ellipsoid is fit to the cell to determine the orientation of its three principle axes and the length of those axes (Figure A.2). The products of inertia of the cell are calculated in Cartesian space and then assembled into a matrix. The matrix is illustrated in Figure A.3.

|          |          |          |
|----------|----------|----------|
| $I_{xx}$ | $I_{xy}$ | $I_{xz}$ |
| $I_{yx}$ | $I_{yy}$ | $I_{yz}$ |
| $I_{zx}$ | $I_{zy}$ | $I_{zz}$ |

Figure A.3. Location of products of inertia in the matrix

The moments of inertia are calculated based on the following equations,

$$I_{xx} = \sum_{i=1}^n V \times \Delta x^2 , \quad (\text{A.2})$$

$$I_{xy} = I_{yx} = \sum_{i=1}^n V \times \Delta x \times \Delta y , \quad (\text{A.3})$$

$$I_{xz} = I_{zx} = \sum_{i=1}^n V \times \Delta x \times \Delta z , \quad (\text{A.4})$$

$$I_{yy} = \sum_{i=1}^n V \times \Delta y^2 , \quad (\text{A.5})$$

$$I_{yz} = I_{zy} = \sum_{i=1}^n V \times \Delta y \times \Delta z , \quad (\text{A.6})$$

$$I_{zz} = \sum_{i=1}^n V \times \Delta z^2 , \quad (\text{A.7})$$

where V represents the volume of the cell;  $\Delta x$ ,  $\Delta y$ , and  $\Delta z$  are the x, y and z distances from the centroid of the tetrahedron (constructed by connecting the triangular sub-faces with the centroid of the cell) to the centroid of the cell respectively and n is the number of the tetrahedrons that make up a cell.

Through a great number of computational simulations, an empirical formulation to relate the eigenvalues of the matrix to the length of the three principle axes of the ellipsoid is expressed as,

$$AxisLength = \sqrt{\frac{EigenValue}{Volume}} \times 6.63 \quad (A.8)$$

Then the dashpots along each of the principle axes are formulated by the following equations:

$$\mu_A = \frac{g\mu BC}{nA}, \quad (A.9)$$

$$\mu_B = \frac{g\mu AC}{nB}, \quad (A.10)$$

$$\mu_C = \frac{g\mu AB}{nC}, \quad (A.11)$$

where the A, B, C represent the length in the three principle axes, n is the number of nodes in the cell and g is a form factor with the value of 17.7.

Truss-like elements are employed to model the interfacial tension along the each side of the cell. To keep the total cell volume constant, a volume boundary constraint is imposed on each cell. The system is described by the equation:

$$\frac{1}{\Delta t} \mathbf{C}(\mathbf{u}_{q+1} - \mathbf{u}_q) = \mathbf{f}_q \quad (A.12)$$

$$\mathbf{C} = \sum_{k=1}^m \mathbf{C}^k \quad (A.13)$$

where  $m$  is the number of 3D cell elements in the cell mass, and  $\mathbf{C}^k$  is the damping matrix of cell element  $k$ . The elements in the matrix can be calculated as follows.

$$\mathbf{C}_{3i,3j}^k = \begin{cases} -\mu_A & \text{if } i \neq j \\ n\mu_A & \text{if } i = j' \end{cases} \quad (A.14)$$

$$\mathbf{C}_{3i+1,3j+1}^k = \begin{cases} -\mu_B & \text{if } i \neq j \\ n\mu_B & \text{if } i = j' \end{cases} \quad (A.15)$$

$$\mathbf{C}_{3i+2,3j+2}^k = \begin{cases} -\mu_C & \text{if } i \neq j \\ n\mu_C & \text{if } i = j' \end{cases} \quad (A.16)$$

The damping matrix associated with cytoplasm is updated with each time step.

# References

- Adams, C.L., and Nelson, W.J. (1998). Cytomechanics of cadherin-mediated cell-cell adhesion. *Curr. Opin. Cell Biol.* 10, 572-577.
- Alberts, B. (1998). *Essential Cell Biology: An Introduction to the Molecular Biology of the Cell* (New York: Garland).
- Almkvist, G., and Berndt, B. (1988). Gauss, Landen, Ramanujan, the Arithmetic-Geometric Mean, Ellipses,  $\pi$ , and the Ladies Diary. *The American Mathematical Monthly* 95, 585-608.
- Asipauskas, M., Aubouy, M., Glazier, J.A., Graner, F., and Jiang, Y. (2003). A texture tensor to quantify deformations: the example of two-dimensional flowing foams. *Granular Matter* 5, 71-74.
- Bao, G., and Suresh, S. (2003). Cell and molecular mechanics of biological materials. *Nat. Mater.* 2, 715-725.
- Beadle, G.W., and Tatum, E.L. (1941). Genetic Control of Biochemical Reactions in *Neurospora*. *Proc. Natl. Acad. Sci. U. S. A.* 27, 499-506.
- Belousov, L.V. (1998). *The Dynamic Architecture of a Developing Organism: an interdisciplinary approach to the development of organisms* (New York: Springer).
- Belousov, L.V., and Grabovsky, V.I. (2006). Morphomechanics: goals, basic experiments and models. *Int. J. Dev. Biol.* 50, 81-92.
- Belousov, L.V., Lakirev, A.V., Naumidi, I.I., and Novoselov, V.V. (1990). Effects of relaxation of mechanical tensions upon the early morphogenesis of *Xenopus laevis* embryos. *Int. J. Dev. Biol.* 34, 409-419.
- Belousov, L.V., Luchinskaya, N.N., Ermakov, A.S., and Glagoleva, N.S. (2006). Gastrulation in amphibian embryos, regarded as a succession of biomechanical feedback events. *Int. J. Dev. Biol.* 50, 113-122.
- Benko, R., and Brodland, G.W. (2007). Measurement of in vivo Stress Resultants in Neurulation-stage Amphibian Embryos. *Ann. Biomed. Eng.* 35, 672-681.

- Bjorklund, N.K., and Gordon, R. (2006). A hypothesis linking low folate intake to neural tube defects due to failure of post-translation methylations of the cytoskeleton. *Int. J. Dev. Biol.* 50, 135-141.
- Bootsma, G. (2003). Spatial data correlation. Cive 701 course project. Department of Civil Engineering, University of Waterloo.
- Borkhvardt, V.G. (2002). Invagination and Evagination: A Hydromechanical Model. *Russian Journal of Developmental Biology* 33, 13-21.
- Braga, V. (2000). The crossroads between cell-cell adhesion and motility. *Nat. Cell Biol.* 2, E182-4.
- Braun, J., and Sambridge, M. (1995). A numerical method for solving partial differential equations on highly irregular evolving grids. *Nature* 376, 655-660.
- Brodland, G.W. (2004). Computational modeling of cell sorting, tissue engulfment, and related phenomena: A review. *Appl. Mech. Rev.* 57, 47.
- Brodland, G.W. (2003). New information from cell aggregate compression tests and its implications for theories of cell sorting. *Biorheology* 40, 273-277.
- Brodland, G.W., and Chen, H.H. (2000). The mechanics of cell sorting and envelopment. *J. Biomech.* 33, 845-851.
- Brodland, G.W., and Clausi, D.A. (1995). Cytoskeletal mechanics of neurulation: insights obtained from computer simulations. *Biochem. Cell Biol.* 73, 545-553.
- Brodland, G.W., and Clausi, D.A. (1994). Embryonic tissue morphogenesis modeled by FEM. *J. Biomech. Eng.* 116, 146-155.
- Brodland, G.W., and Gordon, R. (1990). Intermediate filaments may prevent buckling of compressively loaded microtubules. *J. Biomech. Eng.* 112, 319-321.
- Brodland, G.W., and Veldhuis, J.H. (2002). Computer simulations of mitosis and interdependencies between mitosis orientation, cell shape and epithelia reshaping. *J. Biomech.* 35, 673-681.
- Brodland, G.W., and Veldhuis, J.H. (1998). Three-dimensional reconstruction of live embryos using robotic microscope images. *IEEE Trans. Biomed. Eng.* 45, 1173-1181.

- Brodland, G.W., Viens, D., and Veldhuis, J.H. (2007). A new cell-based FE model for the mechanics of embryonic epithelia. *Computer Methods in Biomechanics & Biomedical Engineering* 10, 121-128.
- Brodland, G.W., and Wiebe, C.J. (2004). Mechanical effects of cell anisotropy on epithelia. *Comput. Methods Biomech. Biomed. Engin.* 7, 91-99.
- Brouns, M.R., Afman, L.A., Vanhauten, B.A., Hekking, J.W., Kohler, E.S., and van Straaten, H.W. (2005). Morphogenetic movements during cranial neural tube closure in the chick embryo and the effect of homocysteine. *Anat. Embryol. (Berl)* 210, 81-90.
- Brun, R.B., and Garson, J.A. (1983). Neurulation in the Mexican salamander (*Ambystoma mexicanum*): a drug study and cell shape analysis of the epidermis and the neural plate. *J. Embryol. Exp. Morphol.* 74, 275-295.
- Burnside, B. (1973). Microtubules and Microfilaments in Amphibian Neurulation. *Integrative and Comparative Biology* 13, 989.
- Burnside, M.B., and Jacobson, A.G. (1968). Analysis of morphogenetic movements in the neural plate of the newt *Taricha torosa*. *Dev. Biol.* 18, 537-552.
- Carter, M., Chen, X., Slowinska, B., Minnerath, S., Glickstein, S., Shi, L., Campagne, F., Weinstein, H., and Ross, M.E. (2005). Crooked tail (Cd) model of human folate-responsive neural tube defects is mutated in Wnt coreceptor lipoprotein receptor-related protein 6. *PNAS* 102, 12843-12848.
- Chen, C.S., Tan, J., and Tien, J. (2004). Mechanotransduction at cell-matrix and cell-cell contacts. *Annu. Rev. Biomed. Eng.* 6, 275-302.
- Chen, H.H., and Brodland, G.W. (2000). Cell-level finite element studies of viscous cells in planar aggregates. *J. Biomech. Eng.* 122, 394-401.
- Cherdantsev, V.G. (2006). The dynamic geometry of mass cell movements in animal morphogenesis. *Int. J. Dev. Biol.* 50, 169-182.
- Chin, K., Kurian, R., and Saunders, J.C. (1997). Maturation of tympanic membrane layers and collagen in the embryonic and post-hatch chick (*Gallus domesticus*). *J. Morphol.* 233, 257-266.
- Clausi, D.A., and Brodland, G.W. (1993). Mechanical evaluation of theories of neurulation using computer simulations. *Development* 118, 1013-1023.

- Cummings, F.W. (1989). On surface geometry coupled to morphogen. *J. Theor. Biol.* 137, 215-219.
- Davidson, E.H., Rast, J.P., Oliveri, P., Ransick, A., Calestani, C., Yuh, C.H., Minokawa, T., Amore, G., Hinman, V., and Arenas-Mena, C. (2002). A Genomic Regulatory Network for Development. *Science's STKE* 295, 1669.
- Discher, D.E., Janmey, P., and Wang, Y.L. (2005). Tissue cells feel and respond to the stiffness of their substrate. *Science* 310, 1139-1143.
- du Roure, O., Saez, A., Buguin, A., Austin, R.H., Chavrier, P., Silberzan, P., and Ladoux, B. (2005). Force mapping in epithelial cell migration. *Proc. Natl. Acad. Sci. U. S. A.* 102, 2390-2395.
- Edelman, G.M. (1988). *Topobiology: An Introduction to Molecular Embryology* (New York: Basic Books).
- Ehrlich, J.S., Hansen, M.D., and Nelson, W.J. (2002). Spatio-temporal regulation of Rac1 localization and lamellipodia dynamics during epithelial cell-cell adhesion. *Dev. Cell.* 3, 259-270.
- Ewald, A.J., Peyrot, S.M., Tyszka, J.M., Fraser, S.E., and Wallingford, J.B. (2004). Regional requirements for Dishevelled signaling during *Xenopus* gastrulation: separable effects on blastopore closure, mesendoderm internalization and archenteron formation. *Development* 131, 6195-6209.
- Kakal, F. (2007). *Neural Tube Defects Causing Teratogens Affect Material Properties and Cytoskeletal Structures of Neurulating Axolotl Embryos*. Master's thesis. University of Waterloo.
- Flügge, W. (1973). *Stress in shells* (Berlin and New York: SpringerVerlag).
- Forgács, G. (2005). *Biological Physics of the Developing Embryo* (Cambridge: Cambridge University Press).
- Fristrom, D. (1988). The cellular basis of epithelial morphogenesis. A review. *Tissue Cell* 20, 645-690.
- Fung, Y. (1993). *Biomechanics: Mechanical Properties of Living Tissues* (Springer).
- Gardel, M.L., Nakamura, F., Hartwig, J.H., Crocker, J.C., Stossel, T.P., and Weitz, D.A. (2006). Prestressed F-actin networks cross-linked by hinged filamins replicate mechanical properties of cells. *PNAS* 103, 1762-1767.

- Gere, J.M., and Timoshenko, S.P. (2001). *Mechanics of materials* Brooks/Cole Pacific Grove, CA).
- Gilbert, S.F. (2000). *Developmental biology* (Sinauer Associates Sunderland, Mass).
- Glazier, J.A., and Graner, F. (1993). Simulation of the differential adhesion driven rearrangement of biological cells. *Physical Review E* 47, 2128-2154.
- Gloushankova, N.A., Alieva, N.A., Krendel, M.F., Bonder, E.M., Feder, H.H., Vasiliev, J.M., and Gelfand, I.M. (1997). Cell-cell contact changes the dynamics of lamellar activity in nontransformed epitheliocytes but not in their ras-transformed descendants. *Proc. Natl. Acad. Sci. U. S. A.* 94, 879-883.
- Gloushankova, N.A., Krendel, M.F., Alieva, N.O., Bonder, E.M., Feder, H.H., Vasiliev, J.M., and Gelfand, I.M. (1998). Dynamics of contacts between lamellae of fibroblasts: essential role of the actin cytoskeleton. *Proc. Natl. Acad. Sci. U. S. A.* 95, 4362-4367.
- Goel, N., Campbell, R.D., Gordon, R., Rosen, R., Martinez, H., and Ycas, M. (1970). Self-sorting of isotropic cells. *J. Theor. Biol.* 28, 423-468.
- Goel, N.S., and Rogers, G. (1978). Computer simulation of engulfment and other movements of embryonic tissues. *J. Theor. Biol.* 71, 103-140.
- Gordon, R., and Brodland, G. (1987). The cytoskeletal mechanics of brain morphogenesis. Cell state splitters cause primary neural induction. *Cell Biophys.* 11, 177-238.
- Gordon, R., Goel, N.S., Steinberg, M.S., and Wiseman, L.L. (1972). A rheological mechanism sufficient to explain the kinetics of cell sorting. *J. Theor. Biol.* 37, 43-73.
- Gordon, R., and Jacobson, A. (1978). The shaping of tissues in embryos. *Sci. Am.* 238, 106-113.
- Graner, F., and Glazier, J.A. (1992). Simulation of biological cell sorting using a two-dimensional extended Potts model. *Phys. Rev. Lett.* 69, 2013-2016.
- Gumbiner, B.M. (1996). Cell adhesion: the molecular basis of tissue architecture and morphogenesis. *Cell* 84, 345-357.
- Haigo, S.L., Hildebrand, J.D., Harland, R.M., and Wallingford, J.B. (2003). Shroom induces apical constriction and is required for hinge point formation during neural tube closure. *Curr. Biol.* 13, 2125-2137.

- Hardin, J.D., and Cheng, L.Y. (1986). The mechanisms and mechanics of archenteron elongation during sea urchin gastrulation. *Developmental Biology* 115, 490-501.
- Hardin, J., and Walston, T. (2004). Models of morphogenesis: the mechanisms and mechanics of cell rearrangement. *Curr. Opin. Genet. Dev.* 14, 399-406.
- Hemerly, A.S., Ferreira, P.C., Van Montagu, M., Engler, G., and Inze, D. (2000). Cell division events are essential for embryo patterning and morphogenesis: studies on dominant-negative *cdc2aAt* mutants of *arabidopsis*. *Plant J.* 23, 123-130.
- Hildebrand, J.D. (2005). Shroom regulates epithelial cell shape via the apical positioning of an actomyosin network. *J. Cell. Sci.* 118, 5191-5203.
- Hohler, R., and Cohen-Addad, S. (2005). Rheology of liquid foam. *Journal of Physics: Condensed Matter* 17, R1041-R1069.
- Holland, L.Z. (2005). Non-neural ectoderm is really neural: evolution of developmental patterning mechanisms in the non-neural ectoderm of chordates and the problem of sensory cell homologies. *J. Exp. Zool. B. Mol. Dev. Evol.* 304, 304-323.
- Honda, H. (1983). Geometrical models for cells in tissues. *Int. Rev. Cytol.* 81, 191-248.
- Honda, H. (1978). Description of cellular patterns by Dirichlet domains: the two-dimensional case. *J. Theor. Biol.* 72, 523-543.
- Honda, H., Tanemura, M., and Nagai, T. (2004). A three-dimensional vertex dynamics cell model of space-filling polyhedra simulating cell behavior in a cell aggregate. *J. Theor. Biol.* 226, 439-453.
- Honda, H., Yamanaka, H., and Eguchi, G. (1986). Transformation of a polygonal cellular pattern during sexual maturation of the avian oviduct epithelium: computer simulation. *J. Embryol. Exp. Morphol.* 98, 1-19.
- Hove, J.R., Koster, R.W., Forouhar, A.S., Acevedo-Bolton, G., Fraser, S.E., and Gharib, M. (2003). Intracardiac fluid forces are an essential epigenetic factor for embryonic cardiogenesis. *Nature* 421, 172-177.
- Huang, S., Brangwynne, C.P., Parker, K.K., and Ingber, D.E. (2005). Symmetry-breaking in mammalian cell cohort migration during tissue pattern formation: role of random-walk persistence. *Cell Motil. Cytoskeleton* 61, 201-213.
- Huang, S., Eichler, G., Bar-Yam, Y., and Ingber, D.E. (2005). Cell fates as high-dimensional attractor states of a complex gene regulatory network. *Phys. Rev. Lett.* 94, 128701.

- Huang, S., and Ingber, D.E. (2005). Cell tension, matrix mechanics, and cancer development. *Cancer. Cell.* 8, 175-176.
- ILES, P.J.W. (2007). Estimation of cellular fabric in embryonic epithelia. *Comput. Methods Biomech. Biomed. Engin.* 10, 75-84.
- Ingber, D.E. (2003). Tensegrity II. How structural networks influence cellular information processing networks. *J Cell Sci* 116, 1397-1408.
- Ingber, D.E. (2005). Mechanical control of tissue growth: function follows form. *Proc. Natl. Acad. Sci.* 102, 11571-11572.
- Ingber, D.E. (2003). Tensegrity I. Cell structure and hierarchical systems biology. *J. Cell. Sci.* 116, 1157-1173.
- Izaguirre, J.A. (2004). COMPUCELL, a multi-model framework for simulation of morphogenesis. *Bioinformatics* 20, 1129-1137.
- Jacobson, A.G., and Gordon, R. (1976). Changes in the shape of the developing vertebrate nervous system analyzed experimentally, mathematically and by computer simulation. *J. Exp. Zool.* 197, 191-246.
- Jacobson, A.G., Oster, G.F., Odell, G.M., and Cheng, L.Y. (1986). Neurulation and the cortical tractor model for epithelial folding. *J. Embryol. Exp. Morphol.* 96, 19-49.
- Jacobson, C., and Jacobson, A. (1973). Studies on the morphogenetic movements during neural tube closure in Amphibia. *Zoon* 1, 17-21.
- Jamora, C., and Fuchs, E. (2002). Intercellular adhesion, signalling and the cytoskeleton. *Nat. Cell Biol.* 4, E101-8.
- Janiaud, E., and Graner, F. (2005). Foam in a two-dimensional Couette shear: a local measurement of bubble deformation. *J. Fluid Mech.* 532, 243-267.
- Karfunkel, P. (1974). The mechanisms of neural tube formation. *Int. Rev. Cytol.* 38, 245-271.
- Kauffman, S. (1969). Homeostasis and differentiation in random genetic control networks. *Nature* 224, 177-178.
- Keller, R. (2006). Mechanisms of elongation in embryogenesis. *Development* 133, 2291-2302.
- Keller, R. (2005). Cell migration during gastrulation. *Curr. Opin. Cell Biol.* 17, 533-541.

- Keller, R., Davidson, L., Edlund, A., Elul, T., Ezin, M., Shook, D., and Skoglund, P. (2000). Mechanisms of convergence and extension by cell intercalation. *Philos. Trans. R. Soc. Lond. B. Biol. Sci.* 355, 897-922.
- Kiehart, D.P., Galbraith, C.G., Edwards, K.A., Rickoll, W.L., and Montague, R.A. (2000). Multiple forces contribute to cell sheet morphogenesis for dorsal closure in *Drosophila*. *J. Cell Biol.* 149, 471-490.
- Kirschner, M., Gerhart, J., and Mitchison, T. (2000). Molecular "vitalism". *Cell* 100, 79-88.
- Kirschner, M.W. (2005). The meaning of systems biology. *Cell* 121, 503-504.
- Kitano, H. (2002). Systems Biology: A Brief Overview. *Science* 295, 1662-1664.
- Koehl, M. (1990). Biomechanical approaches to morphogenesis. *Sem. Dev. Biol.* 1, 367-378.
- Krendel, M.F., and Bonder, E.M. (1999). Analysis of actin filament bundle dynamics during contact formation in live epithelial cells. *Cell Motil. Cytoskeleton* 43, 296-309.
- Kung, C. (2005). A possible unifying principle for mechanosensation. *Nature* 436, 647-654.
- Lakirev, A.V., and Belousov, L.V. (1986). Computer modelling of gastrulation and neurulation in amphibian embryos based on mechanical tension fields. *Ontogenez* 17, 636-647.
- Lätzel, M., Luding, S., and Herrmann, H.J. (2000). Macroscopic material properties from quasi-static, microscopic simulations of a two-dimensional shear-cell. *Granular Matter* 2, 123-135.
- Lauffenburger, D.A., and Wells, A. (2001). Getting a grip: new insights for cell adhesion and traction. *Nat. Cell Biol.* 3, E110-2.
- Lawson, A., Anderson, H., and Schoenwolf, G.C. (2001). Cellular mechanisms of neural fold formation and morphogenesis in the chick embryo. *Anat. Rec.* 262, 153-168.
- Lecuit, T., and Pilot, F. (2003). Developmental control of cell morphogenesis: a focus on membrane growth. *Nat. Cell Biol.* 5, 103-108.
- Lee, C., Scherr, H.M., and Wallingford, J.B. (2007). Shroom family proteins regulate gamma-tubulin distribution and microtubule architecture during epithelial cell shape change. *Development* 134, 1431-1441.

- Malvern, L.E. (1969). *Introduction to the Mechanics of a Continuous Medium* (Englewood).
- Matthews, B.D., Overby, D.R., Mannix, R., and Ingber, D.E. (2006). Cellular adaptation to mechanical stress: role of integrins, Rho, cytoskeletal tension and mechanosensitive ion channels. *J. Cell. Sci.* 119, 508-518.
- Munro, E.M., and Odell, G. (2002). Morphogenetic pattern formation during ascidian notochord formation is regulative and highly robust. *Development* 129, 1-12.
- Munro, E.M., and Odell, G.M. (2002). Polarized basolateral cell motility underlies invagination and convergent extension of the ascidian notochord. *Development* 129, 13-24.
- Nechiporuk, T., and Vasioukhin, V. (2006). Planar cell polarity planes the inconveniences of cell division into a smooth morphogenetic process. *Dev. Cell.* 10, 153-154.
- Nelson, C.M., Jean, R.P., Tan, J.L., Liu, W.F., Sniadecki, N.J., Spector, A.A., and Chen, C.S. (2005). Emergent patterns of growth controlled by multicellular form and mechanics. *Proc. Natl. Acad. Sci.* 102, 11594-11599.
- Noble, D. (2002). Modeling the Heart-from Genes to Cells to the Whole Organ. *Science* 295, 1678-1682.
- Odell, G.M., Oster, G., Alberch, P., and Burnside, B. (1981). The mechanical basis of morphogenesis. I. Epithelial folding and invagination. *Dev. Biol.* 85, 446-462.
- Oster, G., and Alberch, P. (1982). Evolution and Bifurcation of Developmental Programs. *Evolution* 36, 444-459.
- Pilot, F., and Lecuit, T. (2005). Compartmentalized morphogenesis in epithelia: from cell to tissue shape. *Dev. Dyn.* 232, 685-694.
- Pollard, T.D., and Borisy, G.G. (2003). Cellular motility driven by assembly and disassembly of actin filaments. *Cell* 112, 453-465.
- Puddister, S.M. (2003). Estimating bulk geometrical properties of cellular structures. 16th International Conference on Vision Interface (VI'03), Halifax, NS, Canada, June 11-13.
- Rieu, J.P., Kataoka, N., and Sawada, Y. (1998). Quantitative analysis of cell motion during sorting in two-dimensional aggregates of dissociated hydra cells. *Physical Review E* 57, 924-931.
- Robinson, D.N., and Spudich, J.A. (2004). Mechanics and regulation of cytokinesis. *Curr. Opin. Cell Biol.* 16, 182-188.

- Rosenblatt, N., Alencar, A.M., Majumdar, A., Suki, B., and Stamenovic, D. (2006). Dynamics of prestressed semiflexible polymer chains as a model of cell rheology. *Phys. Rev. Lett.* 97, 168101.
- Rothenburg, L., (1981). Micromechanics of idealized granular systems. PhD. thesis. Dept. of Civil and Environmental Engineering. Carleton University.
- Runswick, S.K., O'Hare, M.J., Jones, L., Streuli, C.H., and Garrod, D.R. (2001). Desmosomal adhesion regulates epithelial morphogenesis and cell positioning. *Nat. Cell Biol.* 3, 823-830.
- Sausedo, R.A., Smith, J.L., and Schoenwolf, G.C. (1997). Role of nonrandomly oriented cell division in shaping and bending of the neural plate. *J. Comp. Neurol.* 381, 473-488.
- Schoenwolf, G.C., and Smith, J.L. (1990). Mechanisms of neurulation: traditional viewpoint and recent advances. *Development* 109, 243-270.
- Scott, I.C., and Stainier, D.Y. (2003). Developmental biology: twisting the body into shape. *Nature* 425, 461-463.
- Sekimura, T. (2003). Morphogenesis and pattern formation in biological systems (Tokyo: Springer).
- Shin, J., Gardel, M., Mahadevan, L., Matsudaira, P., and Weitz, D. (2004). Relating microstructure to rheology of a bundled and cross-linked F-actin network in vitro. *Proceedings of the National Academy of Sciences* 101, 9636-9641.
- Shraiman, B.I. (2005). Mechanical feedback as a possible regulator of tissue growth. *Proc. Natl. Acad. Sci. U. S. A.* 102, 3318-3323.
- Stamenovic, D., and Ingber, D.E. (2002). Models of cytoskeletal mechanics of adherent cells. *Biomech. Model. Mechanobiol* 1, 95-108.
- Stephanou, A., and Tracqui, P. (2002). Cytomechanics of cell deformations and migration: from models to experiments. *C. R. Biol.* 325, 295-308.
- Sukumar, N., Moran, B., and Belytschko, T. (1998). The natural element method in solid mechanics. *Int. J. Numer. Meth. Eng* 43, 839-887.
- Swartz, M.A., Tschumperlin, D.J., Kamm, R.D., and Drazen, J.M. (2001). Mechanical stress is communicated between different cell types to elicit matrix remodeling. *Proc. Natl. Acad. Sci. U. S. A.* 98, 6180-6185.

Taber, L.A. (2007). Biomechanical Modeling of Cardiac Looping. Proceedings of Experimental Biology Annual Meeting. Washington, DC, U. S. A., April 28<sup>th</sup>-May 2<sup>nd</sup>.

Taber, L.A. (1995). Biomechanics of growth, remodeling, and morphogenesis. *Appl. Mech. Rev.* 48, 487-545.

Thompson, D. (1942). *On growth and form.* (Cambridge, England: The University Press).

Vasioukhin, V., Bauer, C., Yin, M., and Fuchs, E. (2000). Directed actin polymerization is the driving force for epithelial cell-cell adhesion. *Cell* 100, 209-219.

Vasioukhin, V., and Fuchs, E. (2001). Actin dynamics and cell-cell adhesion in epithelia. *Curr. Opin. Cell Biol.* 13, 76-84.

Viens, D., and Brodland, G.W. (2007). A Three-dimensional Finite Element Model for the Mechanics of Cell-Cell Interactions. *ASME Journal of Biomechanical Engineering.* in Press.

Wallingford, J.B. (2005). Neural tube closure and neural tube defects: studies in animal models reveal known knowns and known unknowns. *Am. J. Med. Genet. C. Semin. Med. Genet.* 135, 59-68.

Wallingford, J.B., and Harland, R.M. (2002). Neural tube closure requires Dishevelled-dependent convergent extension of the midline. *Development* 129, 5815-5825.

Wiebe, C., (2002). Contact Algorithm for Embryonic Tissue Finite Element Analysis. Cive 611 course project. Department of Civil Engineering, University of Waterloo.

Wiebe, C., and Brodland, G.W. (2005). Tensile properties of embryonic epithelia measured using a novel instrument. *J. Biomech.* 38, 2087-2094.

Wilt, F., and Hake, S. (2004). *Principles of Developmental Biology* (New York, NY: W. W. Norton & Company).

Wriggers, P. (1996). Finite element methods for contact problems with friction. *Tribol. Int.* 29, 651-658.

Zone, T. (1996). Cooperative Model of Epithelial Shaping and Bending During Avian Neurulation: Autonomous Movements of the Neural Plate, Autonomous Movements of the Epidermis, and Interactions in the Neural Plate/Epidermis Transition Zone. *Developmental Dynamics* 2, 337.